DEVELOPMENT OF AN ACTIVE SEISMIC EXPERIMENT FOR LUNAR EXPLORATION

vorgelegt von

Dipl.- Geophys.

Alexandra Heffels, geb. Czeluschke

an der Fakultät VI - Planen Bauen Umwelt

der Technischen Universität Berlin

zur Erlangung des akademischen Grades

Doktorin der Naturwissenschaften

- Dr. rer. nat. -

genehmigte Dissertation

Promotionsausschuss:

Vorsitzender: Prof. Dr. Dr. h.c. Harald Schuh

Gutachter: Prof. Dr. Jürgen Oberst

Gutachterin: Prof. Dr. Christine Thomas

Gutachterin: Prof. Dr. Doris Breuer

Tag der wissenschaftlichen Aussprache: 20. April 2023

Berlin 2023

Acknowledgements

First of all, I would like to express my gratitude to Prof. Dr. Jürgen Oberst, who always supported my work with a great deal of understanding. He believed in this work from the very beginning and shared with me an enthusiasm for Apollo seismic data. Thank you for giving me the opportunity to study this valuable data set and for always giving me the advice I needed.

I would also like to thank Dr. Martin Knapmeyer for giving me the opportunity to broaden my horizons in many fields of research and for opening my eyes to the world of science.

Many thanks also to Dr. Frank Sohl and the many other colleagues at DLR who provided helpful suggestions for my work in numerous discussions.

For their quick and straightforward help and support I am especially indebted to Prof. Dr. Yosio Nakamura and Prof. Dr. Robert Kovach, who already evaluated the LSPE data in Apollo times and were so kind to share their wealth of experience with me. Furthermore, I thank the NASA Space Science Data Coordinated Archive (NSSDCA) for providing the original bitstream data of the Apollo 17 mission.

This work was done within the framework of the Helmholtz Alliance ROBEX and therefore I would also like to thank the colleagues who contributed to the improvement of my work within this alliance with constructive discussions. Special thanks go to Dr. Autun Purser, whose help in proofreading was very welcome and whose art inspired me.

I thank Prof. Dr. Reinhart Claus for his supportive and uplifting words.

Finally, my special thanks go to my family who supported me at all times. The biggest thanks go to my husband Fabian Heffels, without whose love, patience and support this work would not have been possible.

I would like to dedicate this work to my mother Barbara, who always filled my life with love and understanding.

Structure of the dissertation

The dissertation is structured as follows: An introduction to the Moon and NASA's Apollo program with special focus on the Apollo 17 Lunar Seismic Profiling Experiment, as well as an overview to refraction seismics and its application to the Helmholtz Alliance "Robotic Exploration of Extreme Environments – ROBEX". This is followed by four scientific publications (accepted manuscript included), which were published, submitted in peer-reviewed journals. The four papers are:

Research Paper I
A. Heffels, M. Knapmeyer, J. Oberst, I. Haase.
Re-evaluation of Apollo 17 Lunar Seismic Profiling Experiment data.
Planetary and Space Science 135 (2017), 43-54.
http://dx.doi.org/10.1016/j.pss.2016.11.007.

Research Paper II
A. Heffels, M. Knapmeyer, J. Oberst, I. Haase.
Re-evaluation of Apollo 17 Lunar Seismic Profiling Experiment data including new LROC-derived Coordinates for Explosive Packages 1 and 7, at Taurus-Littrow, Moon
Planetary and Space Science 206 (2021), 105307.
https://doi.org/10.1016/j.pss.2021.105307

Research Paper III
A. Heffels, C. Lange, N. Tóth, S. Jahnke, P. Jaspers.
System design and laboratory tests of an autonomous seismic station for space applications
Planetary and Space Science, 217(2022), 105489
https://doi.org/10.1016/j.pss.2022.105489

The results from these papers are discussed in the synthesis section, and further questions are addressed. This is followed by an outlook.

Alexandra Heffels was the main contributor to the methods and results described in this thesis. The work presented in the three papers was improved by comments of the reviewers and through discussions with the ROBEX team. The author received support from colleagues at German Aerospace Center (DLR) Berlin. The work presented in this dissertation was performed when the author was supported by the Helmholtz Alliance "Robotic Exploration of Extreme Environments – ROBEX" (HA-304) and DLR Berlin.

Abstract

The subject of this thesis was the evaluation of historical Apollo 17 Lunar Seismic Profiling data in combination with the design and operation of a new active seismic experiment for planetary applications.

During the Apollo program, running between 1961 and 1972, there were a total of six manned landings. Astronauts deployed a number of scientific instruments on the Lunar surface, some of which continued operation long after the Apollo missions. Among these was the Lunar Seismic Profiling Experiment (LSPE) set up by astronauts on Apollo 17, which consisted of four geophones in a Y-shaped array and eight explosive packages. The setup was used to register the signals of the eight remotely detonated explosions as well as to passively listen for natural seismic signals. To date, this setup represents the largest seismic experiment conducted outside of the Earth.

In 2009, the Lunar Reconnaissance Orbiter (LRO) was launched with the task of mapping the lunar surface in high resolution. Special attention was paid to a precision mapping of the Apollo landing sites. It turned out that the positions of the Apollo instruments differed substantially from the previously determined positions, thus requiring updates of the previously determined seismic velocity-depth profiles. The first part of this work was to go back to the original bitstreams of the Apollo data to carry out new arrival time readings for the seismic P-waves. Using the new positional data of the seismic sources and receivers, these were inverted to derive a new velocity-depth profiles. The comparison with historical results showed that the use of the corrected distance data led to a significant reduction in layer thicknesses and a stronger increase in P-wave velocity with depth. Overall, this resulted in a stronger compaction of the subsurface material than previously assumed being indicated.

In the second part of this thesis, an active seismic experiment was developed and operated, which was largely based on the idea of the Apollo 17's LSPE. The experiment scenario was now to be set up and carried out by autonomous robotic systems. DLR Bremen developed two autonomous measurement systems, what we called “Remote Units” (RU), for this scenario. The Mascot design of the Japanese Hayabusa2 probe proved to be a suitable basis for this development. Following a number of laboratory tests, the RUs were brought to application in the context of the demo mission “Space” of the Helmholtz Alliance "ROBEX", for which a terrain on Mount Etna in Italy was chosen as the experiment site. Seismic data were successfully obtained, and the evaluation of the data confirmed earlier results on the geology and subsurface structure of the test area determined with standard methods. Thus, the evaluation of the seismic data could not only show that the developed experimental scenario and equipment were suitable to explore near-surface stratifications by means of refraction seismic experiments, but also that the selected test area on Mount Etna, featuring strata of lava flows in the subsurface, actually qualified as a lunar analogue terrain.

Zusammenfassung

Das Thema dieser Arbeit war die Auswertung historischer Daten des Apollo 17 Lunar Seismic Profiling in Kombination mit dem Entwurf und Betrieb eines neuen aktiven seismischen Experiments für planetare Anwendungen.

Während des Apollo-Programms zwischen 1961 und 1972 gab es insgesamt sechs bemannte Landungen, welche viele unterschiedliche Experimente zum Mond brachten. Darunter war auch das von Apollo 17 durch Astronauten aufgebaute Lunar Seismic Profiling Experiment (LSPE), welches aus vier Geophonen in einem Y-förmigen Array und acht Sprengladungen (Explosive Packages) bestand. Der Aufbau diente zum einem der Registrierung der Signale der acht ferngezündeten Detonationen als auch zum passiven Lauschen nach natürlichen Signalen. Bis heute repräsentiert dieser Aufbau das größte seismische Experiment außerhalb der Erde.

Im Jahr 2009 startete dann der Lunar Reconnaissance Orbiter (LRO) mit der Aufgabe die lunare Oberfläche hochauflösend zu kartieren. Besonderes Augenmerk wurde hierbei auf die präzise Kartierung der Apollo-Landestellen gelegt. Dabei zeigte sich, dass die Positionen der Apollo-Geräte zum Teil stark von den bisher angenommenen Positionen abweichen. Da seismische Daten sehr sensibel auf Distanzänderungen reagieren, musste geklärt werden, wie stark die berechneten Tiefenprofile auf diese Abweichungen reagierten. Ein erster Teil dieser Arbeit bestand darin, auf die ursprünglichen Bitströme der Apollo-Daten zurückzugehen, um neue Ankunftszeiten für die seismischen P-Wellen zu ermitteln. Unter Verwendung der neuen Positionsdaten der seismischen Quellen und Empfänger wurden diese invertiert, um neue Geschwindigkeitstiefenprofile zu erstellen. Der Vergleich mit historischen Ergebnissen zeigte, dass die Verwendung der korrigierten Entfernungsdaten zu einer deutlichen Verringerung der Schichtdicken und einem stärkeren Anstieg der P-Wellengeschwindigkeit mit der Tiefe führte. Daraus ergab sich insgesamt eine stärkere Kompaktierung des Untergrundmaterials als bisher angenommen.

Im zweiten Teil dieser Arbeit wurde ein aktives seismisches Experiment entwickelt und betrieben, das weitgehend auf der Idee des LSPE von Apollo 17 basierte. Das Experimentszenario sollte nun durch autonome robotische Systeme aufgebaut und durchgeführt werden. Das DLR Bremen entwickelte für dieses Szenario zwei autonome Messsysteme. Diese auf dem Mascot-Design der japanischen Hayabuse2-Sonde basierten Geräte wurden Remote Units (RU) genannt.

Nach einer Reihe von Labortests, welche die Funktionsfähigkeit und Datenaufnahmequalität der RUs belegten, wurden die RUs im Rahmen der Demo-Mission „Space“ der Helmholtz-Allianz „ROBEX“ im Feld zur Anwendung gebracht. Als Testgebiet wurde hierfür ein Gelände in ca. 2500m Höhe am Vulkan Ätna in Italien gewählt. Es wurden erfolgreich seismische Daten gewonnen, deren Auswertung bestätigte frühere mit Standardmethoden ermittelte Ergebnisse zur Geologie und Untergrundstruktur des Testgebietes. Somit konnte die Auswertung der seismischen Daten nicht nur zeigen, dass das entwickelte Experimentszenario und die Ausrüstung geeignet waren, um wie gewünscht oberflächennahe Schichtungen mittels refraktionsseismischer Experimente zu erkunden, sondern auch, dass sich das gewählte Testgebiet auf dem Ätna durch die vorliegenden Lavaschichten im Untergrund tatsächlich als mondanaloges Terrain qualifizierte.

Contents

List of Figures

List of Tables

1. Motivation

The Moon, as Earth‘s companion, has always been of great interest to people around the world. But it was not until the Apollo missions from 1969 onwards that people came close enough to touch the Earth's satellite. During a total of six manned landings, the Apollo program brought many different experiments to the lunar surface, among them the Lunar Seismic Profiling Experiment (LSPE) of Apollo 17, which was the focus of this work. The LSPE, with its four geophones and eight explosive packages, was the largest seismic experiment ever conducted on a planetary body other than Earth. From today's perspective, the equipment used was simple. But due to its robustness, it was possible to record incredible data, which represent a great scientific treasure.

But even after the Apollo missions, the Moon remained the focus of interest. In 2009, the Lunar Reconnaissance Orbiter (LRO) was launched and its main task was to map the surface of the moon in high resolution, with special attention to the former Apollo landing sites. It turned out that the positions of the Apollo equipment, in particular, the distances between the LSPE devices, deviated strongly from the previously determined data. This made it necessary to re-evaluate the seismic data, as the calculated subsurface profiles would react very sensitively to deviations in these distances. So, the first step of work was to clarify how exactly the calculated profiles would react to the changed data. This included both a re-deciphering of the original historical data bit stream and the re-determination of first arrival times of P-waves, thus generating a self-consistent new data set that could be evaluated.

A further step was then the question of how an experiment such as the Apollo 17 LSPE would be realised in today's world. From today's perspective, astronauts were no longer necessarily the best solution for deploying the components of such an experimental setup. It has always been a complex, time-consuming and costly to send humans into space, keep them alive and bring them back safely. Rapidly evolving technology, especially robotic research and development has made it possible to consider a modern re-enactment of the Apollo 17 LSPE. Increasing the use of autonomous robotic systems, especially for simple standard tasks, could enable astronauts to do more meaningful science. Therefore, the development of an autonomously operating measurement system, called the Remote Unit, was crucial. It had to be ensured that the developed system was capable of delivering scientifically usable data.

In a final step, the developed experiment was tested in a final demonstration mission on Mount Etna, Italy, in 2017. The experiment, which was motivated by the idea of the Apollo 17 LSPE, was intended to show that an experiment carried out by autonomous robotic systems in a lunar analogue territory could achieve scientifically valuable results.

2. Introduction

2.1 The Moon

The Moon is Earth's only permanent natural satellite. It moves around Earth in a nearly circular orbit at an average orbital distance of 384000 km. The orbital period is 27.3 days and the synodic period (i.e., the orbit with respect to the Sun) is 29.5 days. The Moon's rotation is tidally locked, which means it is always the same hemisphere (the "nearside") that faces the Earth. With a mean radius of 1737.1 km, which represents a little more than 25% of the Earth's radius, it is the largest known planetary satellite with respect to the planet that it orbits. The Moon has an overall spherical shape with notable deviations from a perfect sphere due to its rough topography (cf. Table 1). From measurements of its gravity field and global shape, it can be seen that the center of the figure and the center of mass are displaced by about 2 km (Vermillion, 1975), suggesting that the crust of the nearside is clearly thinner than on the farside, the "lunar dichotomy". Given the lunar volume and mass, the mean density is found as 3.34 g/cm³, similar to the density of the Earth's mantle. The Moon possesses a faint transient atmosphere consisting of of helium, neon, hydrogen, argon, and various trace gases (e.g., CH_4, NH_3, CO_2). The lack of a substantial atmosphere and the slow rotation leads to extreme temperature differences between the day- and night hemispheres. In bright sunlight temperatures can rise up to 390 K (117 °C) whereas at night or in shadowed areas temperatures can fall to minimum values of approximately 100 K (-173 °C). According to the most widely accepted theory, the Moon was created by a giant impact. An approximately Mars-sized body called Theia collided with the proto-Earth. Excavated debris from Earth's crust and the mantle of the impacting body conglomerated in an orbit around Earth and formed the Moon (Canup and Asphaug, 2001; Canup, 2004; Young et al., 2016).

Table 1: Physical properties of the Moon

PROPERTY	MOON
MASS	7.342×10^{22} kg
RADIUS (EQUATORIAL)	1738.1 km
RADIUS (POLAR)	1736.0 km
SURFACE AREA	3.793×10^{7} km^2
MEAN DENSITY	3344 kg/m^3
SURFACE GRAVITY	1.622 m/s^2
SIDERAL ROTATION TIME	27.321661 d (spin-orbit locked)
MEAN SURFACE TEMPERATURE	380 K or 107 °C (day) 120 K or -153 °C (night)
MAGNETIC FIELD	small paleo field
ATMOSPHERE	10^{-7} Pa (day) 10^{-10} Pa (night)

2.1.1 Surface geology and structure of the Moon

Even with the naked eye, bright and dark patterns can be distinguished on the illuminated lunar disk. The dark lunar plains, the maria (Latin for "seas"; singular: mare), represent solidified ancient basaltic lava pools. In the early stages of lunar formation, giant impacts penetrated the thin lunar crust and

ascending magma filled topographic low areas (Mackin, 1969). Maria are not evenly distributed on the lunar surface. About 31% of the nearside is covered with maria, whereas on the farside hardly any maria can be found (only 2.6%). This means that the lunar farside is mainly characterized by the brighter highland plateaus (terrae). Impact craters of all sizes can be found on the lunar surface. Except in areas of a few very young craters the entire surface is covered with the so-called regolith, a physically weathered rock. As mentioned before the atmosphere of the Moon is extremely thin, which does not provide any protection against impacts of any type. Therefore an extremely thin atmosphere is associated with continuous impacts of meteorites and micrometeorites as well as influences of solar and galactic charged particles. Altogether being responsible for the formation of regolith. Grain sizes of lunar regolith range from the finest dust to large boulders. The thickness of regolith varies from 3

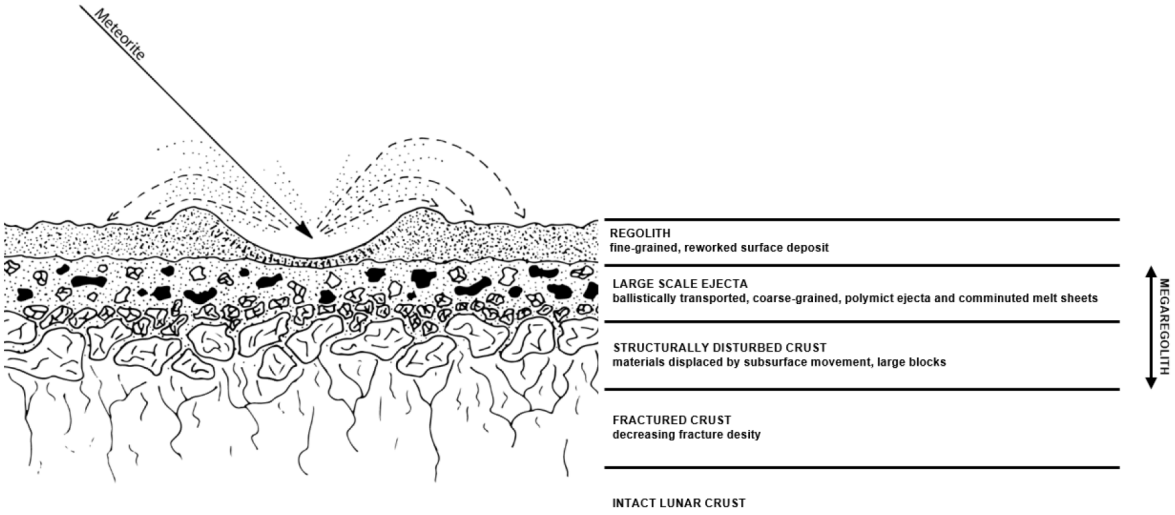

Figure 1: Schematic cross-section illustrating effects of meteorite impacts and the resulting structure of the uppermost lunar surface layers. (Modified illustration from Hörz et al., 1991, Lunar Surface Processes, in The Lunar Sourcebook, pp. 62-120).

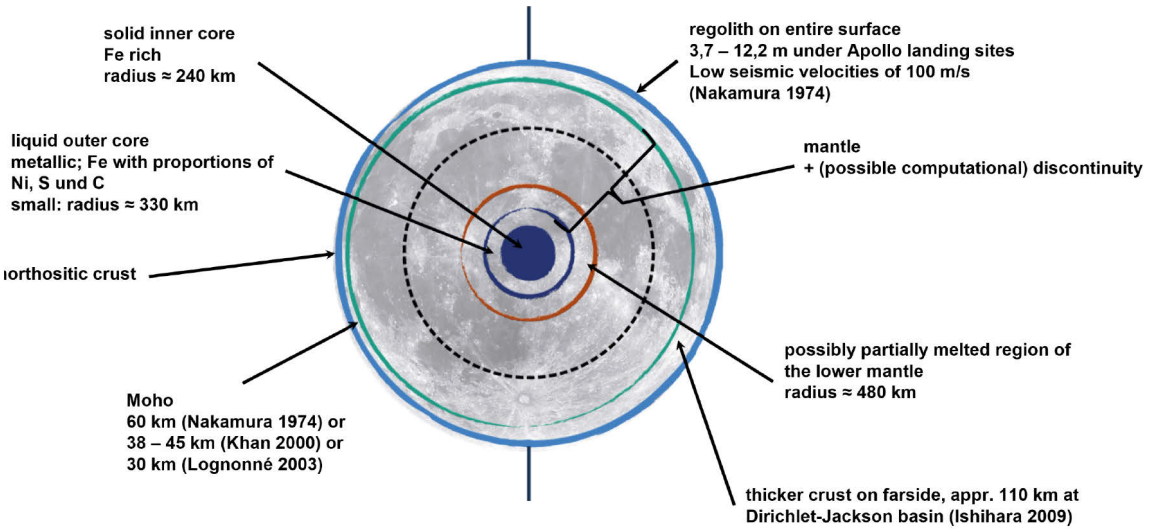

Figure 2: Schematic view of the internal structure of the Moon. Moon has a distinct crust, mantle and core.

to 15 m (3.7 – 4.4 m under Apollo landing sites) and tends to be thicker in the highlands. It is characterized by very low seismic velocities of 100 m/s (Nakamura et al., 1974). Below the regolith layer blocky and fractured bedrock forms a region called megaregolith (see Figure 1, p. 3).

Figure 2 (p. 3) shows a schematic view of the lunar interior. The anorthositic lunar crust is thicker on the farside, being thickest at about 110 km (at Dirichlet-Jackson Basin; Ishihara et al., 2009). A number of studies have investigated the crustal thickness on the near side. According to Toksöz (1973), the boundary layer between crust and mantle is at 60 km depth. However, Khan (2000) calculates this boundary layer to be at around 45 km depth. The more recent study of Lognonné (2003) claims that boundary to be even lower at only 30 km depth. Ishihara et al. (2009) calculates a detailed lunar crustal thickness map by combining gravity and topography models. In their study, values for crustal thickness vary from nearly zero to 110 km with a mean thickness at about 53 km. For the mantle below, some studies suggest one or more discontinuities (cf. Nakamura, 1983; Lognonné et al., 2003; Gagnepain-Beyneix et al., 2006). The lunar core is covered by a partially molten boundary layer. The core itself has

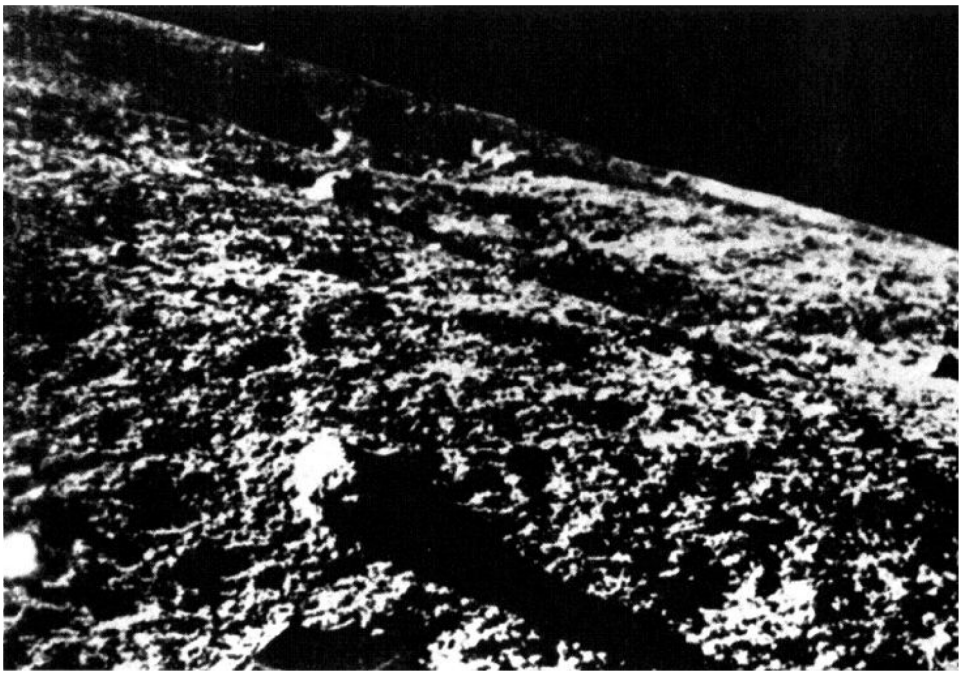

Figure 3: The first image from the surface of the moon, taken by the Luna 9 spacecraft. (Credit: UdSSR/NASA)

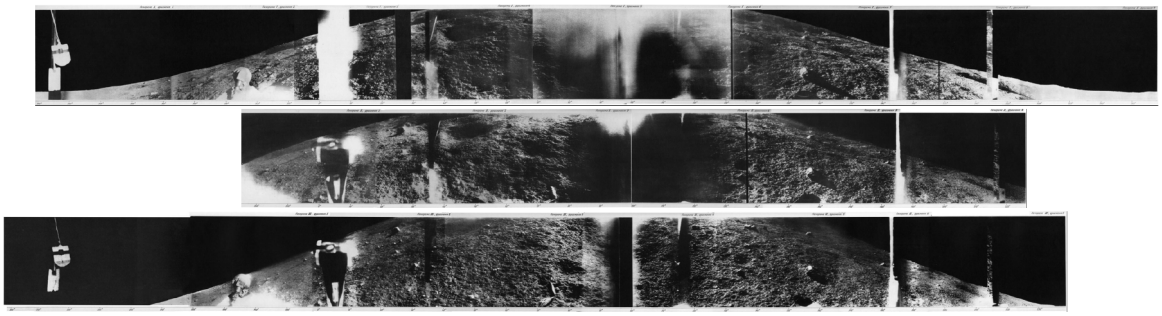

Figure 4: Black and white cycloramic panorama pictures taken with an optical-mechanical camera by Luna 9. (Credit: UdSSR/NASA)

a solid inner part and a liquid outer region. The study of Weber et al. (2011) suggests that the core is ~60% liquid by volume.

2.2 Moon missions and their findings regarding seismic observations

The knowledge about the Moon and its inner structure outlined earlier in this section was not only based on astronomical observations. In addition, many different missions have contributed to our knowledge. The first attempts to visit the Moon with unmanned spacecraft were made as early as at the end of the 1950s. In March, 1959, NASAs Pioneer 4 made the first fly-by of the Moon at a distance of about 60000 km before it became the first US spacecraft to enter interplanetary space. In September of the same year the Soviet spacecraft Lunik 2 (also known as Luna 2) performed the first hard landing on the Moon. It was thus the first artificial object that purposefully hit the moon. The first US-American spacecraft that hit the lunar surface was the Ranger 4 probe in April, 1962, however, suffering from break of radio communication before impact. 1966, the Soviet Luna 9 probe executed the first soft landing on the lunar surface. After landing in Oceanus Procellarum, the probe carried out radiation measurements and sent images to Earth, which could later be assembled into black and white stereoscopic full (360°) panoramas (Figure 3 and Figure 4, p. 4). Many more unmanned missions followed. Most notably, the manned missions of NASA's Apollo program contributed to our better understanding of the Moon.

2.2.1 Apollo-Program

Following the Mercury and Gemini missions, Apollo was NASA's third human spaceflight program and the first project that successfully landed humans on the Moon. Apollo 11 was the first mission in the program to land on the lunar surface in July 1969. Five more successful landings followed before the project was shut down after Apollo 17's return to Earth in December 1972. These missions were of great importance for science and our understanding of the Moon. A total of 382 kg of lunar rock and soil were brought back to Earth during the program. This allowed deeper insights into the geological history and composition of the Moon. However, besides the recovery of lunar rocks, various scientific experiments were carried out by the astronauts on the lunar surface.

A modular instrument complex called Apollo Lunar Surface Experiments Package (ALSEP) was used to carry out the experiments. Only Apollo 11 used a simpler version, the Early Apollo Scientific Experiments Package (EASEP). EASEP comprised two basic and independent experiments, the Laser Ranging Retro Reflector (LRRR) and the Passive Seismic Experiment Package (PSEP), which was self-supporting since it was equipped with all subsystems needed to operate (such as structure/thermal subsystem, solar panel array for power supply, data subsystem, etc.). PSEP used three long-period seismometers and one short-period vertical seismometer. It was built to record seismic signals from meteoroid impacts and moonquakes. Starting with Apollo 12 the more complex ALSEP was used. All ALSEPs had in common a Central Station for communication to Earth, a Radioisotope Thermoelectric Generator (RTG) as power source and an RTG cask to store the radioactive plutonium-238 pellets needed for operation of the RTG. The scientific components of the ALSEP comprised experiments to measure the flux of charged particles, the pressure and composition of the lunar atmosphere, and surface heat flow, as well as gravimeters, magnetometers, spectrometers, seismometers, and laser retroreflector arrays. In this work, special attention was paid to the seismic experiments. Apollo 12 to 16 carried the Passive Seismic Experiment (PSE). It was no longer a self-supporting system with all

necessary subsystems as the Apollo 11 PSEP. PSE, for these missions, used the Central Station of ALSEP for energy supply, communication and so on. Thereby, through the Central Station the PSE had access to the nuclear power of the RTG and could therefore operate continuously (not only daylight hours). PSE was used to measure the natural seismic activity of the Moon and to further specify the properties of the lunar crust and interior. Apollo 14 and 16 carried the Active Seismic Experiment (ASE). It comprised a set of three geophones laid out in a line to detect explosions. Explosions were generated either with an astronaut-activated Thumper (see Figure 5, p.7) which could create small shocks or with a mortar package that could fire a set of four explosives to different distances from the Central Station after the astronauts had left the Moon. The aim of this experiment was the seismic exploration below the landing sites to depths of several hundred meters. Apollo 17 carried a more complex seismic experiment, the Lunar Seismic Profiling Experiment (LSPE). The network consisted of four geophones placed in the center and at each corner of a 90 m equilateral triangle (cf. lower left panel of Figure 5), designed to determine directions from which seismic signals arrived, allowing for more accurate measurements of seismic velocities than the ASE of Apollo 14 or 16 before. A total of eight Explosive Packages (EP) served as seismic sources. The amount of explosives used in the EPs varied between 57 g and 2722 g depending on the planned distance of deployment. Each EP was equipped with several securing mechanisms (two delay timers which were activated after pulling three arming pins, cf. lower right panel in Figure 5). After the astronauts had left the lunar surface, the EPs were remotely detonated one after the other. The geophone array should not only record the detonations of EPs but were also meant to measure the thrust of the Lunar Module's ascent stage during launch and to observe the seismic response upon its re-impact on the lunar surface. In addition, the LSPE could be commanded to a passive listening mode to register natural seismic events.

The active part of the Apollo 17 LSPE, i.e. the evaluation of the seismic signals induced by the explosions, was in focus of this research.

2.2.2 Lunar seismic signals

Immediately after the first observation of the lunar seismic signals, it became apparent that the signals were extremely different from terrestrial signals. The spectra were broad, showed a lack of structure, and the signal decay times were extremely long up to several hours for larger impacts. This could be explained by two things: (a) The fine grained regolith at the lunar surface led to strong scattering of seismic waves and (b) at the almost complete absence of water in the surface material meant that there was almost no attenuation of seismic signals.

A number of studies investigated both active and passive seismic experiments. Thereby, different types of natural and artificial seismic events could be identified.

The natural events included: (1) Thermal moonquakes, (2) deep moonquakes, (3) shallow moonquakes, and (4) meteoroid impacts.

(1) Thermal moonquakes appeared to be very small and showed remarkable regularities. They appeared at the same time of each lunation and they had nearly identical waveforms and amplitudes. Their activity started abruptly after sunrise and decreased soon after sunset. In a highly scattering medium such as lunar regolith, two seismic signals could only be identical if they were generated at the same source and registered at the same station. Therefore, the favored mechanism to explain this type of event was slumping of soil on lunar slopes triggered by diurnal temperature changes (Duennebier and Sutton, 1974).

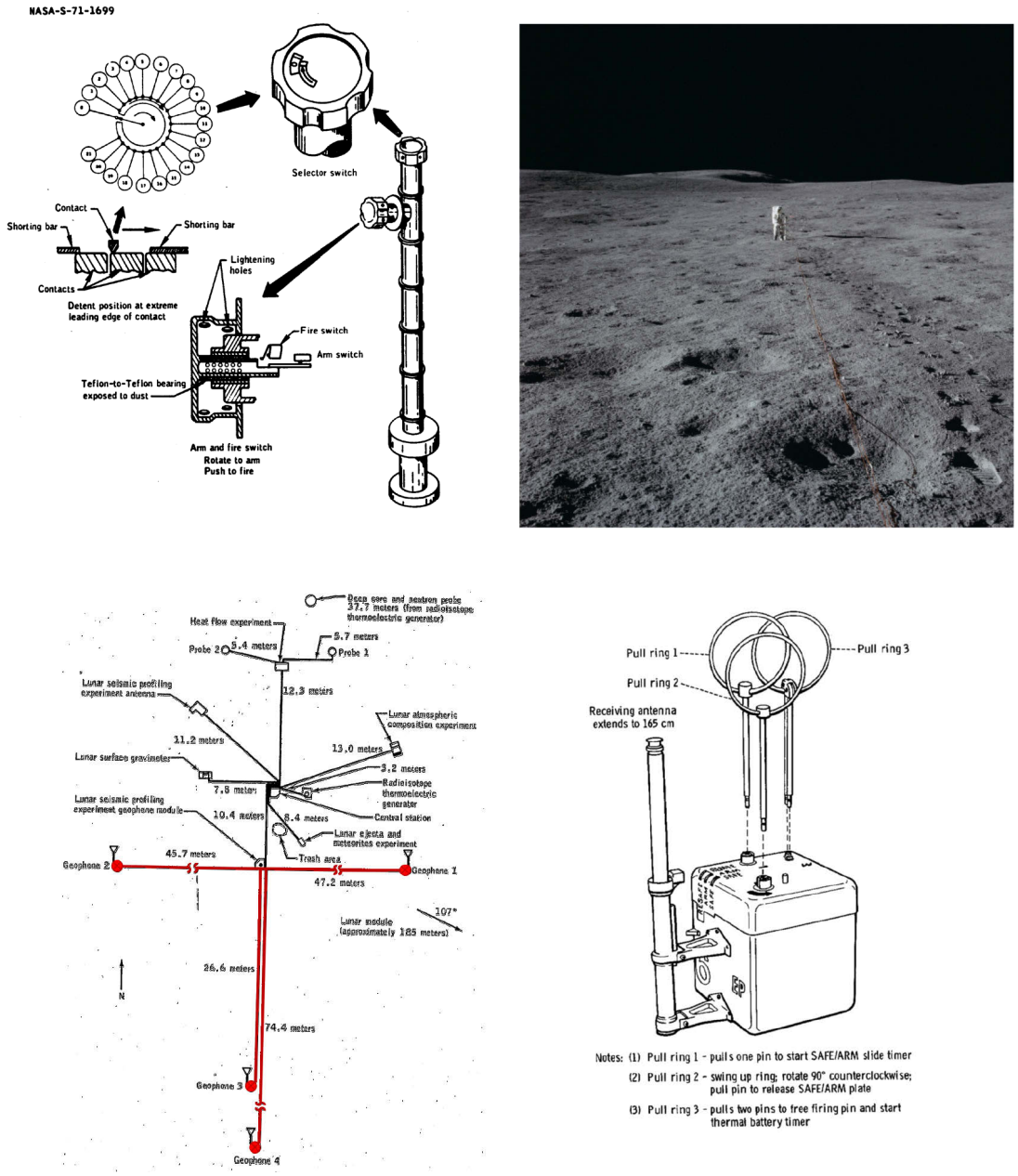

Figure 5: ((Upper left) Diagram of the Thumper component of the Active Seismic Experiment of the ALSEP. (Credit: NASA, Apollo 14 Mission Report: Figure 14-31). (Upper right) Thumper device operated by Lunar Module Pilot Edgar Mitchell on the lunar surface during Apollo 14. (Credit: NASA). (Lower left) Layout of Apollo 17's ALSEP with geophone array highlighted in red. (Lower right) Depiction of arming sequence of LSPE Explosive Package. (Credit: NASA).

(2) Deep moonquakes were the most common type of moonquake and they were small in magnitude (less than 3 in body wave equivalent; Weber, 2014). Their source was approximately halfway between the surface and the center of the moon (700 – 1200 km depth). They showed nearly identical waveforms and occurred from distinct source regions. It was shown that these events are clearly linked to the tides caused by the Earth and Sun on the Moon (Koyama & Nakamura, 1980; Nakamura et al., 1982). Frohlich and Nakamura (2009) discussed fatigue processes in the rock due to the repeated tide-induced stresses on certain heterogeneities in the subsurface as a possible cause for this type of moonquake.

(3) Shallow moonquakes were rare compared with the other event types, but they were the most energetic seismic sources on the Moon. Due to their high-frequency content they were sometimes referred to as high-frequency teleseismic (HTF) events. Besides the high-frequency content they showed relatively well-defined P- and S-wave arrivals (Nakamura, 1977). Most of these occurred in the upper mantle region. In contrast to deep moonquakes, shallow moonquakes showed no clear correlation to lunar tides. They seemed to represent truly tectonic moonquakes which implies that the only region with existing tectonic stresses high enough to cause abrupt mechanical failure was the upper mantle of the lunar interior (Nakamura, 1979). Furthermore, shallow moonquakes were associated with high stress drops (>100 MPa). Such high stresses in the lunar crust could indicate that during its formation phase the Moon was not only covered by a magma ocean but could have been entirely molten (Oberst, 1987).

(4) Meteoroid impacts on the lunar surface provided a natural source that that gave insights to the lunar interior. Their masses varied on average between 500g and 50kg. From the statistics of impacts in space and time clues were obtained on the orbital distribution of the meteoroids. From observed clustering, some impacts were clearly correlated to known meteor showers (Dorman et al., 1978; Oberst and Nakamura, 1991).

Artificial events included: (a) Impacts, (b) thumper shocks, (c) explosions, and (d) landing module induced noise.

(a) Impacts of spent rocket upper stages or landing modules of the Apollo missions that were deliberately crashed into the lunar surface in order to use the seismic signals generated in this way.

(b) Apollo missions 14 and 16 carried an experiment package called ASE. One part of this experiment packages was an astronaut-activated device called Thumper (see Figure 5). It comprised 22 explosive charges for creating small seismic shocks.

(c) Apollo 17 carried the Lunar Seismic Profiling Experiment (LSPE) which comprised a set of eight explosive packages which were detonated remotely after the astronauts had left the lunar surface safely.

(d) When evaluating the seismic data, it was found that the geophones also recorded events that could be associated with moving liquids and bubbles rising inside the tanks within the landing craft, and other noise induced by the landing module (Latham et al., 1971).

2.2.3 Lunar Reconnaissance Orbiter

The robotic Lunar Reconnaissance Orbiter (LRO) was launched on June 18, 2009. From a near-circular orbit, LRO used six individual instruments to map the lunar surface at very high resolution (maximum 50 cm/pixel for cameras). Its payload included (1) Lunar Orbiter Laser Altimeter (LOLA) for global topography mapping, (2) Lunar Reconnaissance Orbiter Camera (LROC) comprising two Narrow Angle Cameras (NACs) for acquiring high-resolution (up to 50 cm/pixel) images and a Wide-Angle Camera (WAC) with multispectral capability for identification of lunar resources, (3) Lunar Exploration Neutron Detector (LEND) for mapping flux of neutrons from the lunar surface to search for evidence of water ice, (4) Diviner Lunar Radiometer Experiment (DLRE) for identifying cold-traps and potential ice-deposits by measuring the temperature (appr. 300 m horizontal resolution), (5) Lyman-Alpha Mapping Project (LAMP) for mapping in the far ultraviolet to detect surface ice, and (6) Cosmic Ray Telescope for the Effects of Radiation (CRaTER) to investigate the effect of galactic cosmic rays on tissue-equivalent plastics (Chin et al., 2007).

Among other targets of interest, special attention was paid to the Apollo landing sites. The detailed maps generated from LRO data allowed the identification and recovery of positions of deployed equipment. Specifically, Haase et al. (2013) determined geometrically accurate coordinates (lat/long/heights) of the Apollo 17 seismic array components by combining high-resolution orthoimages from NAC with Apollo surface panoramas taken by the astronauts. When comparing previously published (historical) coordinates and new LRO derived coordinates of seismic equipment it became apparent that coordinates differed by up to 40 m. Evaluation of seismic data was sensitive to such spatial differences which meant that seismic models could differ drastically when different coordinates were used. Therefore, Paper I and II were dedicated to the reanalysis of the seismic data using new seismic arrival time readings and coordinate information to update seismic velocity depth profiles from the Apollo 17 site.

2.3 Refraction seismics

As introduced above, the Apollo 17 LSPE was the largest seismic experiment conducted on another celestial body. The main goal of the experiment was to characterize the subsurface down to a depth of approximately 2500 m. For this purpose, seismograms of the eight shocks generated by detonating the EPs were evaluated by refraction seismics.

This method made use of the fact that seismic waves travel at different velocities through different types of media. This allowed the determination of general soil types as well as layer thicknesses and layer depths. When using refraction seismics, it made sense to represent seismic waves not by their waveform, but rather by wave fronts or seismic rays. Thereby certain properties of the waves could be illustrated.

Snell's law and the reflection law are basics for refraction seismics. According to Fermat's principle, signals (as well as seismic waves) propagate along defined ray paths so that their travel time is stationary between two points, meaning that the travel time does not change with small variations of the travel path (cf. Fig. 6).

$$t = \frac{1}{v_1}\sqrt{h_1^2 + x^2} + \frac{1}{v_2}\sqrt{h_2^2 + (d-x)^2}$$

$$0 = \frac{dt}{dx} = \frac{1}{v_1}\frac{x}{\sqrt{h_1^2 + x^2}} + \frac{1}{v}\frac{-(d-x)}{2\sqrt{h_2^2 + (d-x)^2}} =$$

$$= \frac{1}{v_1}\frac{x}{l_1} - \frac{1}{v_2}\frac{(d-x)}{l_2} = \frac{1}{v_1} sin\, i_1 - \frac{1}{v_2} sin\, i_2$$

$$\Rightarrow \frac{sin(i_1)}{v_1} = \frac{sin(i_2)}{v_2}$$

Where h_1, h_2, l_1, l_2, d and x are as denoted in Fig. 6, upper panel. For this equation, it does not matter whether these are P-waves or S-waves. In fact, nothing changes if a wave travels as a P-wave with velocity v_{p1} in the first medium and continues as an S-wave with velocity v_{s2} in the second medium. Therefore, this equation also applies to converted waves. Besides, the receiver can be located either in the upper or lower medium.

$\frac{sin\, i_1}{v_1} = \frac{sin\, i_1'}{v_1}$ (Law of Reflection).

If source and receiver are in the same medium, it must be considered that the seismic ray has more than one point in common with the interface. If $v_2 > v_1$, it is conceivable that a wave that travels partially along the boundary layer arrives at the receiver earlier than a reflected wave (cf. Fig. 6, lower panel).

In that case, the travel time also depends on Y and must be extreme when differentiating by x and y.

$$t(x,y) = \frac{1}{v_1}\sqrt{x^2 + h_1^2} + \frac{y-x}{v_2} + \frac{1}{v_1}\sqrt{(d-y)^2 + h_2^2}$$

$$0 \equiv \frac{\partial t}{\partial x} = \frac{1}{v_1}\frac{x}{\sqrt{x^2 + h_1^2}} - \frac{1}{v_2} = \frac{sin\, i_x}{v_1} - \frac{1}{v_2}$$

$$\Rightarrow sin\, i_x = \frac{v_1}{v_2}$$

$$0 \equiv \frac{\partial t}{\partial y} = \frac{1}{v_2} + \frac{1}{v_1}\frac{-(d-y)}{\sqrt{(d-y)^2 + h_2^2}} = \frac{1}{v_2} - \frac{sin\, i_y}{v_1}$$

$$\Rightarrow sin\, i_y = \frac{v_1}{v_2}$$

So, there is only one special angle of incidence for such a wave, the critical angle $sin\, i_c = \frac{v_1}{v_2}$ (Snell's Law). Since $\sin i_c < 1$, this wave exists only if $v_2 > v_1$. This wave is called a head wave.

Further evaluation is done by creating travel time curves. In this type of graph, arrival times of seismic waves at different points are plotted as a function of distance from the seismic source. Seismic velocities can be computed from slopes of the resulting curves.

Two-layer case

This case is depicted in Figure 7, where the upper layer has a seismic velocity of v_1 and a thickness of h_0, the lower layer has a seismic velocity of v_2. A direct wave (blue) propagates by the shortest route

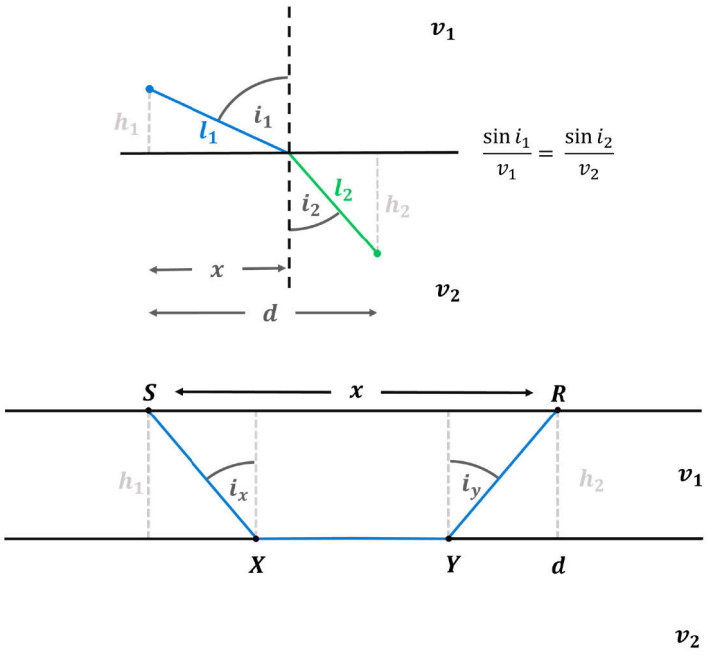

Figure 6: Schematic ray paths.

between source and receiver. The slope of this straight line is $\frac{1}{v_1}$. This straight line is crossed by another straight line (green). This travel time belongs to the refracted wave, also called head wave, which strikes the boundary between the layers at the critical angle i_c, propagates along the boundary at velocity v_2, and radiates energy back to the surface. Since the head wave only exists when the critical angle is reached, it can only be registered from a certain distance X_c from the source, with $X_c = 2h_0\ tan\ i_c$. The point of intersection of the two straight lines is called the crossover distance X_{cross}. The crossover distance X_{cross} is the distance at which the head wave and direct wave have the same travel time. From that distance on the head wave will arrive first.

$$X_{cross} = 2h_0 \frac{\sqrt{v_2+v_1}}{\sqrt{v_2-v_1}}\ .$$

The thickness h_0 is determined from the intercept t_0 of the head wave time-distance line as follows

$$h_0 = \frac{v_1 t_0}{2\cos i_C}\ .$$

This model can be transferred from the two-layer case to the multi-layer case. For a model consisting of n uniform layers of thickness h_j and seismic velocities v_j the travel time for a wave refracted along the boundary on top of the mth layer is

$$t = \sum_{j=1}^{m-1} \left(\frac{2h_j}{v_j} \sqrt{1 - \frac{v_j^2}{v_m^2}} \right) + \frac{x}{v_m} \quad \text{with } v_j < v_m.$$

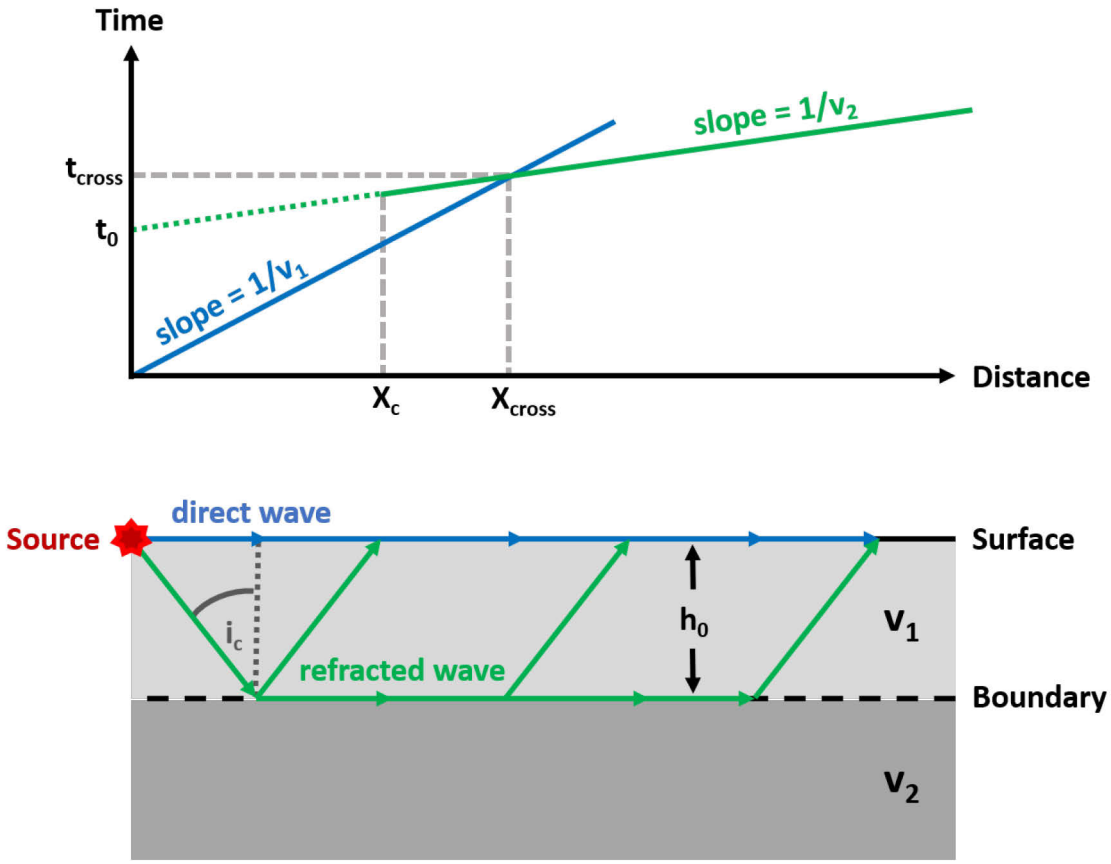

Figure 7: Refraction seismics.

Dipping layers

The reality is much more complex in most cases and you will not find a perfectly horizontal stratification, but rough layer interfaces. To the first order, we can use the model of „dipping layers", for which analytical expressions are available. If we assume an inclination angle δ for the first interface, we obtain for the travel time of the head wave :

$$t_d = \frac{2h_d}{v_1}\sqrt{1+\frac{v_1^2}{v_2^2}} + \frac{x}{v_1}\sin(i_c+\delta)$$

with h_d being the perpendicular distance from the surface point to the interface. In this case the head wave velocity is v_d:

$$v_d = \frac{v_1}{\sin(i_c+\delta)}$$

v_d is less than $v_2 (= v_1/\sin i_c)$. In this case, the fact that the layer is dipping cannot be obtained from this representation alone. For this, the refraction line must be kind of reversed, i.e. the receiver and the shot point must swap places. The travel time for the head wave is now calculated as:

$$t_u = \frac{2h_u}{v_1}\sqrt{1+\frac{v_1^2}{v_2^2}} + \frac{x}{v_1}\sin(i_c - \delta)$$

with h_u being the perpendicular distance from the new surface point to the interface. The new head wave velocity is v_u:

$$v_u = \frac{v_1}{\sin(i_c - \delta)}$$

and v_u greater than the true velocity of the lower layer v_2. In this way the true velocity of the dipping layer v_2 can be calculated for small dip angles δ:

$$\frac{1}{v_2} = \frac{\sin i_c}{v_1}$$
$$= \frac{1}{2}\left(\frac{1}{v_d} + \frac{1}{v_u}\right)$$

If the dipping layers are deeper than directly at the first boundary, the contributions of the layers above must be included (Fowler, 1990).

Hidden layers

In some cases distinct layers cannot be resolved by analysis of first arrival times, these are called "hidden layers".

For example, a low-velocity layer cannot be resolved, because their upper interface does not generate head waves, since the refracting rays bend towards the normal ($v_{j-1} = v_j$). Thus, evidence for a low-velocity layer can only come from reflections at its upper interface, and from reflections and head waves from its lower interface. The layer will express itself by different offsets of arrivals but would not be recognizable as a distinct layer.

Another type of a hidden layer is a very thin layer which is underlain by a layer with much larger velocity than the layer above ($v_{j-2} < v_{j-1} \ll v_j$). Even though head waves would travel as in the usual refraction case, waves from the very thin intermediate layer would not be resolvable as first arrivals.

In both cases, therefore, evaluation of arrival time data would not help to identify "Hidden Layers", which may require more sophisticated seismic experiments, involving the detection and mapping of seismic reflections.

2.4 Seismic data and filters

As with almost all time-dependent data, an important part of seismic data interpretation is signal filtering.

Usually a seismic signal contains a combination of signal and noise. The signal represents an actual geological feature of interest, whereas random or coherent noise may originate from different sources, including natural sources, or from the mechanical or electronic seismic equipment. Noise would affect e.g. recognition of seismic arrivals and making arrival time readings. Typically, filtering is used to improve the signal-to-noise ratio. In the simple case, these are lowpass-, high-pass- and band-pass

filters. However, more complex filtering methods are also finding increasing application in seismology. For example, Kalman filters, also known as linear quadratic estimation, minimizes the mean square error of estimated parameters. They are used in filtering seismic data, initially only for deconvolution purposes, but it has been shown that they can also be used to suppress harmonic interference in seismic traces (Frischmuth, 1998).

Another filter that is increasingly used in seismic applications is the Wiener filter (Wiener, 1949), a so-called error prediction filter. Thus, the Wiener filter can be used to suppress the noise in a corrupted signal to obtain an estimate of the underlying useful signal. It performs optimal noise reduction by minimizing the mean square error between the estimated random noise and the desired output.

The input signal for the Wiener filter is a signal $s(t)$ which is disturbed by an additive noise $n(t)$.

$$y(t) = s(t) + n(t)$$

The output signal x(t) is obtained by convolution of the input signal with the filter function w(τ):

$$x(t) = w(\tau) * y(t) = w(\tau) * \big(s(t) + n(t) \big)$$

Error $e(t) = s(t+d) - x(t)$ and quadratic error $e^2 = s^2(t+d) - 2s(t+d)x(t) + x^2(t)$ result from the deviation of the output signal from the time-shifted input signal $s(t+d)$.

Let $x(t)$ be represented as a convolution integral:

$$x(t) = \int_{-\infty}^{\infty} w(\tau)[s(t-\tau + n(t-\tau)]\, d\tau$$

then the expected value of the squared error is given by:

$$E(e^2) = R_s(0) - 2 \int_{-\infty}^{\infty} w(\tau) R_{y\,s}(\tau + d)\, d\tau + \iint_{-\infty}^{\infty} w(\tau) w(\theta) R_y(\tau - \theta)\, d\tau\, d\theta$$

where R_s is the autocorrelation of $s(t)$, R_y is the autocorrelation of $y(t)$, and $R_{y\,s}$ is the cross correlation of $y(t)$ and $s(t)$. If the signal $s(t)$ and noise $n(t)$ are uncorrelated the cross correlation is zero. This leads to $R_{y\,s} = R_s$ and $R_y = R_s + R_n$. Subsequently, the goal is to minimize the quadratic error $E(e^2)$ by determining an optimal filter function $w(\tau)$ (Wiener, 1949).

2.5 From historic to modern age data

Records of historical data from the Apollo era, in this case Apollo 17, were obtained from the website of the Incorporated Research Institutions for Seismology (IRIS). Here, records of seismic data from all eight EP detonations, each recorded with the four geophones, could be downloaded in SEGY format. However, these were 15-second clips (starting with the clearly recognizable detonation signal, see Figure 8). Obviously, it was decided to shorten the data streams to the same length as the data streams of the thumper experiments of Apollo 16. Additionally, the contained raw data were contaminated by the periodic noise of the transmitter, which communicated on the same channel as the seismic data. In order to filter out these disturbing signals, a filter design was required, for which it was necessary (depending on the applied filter) to include longer data streams before the occurrence of the signal under investigation. Hence, the 15-second SEGY files were not sufficient for this approach.

NASA space mission data can be requested via the NASA Space Science Data Coordinated Archive (NSSDCA). The extensive data catalogue provided many possibilities. It was possible to get access to the original bitstreams from that resource. At first, it turned out that it was problematic to decode the binary data stream since the scheme published in the literature (see Figure 9) did not provide usable results when used. This was partly due to the fact that the data had been re-stored and re-written several times over the years and this had not always been sufficiently documentated. The further development of technical possibilities had therefore left its mark on the data. In order to restore the original data, the scheme for the evaluation of the Apollo 17 LSPE raw bitstreams was restored as part of the first research work. In the appendix of this work, the restoration scheme is described, which could be used in the future to decode the Apollo 17 LSPE raw data.

For the first (and second) research paper(s), the restored original data streams were evaluated in combination with newly identified, LRO-derived coordinates of the Apollo 17 equipment from Haase et al. (2013). This led to new velocity-depth profiles below the landing site. In addition, a link between history and modern age was created by investigating the extent to which the results change when switching from old to new data sets, or when combining these data sets.

This work was done within the framework of the Helmholtz Alliance „Robotic Exploration of Extreme Environments – ROBEX“ project, which aimed to foster collaboration between space and deep-sea research. Within this framework of ROBEX a demo mission was designed to test the developed scenarios and equipment.

During the joint work, two separate demo missions for deep-sea and space were developed. The ROBEX space scenario showed a version of the Apollo 17 LSPE as it could be performed with modern robotic technology that relied on a high degree of autonomy. One part of this was the new development of a seismic measurement platform which could be handled by an autonomously operating rover. The data recorded with the instrument must meet scientific standards regarding the quality of the data, especially the recorded noise levels. This was the subject of the third paper.

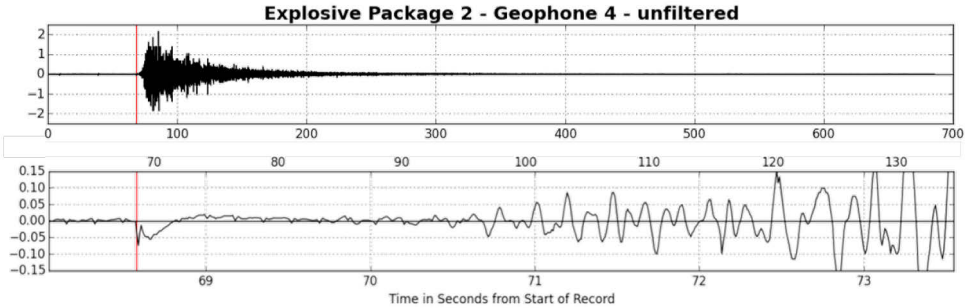

Figure 8: Seismogram of EP2 recorded with geophone 4. The red vertical line marks the clearly visible detonation signal. Upper panel shows the complete seismogram. Lower panel shows a zoomed in view where periodic noise of the transmitter is visible as small ticks in the data.

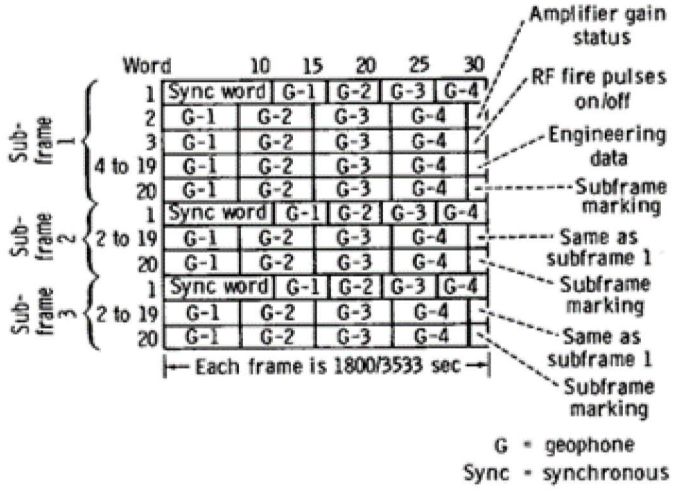

Figure 9: Depiction of the decoding scheme for LSPE data format (from NASA – Apollo 17 Preliminary Science Report, 1973).

2.6 References

Canup, R. M., & Asphaug, E. (2001). Origin of the Moon in a giant impact near the end of the Earth's formation. *Nature*, *412*(6848), 708.

Canup, R. M. (2004). Dynamics of lunar formation. *Annu. Rev. Astron. Astrophys.*, *42*, 441-475.

Chambers, J. E., & Lissauer, J. J. (2002, March). A new dynamical model for the lunar Late Heavy Bombardment. In *Lunar and Planetary Science Conference* (Vol. 33).

Chin, G., Brylow, S., Foote, M., Garvin, J., Kasper, J., Keller, J., ... & Robinson, M. (2007). Lunar reconnaissance orbiter overview: The instrument suite and mission. *Space Science Reviews*, *129*(4), 391-419.

Dorman , J., Evans, S., Nakamura, Y., & Latham, G. (1978). On the time-varying properties of the lunar seismic meteoroid population. Lunar and Planetary Science Conference, 9th, Houston, Tex., March 13-17, 1978, Proceedings. Volume 3. (A79-39253 16-91) New York, Pergamon Press, Inc., 1978, p. 3615-3626.

Duennebier, F., & Sutton, G. H. (1974). Thermal moonquakes. *Journal of Geophysical Research*, *79*(29), 4351-4363.

Frohlich, C., & Nakamura, Y. (2009). The physical mechanisms of deep moonquakes and intermediate-depth earthquakes: How similar and how different?. Physics of the Earth and Planetary Interiors, 173(3-4), 365-374.

Fowler, C. M. R. (1990). 4.3 Refraction Seismology. The solid earth: an introduction to global geophysics. (p. 140-156), Cambridge University Press.

Frischmuth, Ulf. (1998) Das erweiterte Kalman-Filter zur Unterdrückung harmonischer Störsignale in der Seismik. Papierflieger.

Gagnepain-Beyneix, J., Lognonné, P., Chenet, H., Lombardi, D., & Spohn, T. (2006). A seismic model of the lunar mantle and constraints on temperature and mineralogy. *Physics of the Earth and Planetary Interiors*, *159*(3-4), 140-166.

Haase, I., Gläser, P., Knapmeyer, M., Oberst, J., & Robinson, M. S. (2013, March). Improved Coordinates of the Apollo 17 Lunar Seismic Profiling Experiment (LSPE) Components. In Lunar and Planetary Science Conference (Vol. 44, p. 1966).

Haase, I., Wählisch, M., Gläser, P., Oberst, J., & Robinson, M. S. (2019). Coordinates and Maps of the Apollo 17 Landing Site. *Earth and Space Science*, *6*(1), 59-95.

Heiken, G. H., Vaniman, D. T., & French, B. M. (1991). Lunar sourcebook-A user's guide to the moon. Research supported by NASA, Cambridge, England, Cambridge University Press, 1991, 753 p. No individual items are abstracted in this volume.

Hörz et al. (1991), Lunar Surface Processes. The Lunar Sourcebook, pp. 62-120.

Ishihara, Y., Goossens, S., Matsumoto, K., Noda, H., Araki, H., Namiki, N., ... & Sasaki, S. (2009). Crustal thickness of the Moon: Implications for farside basin structures. *Geophysical Research Letters*, *36*(19).

Khan, A., Mosegaard, K., & Rasmussen, K. L. (2000). A new seismic velocity model for the Moon from a Monte Carlo inversion of the Apollo lunar seismic data. *Geophysical Research Letters*, *27*(11), 1591-1594.

Koyama, J., & Nakamura, Y. (1980). Focal mechanism of deep moonquakes. In Lunar and Planetary Science Conference Proceedings (Vol. 11, pp. 1855-1865).

Latham, G., Ewing, M., Dorman, J., Lammlein, D., Press, F., Toksoz, N., ... & Nakamura, Y. (1971). Moonquakes. Science, 174(4010), 687-692.

Latham, G., Ewing, M., Dorman, J., Lammlein, D., Press, F., Toksöz, N., ... & Nakamura, Y. (1972). Moonquakes and lunar tectonism. The moon, 4(3-4), 373-382.

Lognonné, P., Gagnepain-Beyneix, J., & Chenet, H. (2003). A new seismic model of the Moon: implications for structure, thermal evolution and formation of the Moon. *Earth and Planetary Science Letters*, *211*(1-2), 27-44.

Mackin, J. H. (1969). Origin of lunar maria. Geological Society of America Bulletin, 80(5), 735-748.

Nakamura, Y., Latham, G., Lammlein, D., Ewing, M., Duennebier, F., & Dorman, J. (1974). Deep lunar interior inferred from recent seismic data. *Geophysical Research Letters*, *1*(3), 137-140.

Nakamura, Y., Dorman, J., Duennebier, F., Lammlein, D., & Latham, G. (1975). Shallow lunar structure determined from the passive seismic experiment. *The Moon*, *13*(1-3), 57-66.

Nakamura, Y. (1977). HFT events: Shallow moonquakes?. Physics of the Earth and Planetary Interiors, 14(3), 217-223.

Nakamura, Y., Latham, G. V., Dorman, H. J., Ibrahim, A. B., Koyama, J., & Horvath, P. (1979). Shallow moonquakes-depth, distribution and implications as to the present state of the lunar interior. In Lunar and Planetary Science Conference Proceedings (Vol. 10, pp. 2299-2309).

Nakamura, Y., Latham, G. V., & Dorman, H. J. (1982). Apollo lunar seismic experiment—Final summary. *Journal of Geophysical Research: Solid Earth*, *87*(S01), A117-A123.

Nakamura, Y. (1983). Seismic velocity structure of the lunar mantle. Journal of Geophysical Research: Solid Earth, 88(B1), 677-686.

NASA Public Affairs, (1969). Apollo 11 Press Kit.

Oberst, J. (1987). Unusually high stress drops associated with shallow moonquakes. *Journal of Geophysical Research: Solid Earth*, *92*(B2), 1397-1405.Oberst, J. and Nakamura, Y. (1991). A search for clustering among the meteoroid impacts detected by the Apollo lunar seismic network. Icarus (Vol. 91, Issue 2, pp. 315-325).

Shoemaker, E. M. (1962). Interpretation of lunar craters. *Physics and Astronomy of the Moon*, 283-359.

Schultz, P. H. (1976). Floor-fractured lunar craters. *The Moon*, *15*(3-4), 241-273.

Toksöz, M. N., Dainty, A. M., Solomon, S. C., & Anderson, K. R. (1973). Velocity structure and evolution of the Moon. In *Lunar and Planetary Science Conference Proceedings* (Vol. 4, p. 2529).

Vermillion, R. E. (1975). On the center-of-mass offset of the moon. American Journal of Physics Vol. 44, 1014.

Weber, R. C., Lin, P. Y., Garnero, E. J., Williams, Q., & Lognonne, P. (2011). Seismic detection of the lunar core. science, 331(6015), 309-312.

Weber, R. C. (2014). Interior of the Moon. T. Spohn, D. Breuer and T. V. Johnson (Eds.). Encyclopedia of the Solar System (Third Edition), pp. 539-554. Elsevier. Wetherill, G. W. (1975). Late heavy bombardment of the moon and terrestrial planets. In *Lunar and Planetary Science Conference Proceedings* (Vol. 6, pp. 1539-1561).

Wiener, N. (1949). Extrapolation, interpolation, and smoothing of stationary time series: with engineering applications (Vol. 113, No. 21, pp. 1043-54). Cambridge, MA: MIT press.

Young, E. D., Kohl, I. E., Warren, P. H., Rubie, D. C., Jacobson, S. A., & Morbidelli, A. (2016).

Oxygen isotopic evidence for vigorous mixing during the Moon-forming giant impact. Science, 351(6272), 493-496.

3. Research Paper I

Re-evaluation of Apollo 17 Lunar Seismic Profiling Experiment data

Alexandra Heffels[a], Martin Knapmeyer[a], Jürgen Oberst[a,b], Isabel Haase[c]

a German Aerospace Center - Institute for Planetary Research, Berlin, Germany

b Moscow State University for Geodesy and Cartography (MIIGAiK), 105064 Moscow, Russia

c Technical University Berlin, Berlin, Germany

The final publication is available at Elsevier via

http://dx.doi.org/10.1016/j.pss.2016.11.007.

Abstract

We re-analyzed Apollo 17 Lunar Seismic Profiling Experiment (LSPE) data to improve our knowledge of the subsurface structure of this landing site. We use new geometrically accurate 3-D positions of the seismic equipment deployed by the astronauts, which were previously derived using high-resolution images by Lunar Reconnaissance Orbiter (LRO) in combination with Apollo astronaut photography. These include coordinates of six Explosive Packages (EPs) and four geophone stations. Re-identified P-wave arrival times are used to calculate two- and three-layer seismic velocity models. A strong increase of seismic velocity with depth can be confirmed, in particular, we suggest a more drastic increase than previously thought. For the three-layer model the P-wave velocities were calculated to 285, 580, and 1825 m/s for the uppermost, second, and third layer, respectively, with the boundaries between the layers being at 96 and 773 m depth. When compared with results obtained with previously published coordinates, we find (1) a slightly higher velocity (+4%) for the uppermost layer, and (2) lower P-wave velocities for the second and third layers, representing a decrease of 34% and 12% for second and third layer, respectively. Using P-wave arrival time readings of previous studies, we confirm that velocities increase when changing over from old to new coordinates. In the three-layer case, this means using new coordinates alone leads to thinned layers, velocities rise slightly for the uppermost layer and decrease significantly for the layers below.

3.1 Introduction

3.1.1 Apollo 17 mission

NASA's early lunar exploration culminated in the sixth manned landing of Apollo 17. The mission was launched on December 7, 1972 and touched down on the lunar surface on December 11, before returning safely to Earth eight days after (Figure 10).

During their stay on the lunar surface, the astronauts deployed several scientific experiments which represent a unique source of lunar ground truth up to the present day. Among other experiments, they deployed the Apollo 17 Lunar Seismic Profiling Experiment (LSPE) which consisted of an array of four identical geophones of the moving coil type with a natural frequency of 7.5 Hz (Vostreys, 1980), set up in a Y-shaped array (see Figure 11, p. 18), and a set of eight explosive packages (EP). The eight EPs were built identically except for the amount of explosives used and the securing mechanical timers (Table A1, Appendix). A mixture of HNS (Hexanitrostilbene) and Teflon (90%/ 10%) was used as explosive substance (Kilmer and Laboratory, 1973). All EPs were detonated remotely after the astronauts had left the lunar surface (Figure 12).

The purpose of the LSPE was to record seismic waves generated by detonations of the eight EPs, the thrust of the Lunar Module's ascent stage during launch, and upon its impact. In addition, a secondary objective was the monitoring of seismic waves generated by natural events.

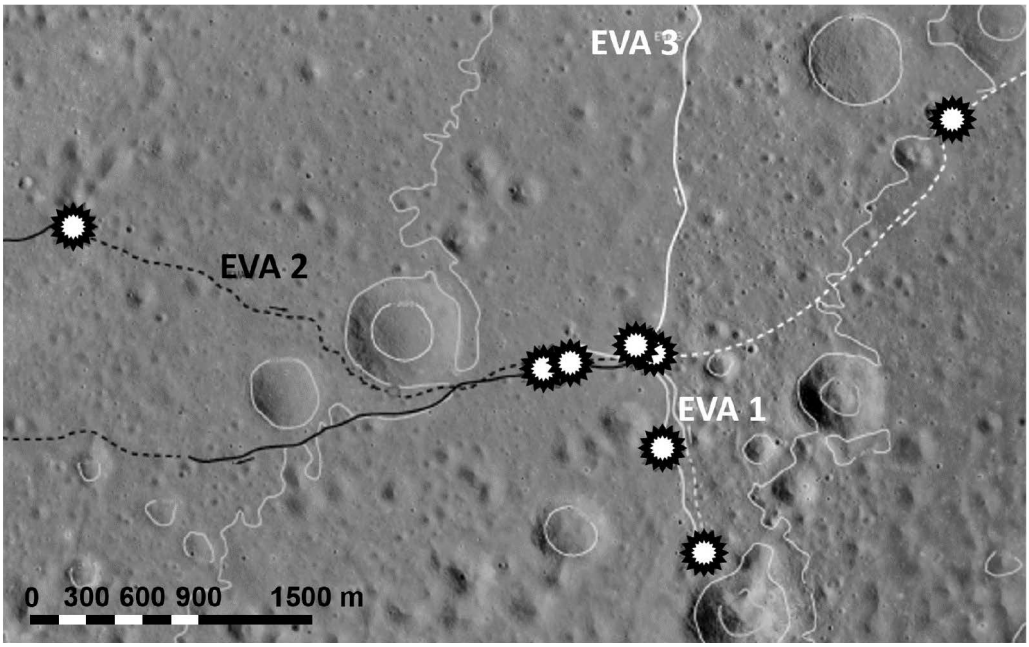

Figure 10: Mosaic of LROC-images of Apollo 17 landing site with depicted paths for extravehicular activities (EVA) of the astronauts. Stars mark the positions of explosive packages. Some contour lines added to give terrain overview.

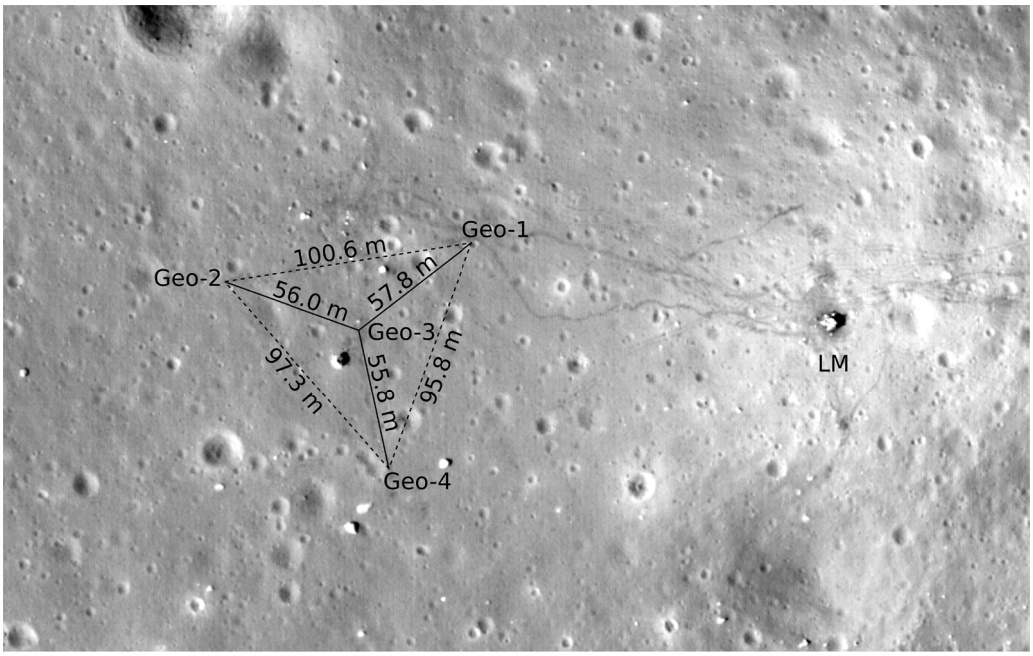

Figure 11: Apollo 17 landing site with Y-shaped array. Geophone-array with point distances marked. Position of Lunar Module (LM) to the right side of the array. Foot tracks of astronauts are clearly visible between array and LM.

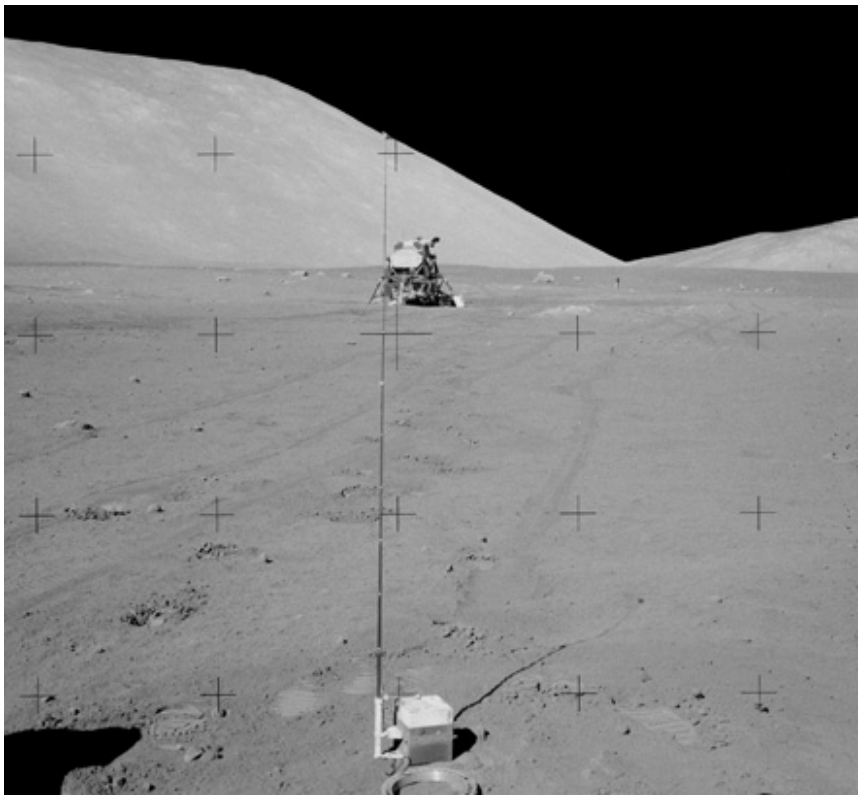

Figure 12: Picture of EP8 with extended antenna and Lunar Module in the background. Distance between EP8 and Lunar Module approximately 290 m. Size of EP with extended antenna 157.48 cm (NASA, 1972). Astronauts took pictures of the equipment during their extravehicular activities (NASA).

3.1.2 Lunar Reconnaissance Orbiter

In 2009, the Lunar Reconnaissance Orbiter (LRO) mission was launched. From a near-circular polar orbit, LRO Narrow Angle Camera (NAC) mapped the lunar surface at a maximum resolution of 50 cm/pixel. This allowed a detailed mapping of Apollo landing sites and reconstruction of the geometry of the deployed seismic array. Geometrically accurate coordinates (lat /long/heights) were determined by combination of these high-resolution orthoimages with Apollo surface panoramas taken by the astronauts (Haase et al., 2013). With this method it was possible to determine new geometrically accurate coordinates for six of the eight EPs. The positions of EP1 and EP7 could not be determined. Since the images where these devices are seen lack distinctive landmarks, it is not possible to reconstruct their accurate coordinates.

New LROC-derived coordinates of seismic equipment differ from previously published coordinates by up to 40 m. In addition, the new LROC-derived coordinates include topographic height information (differences in height in the range of 35 m (Haase et al., 2013)) not available before.

In this paper, we re-analyze the seismic data using new seismic arrival time readings and coordinate information to update seismic velocity depth profiles at the Apollo 17 site (Figure 13).

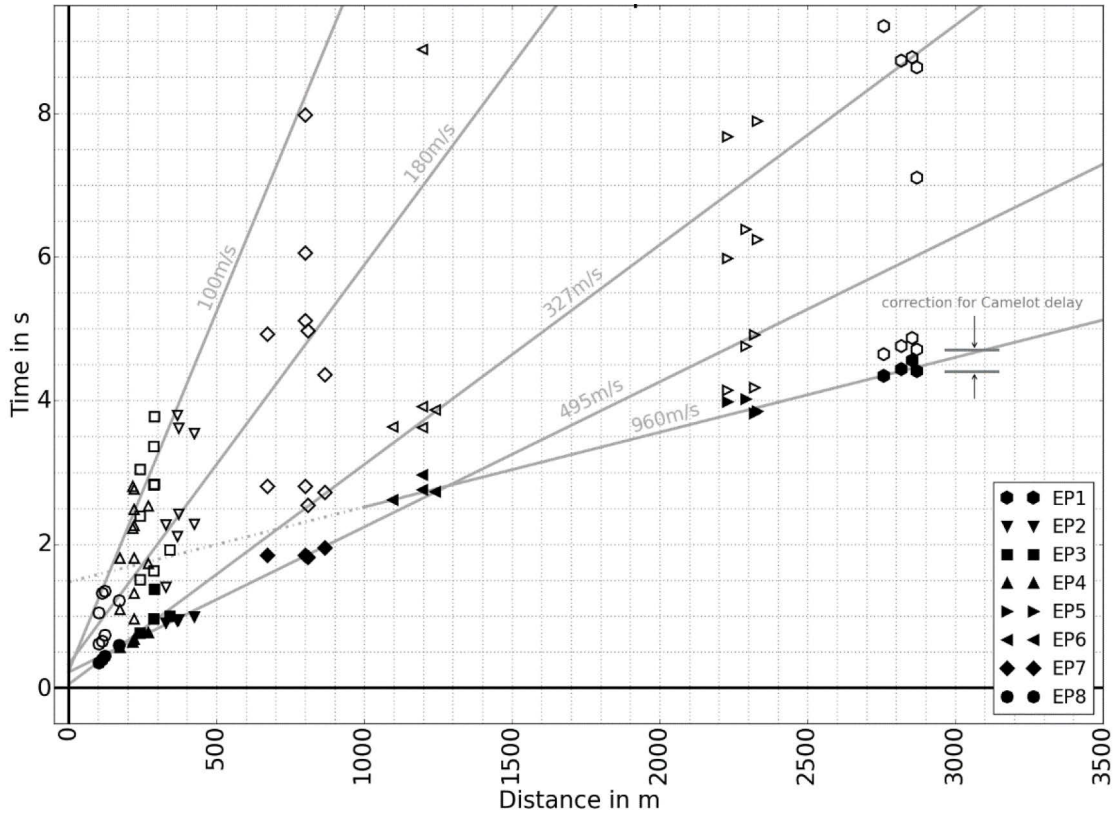

Figure 13: Apollo 17 travel time curves (Cooper et al., 1974). Original numerical data for P-wave first arrivals was kindly provided by Kovach (pers. communication). Remaining secondary arrival times were digitized from a printed version of the figure 13 in the paper by Cooper et al. (1974). Correction for delay in travel times caused by Camelot crater is marked on right side of the plot. Filled markers depict first arrivals, unfilled markers depict other phase arrivals, grey lines show slopes with the suggested velocities of 100, 180, 327, 495, and 960 m/s.

3.2 Method

3.2.1 Cooper model

Cooper et al. (1974) presented a five-layer model with the velocities being 100, 327, 495, 960, and 4700 m/s (Figure 14). The seismic velocity of the uppermost layer (100 m/s) was adopted from thumper data acquired at the Apollo 14 and 16 sites. Unfortunately, there were no thumper experiments conducted during Apollo 17 mission. The existence of the deepest 4700 m/s layer was inferred from the P-wave arrival times of the Apollo 17 LM impact recorded with the LSPE. Nakamura (2011) proved that there was a timing error in the data and therefore this layer is not existent as stated before. Original P-wave arrivals (plotted, but not listed in early publications) were kindly provided by Kovach (pers. communication, 2015). The numerical values for new and old P-wave arrival times can be found in Table A2 in the appendix. Unfortunately, the associated arrival times of other than first arrivals were not available.

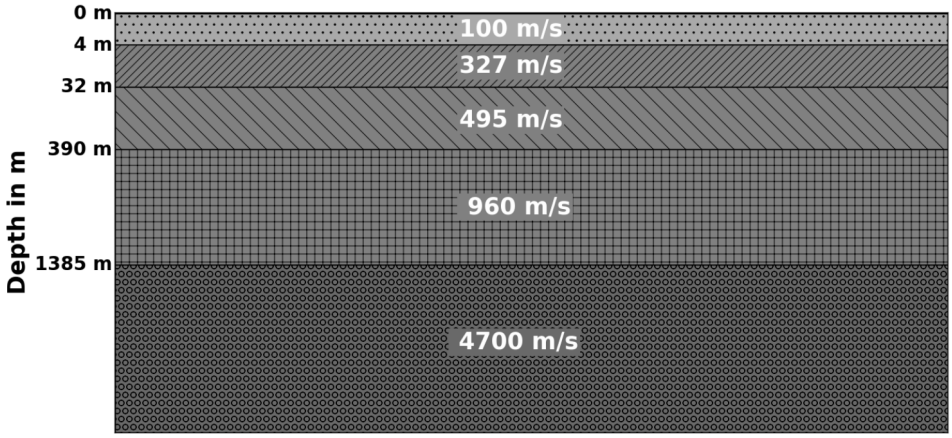

Figure 14: Depiction of the velocity-depth model from Cooper et al. (1974).

3.2.2 Arrival time readings

Seismic signals traveling within the Moon are affected by strong scattering. Hence, raw seismograms show feature-less spectra, emergent arrivals, and long signal decay times, impeding the identification of secondary phases (Cooper and Kovach, 1975; Duennebier and Sutton, 1974). Furthermore, periodic noise generated by the transmitter contaminated all recorded signals (Cooper et al., 1974). Since, it is almost impossible to identify first arrivals in raw data plots, we had to use different digital techniques to improve visibility of first arrivals. In order to remove possibly occurring trends, the mean of data was subtracted on every single trace. While original data analysis used unspecified prediction error filter, we decided to use a Wiener filter. The Wiener filter is a prediction error filter designed from an autocorrelation function estimated from a short data sample. We varied the size of Wiener filter window from 5 to 15 in each dimension, and the noise-power from an estimated average to fixed values of 0.5 and 10 for the local variance input to find the best fitting approach. The filtered records provided a basis for new readings of P-wave arrival times (see Figure 15).

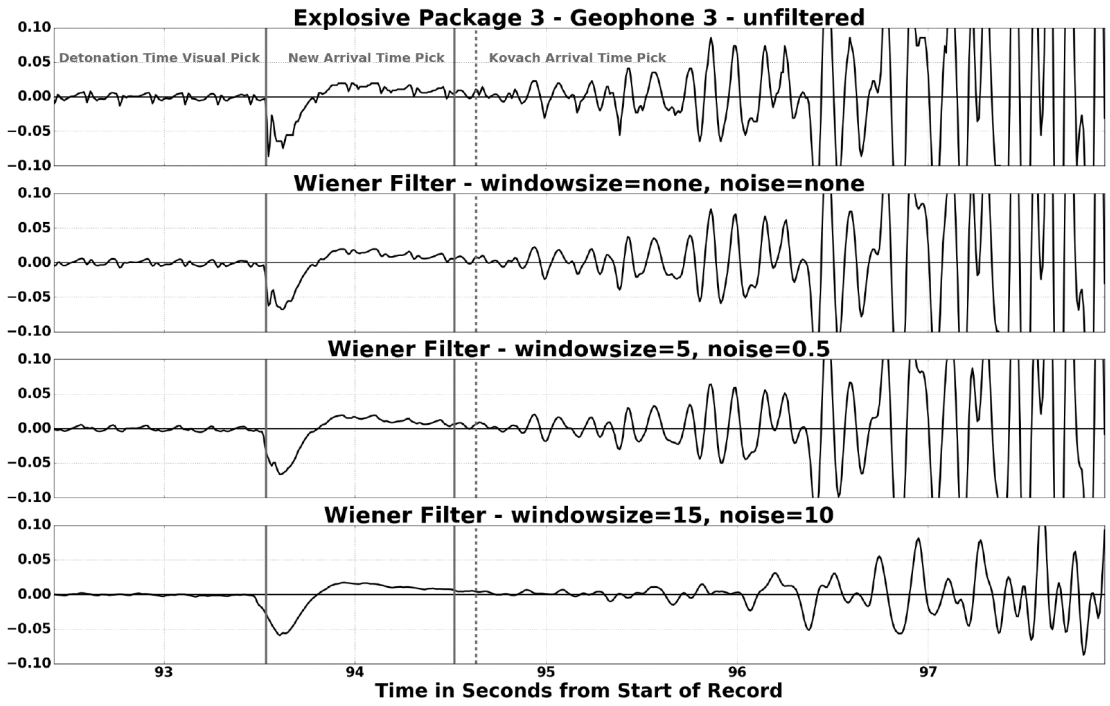

Figure 15: Seismogram plots of EP3 detonation recorded with geophone 3. The uppermost plot shows raw data. The plots below show different Wiener filters applied to find first arrival picks. The electronic detonation impulse is clearly visible as a strong peak in the data. The bold line marks our visual picks of detonation- and seismic wave arrival times. The dashed line in grey marks the arrival time pick from Kovach (pers. communication, 2015).

3.2.3 Travel time function and depth profiles

The new Lunar Reconnaissance Orbiter Camera (LROC)-based point distances from Haase et al. (2013) are available for six of the eight Explosive Packages (EPs). Hence, to work with a self-consistent data set we only use the EPs where old and new coordinates are existent. Therefore, we plotted the first arrivals against the distances from the four geophones for the detonations of EP2, EP3, EP4, EP5, EP6, and EP8.

Travel time inversions were carried out using our new arrival time readings in combination with LROC-based point distances from Haase et al. (2013). Previous arrival time (Kovach, 2015) and coordinate data (Cooper and Kovach,1975) were used for comparison.

The combination of old and new coordinates with old and new travel time readings led to four different combinations: (a) new travel time readings from this study with point distances from Haase et al. (2013), (b) new travel time readings with point distances from Cooper and Kovach (1975), (c) old Kovach's travel time readings with point distances from Haase et al. (2013), and (d) old Kovach's travel times readings with point distances from Cooper and Kovach (1975).

As mentioned before Cooper et al. (1974) purposed a five-layer model (Figure 14). In this model the uppermost layer with a velocity of 100 m/s was derived from Apollo 14 and 16, and the last layer with a velocity of 4700 m/s was proven to be in error by Nakamura (2011). Neglecting these two layers would result in a three-layer model. It was readily apparent that it was possible to fit a straight line through the arrivals from the four closest detonations (EP2, EP3, EP4, and EP8), which represented the

first layer in all models. But as mentioned above, we decided to neglected EP1 and EP7 in order to work with a selfconsistent data set. In the three-layer case this means that second and third layers are only determined by four points (one EP recorded with all four geophones). Four points may seem to be a small data set to determine a layer. Therefore, we decided to also evaluate EP5 and EP6 as points on one straight line instead of two separated lines. This led to two-layer models. The reciprocal value of the slopes represented the velocity of the layer, while the thicknesses of these layers were calculated from intercept times, using standard equations for refraction seismics (e.g., Telford et al., 1990).

Examination of the residuals, e.g. in lag plots or histograms, served as a quality check for all cases. A random pattern in the residuals would support a linear model, which in this case means that our linear regression model to determine the slopes was sufficiently accurate. This would be supported by a normal distribution in the residuals histogram plots. Additionally, a residual lag plot would serve as a check for randomness in distribution of residuals, proving appropriateness of the regression models used. Residual plots, histogram plots, and residual lag plots can be found in the appendix (Figures 21-25).

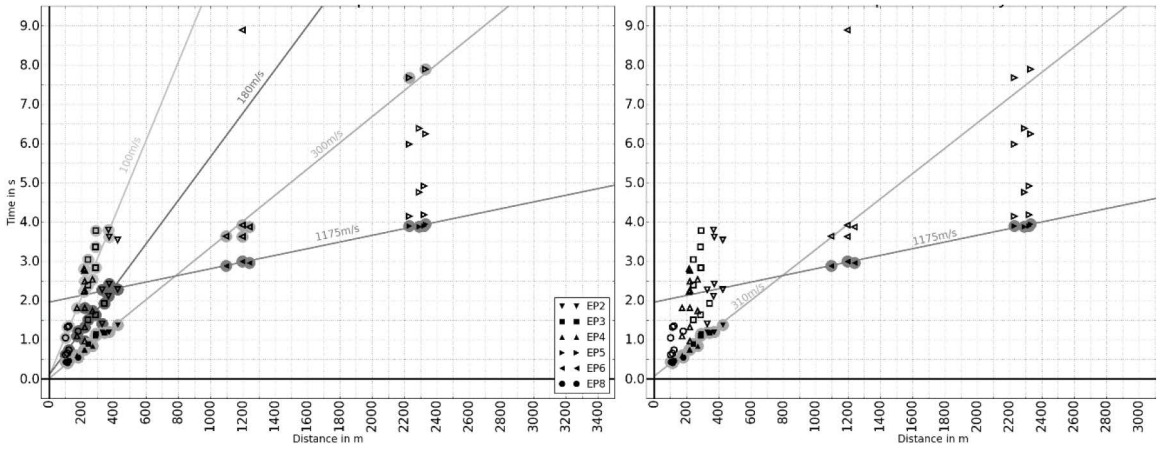

Figure 16: Comparison of data points and fitted linear travel time functions. Only points of the self-consistent data set are depicted here, this means points of EP1 and EP7 are not shown. Points with background circles used for slope determination. Filled markers depict first arrivals, unfilled markers depict other phase arrivals, grey lines show new calculated slopes. Original numerical data for P-wave first arrivals was kindly provided by Kovach (pers. communication, Table A2 in appendix). Remaining other phase arrival times were digitized from a printed version of the figure 13 in the paper by Cooper et al. (1974). Left: Lines were fitted through all suitable points irrespective of phase. Right: Lines were fitted only through first arrival points. Fitting lines through the new obtained points for first and later phase arrivals leads to velocities of 100, 180, 300, and 1175 m/s if all different phase arrivals are used (left side). When using first arrivals only, the two lowest velocity slopes for 100 and 180 m/s cannot be detected since these are solely constrained by later phase arrivals (right side). This means, neglecting points of EP1, EP7, and the LM impact favors a two layered model.

3.3 Results

3.3.1 Two-layer case

(Figure 16) The velocity and depth of the uppermost layer was well constrained by data from four EPs (EP2, EP3, EP4, and EP8) recorded by all four geophones. For the velocity of the second layer only detonations of two charges (EP5 and EP6) were taken into account.

When using our new arrival time readings and new LROC-based coordinates, we find velocities of 285 and 775 m/s for the two layers, respectively, with the depth of the first layer at 170 m. Using the early travel time readings from Kovach (pers. communication, 2015), we obtained velocities of 320 and 1150 m/s for the first and second layer, respectively, with the transition between the two layers at 324 m.

For comparison we also used the previous coordinates from Cooper and Kovach (1975) in combination with our new arrival time readings. In this case the velocities of the layers were 275 and 790 m/s for the first and second layer, respectively, and a layer boundary at 169 m. Using the Kovach travel time readings, this led to velocities for the first and second layer of 310 and 1175 m/s, respectively, and a transition at a depth of 316 m (see Figure 17).

Evaluating the residuals, the histogram of residuals, and the residual lag plot for each of the four cases showed that for both layers the variance of the residuals is constant and the histograms of the residuals showed a normal distribution (appendix, Figures 21 and 22). And, the random errors were independent from each other as shown in the residual lag plots (appendix, Figures 21 and 22, lower panels).

We used these plots for calculating a set of depth profiles, shown in Figure 17.

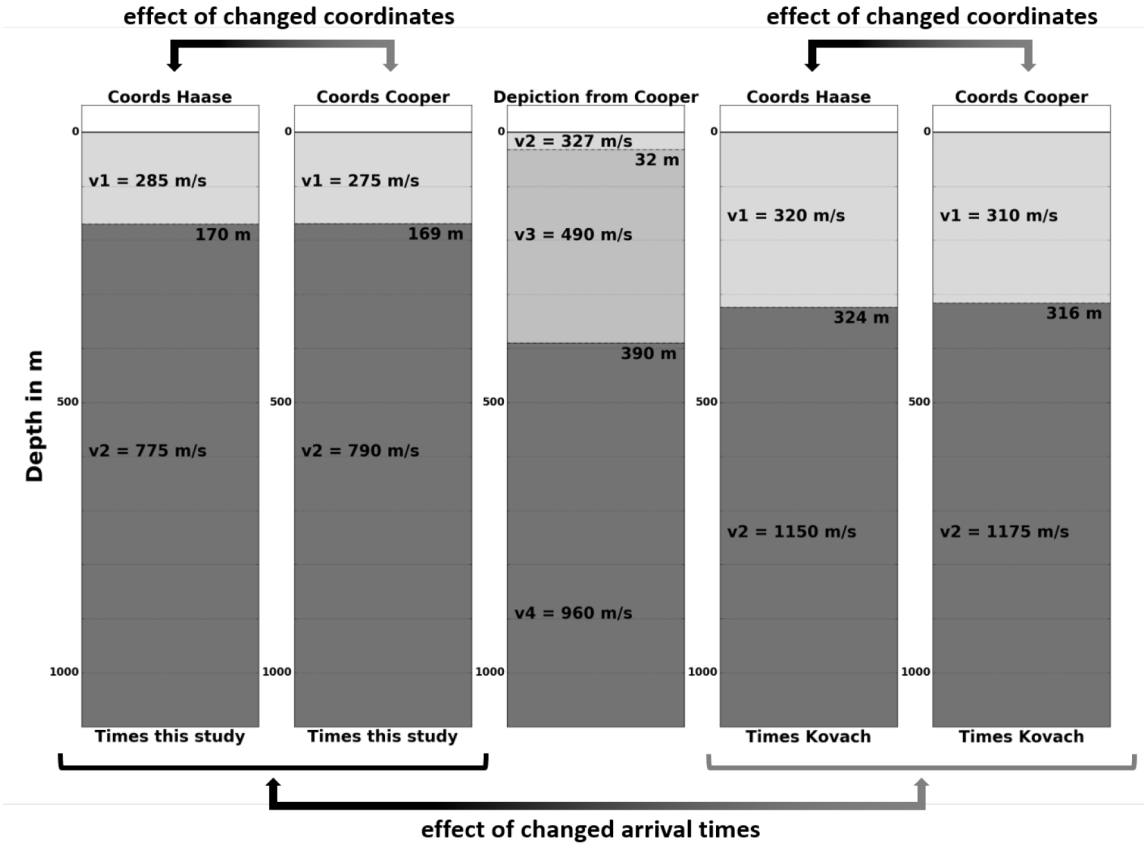

Figure 17: Comparison of depth models for the two-layer case. The column in the middle represents the velocity-depth profile of Cooper et al. (1974); for better readability of the figure the uppermost 100 m/s-layer with a thickness of 4 m and the lowest 4700 m/s-layer at a depth of 1385 m depth are not depicted here. Left side columns were generated with new travel time readings from this study. Right side columns were generated with travel time readings from Kovach (pers. communication, 2015). For better readability no error bars are denoted in this plot. In the two-layer case, almost no change in layer thickness is observable when changing over from old to new coordinates. Trends in the velocity changes are equal to the three-layer case: velocities slightly rise for the uppermost layers. In contrast, P- wave velocities for the layer below decrease.

3.3.2 Three-layer case

Again, the velocity and depth of the uppermost layer was well constrained by data from four EPs (EP2, EP3, EP4, and EP8) recorded by all four geophones. However, for the second layer (which includes velocity and depth) and the velocity of the third layer only one single shot was taken into account, respectively.

When the new travel time readings were combined with the coordinates by Haase et al. (2013) the P-wave velocities were 285 m/s, 580 m/s, and 1825 m/s for first, second, and third layer, respectively, with transitions between the layers at depths of 96 and 773 m (Figure 18). In contrast, when the new arrival time readings from this study and the coordinates of Cooper and Kovach (1975) were used in combination, we obtained the velocities as 275 m/s, 876 m/s, and 2073 m/s for first, second, and third layer, respectively, and transitions between the layers at depths of 188 and 986 m.

For comparison, we calculated the velocities depth models with travel time readings from Kovach (pers. communication, 2015). When combining the old travel time readings from Kovach with the Haase et al. (2013) coordinates, the P-wave velocities were 322, 1053, and 2750 m/s for first, second, and third layer, respectively. The transitions between the layers were calculated to depths of 310 and 1022 m. When combining Kovach's travel time readings with the early coordinates from Cooper and Kovach (1975), these velocities were 315, 1410, and 3155 m/s for first, second, and third layer, respectively, with layer

boundaries at depths of 340 and 1174 m. Evaluation of the residuals, the histogram of residuals, and the residual lag plot for each of the four cases showed that for all three layers the residuals were evenly distributed above and below the reference line at 0. The histograms of the residuals showed a normal

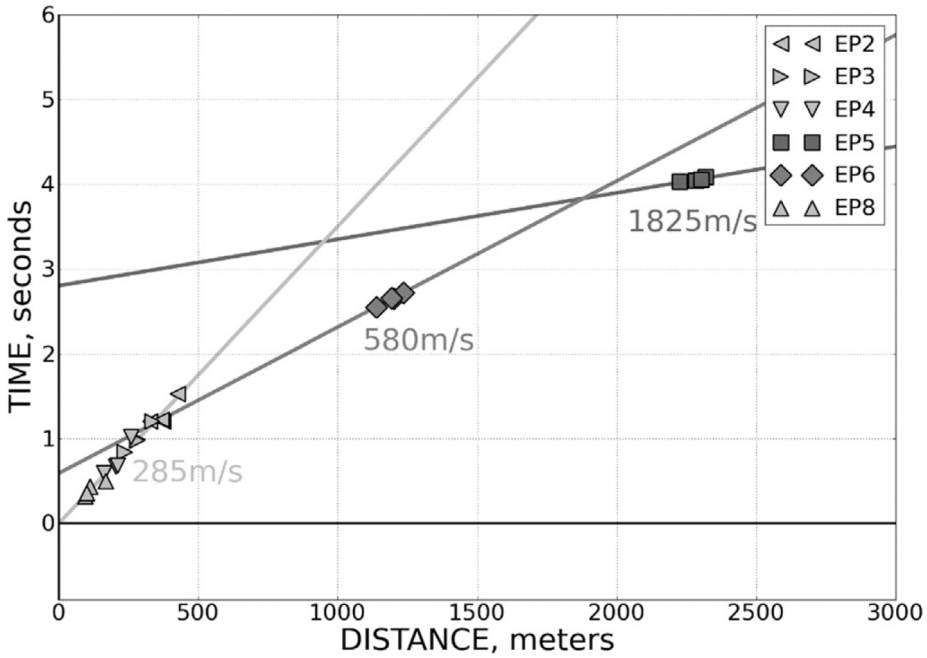

Figure 18: Travel time plot for data from this work. The light grey line represents the best fitting line through data points of EP2, EP3, EP4, and EP8. The reciprocal slope of this line gives a P-wave velocity of 285 m/s. Best fitting lines for EP6 and EP5 are depicted in separated lines. These slopes lead to P-wave velocities of 580 m/s for the second layer and 1825 m/s for the third layer.

distribution. And, the random errors were independent from each other as shown in the residual lag plots (see appendix, Figures. 23-25).

3.4 Discussion

Further improvements to our models may become available, if positions of EP1, EP7 and the Lunar Module (LM) impact can be found. Identification of EP1 and EP7 in images from current lunar spacecraft is not likely. LRO is currently moving in a "frozen orbit" at higher altitude than in its early mission, from where landing site studies at the previous high image resolution is not possible. Hence, we must await mapping of Apollo landing sites by future missions with imaging from more favorable orbits. From our modeling, EP7 and EP1, appear to lie in the transition for the first/second layer and the second/third layer, respectively. Including the missing position data of EP1, EP7, and the LM impact will help to determine more precisely the transitions between the three layers, and the seismic velocity structure beneath the Apollo 17 landing site.

When analyzing lunar farside deep moonquakes for investigation of the deep lunar interior, Nakamura (2005) noticed that the featureless spectra of lunar seismograms make them hard to read and different seismologists working on the same data set will pick different times for first arrivals. It is likely to be similar with the investigations of this study. Hence, variations in total values are hard to compare but trends can be observed and will be discussed below. For both, the two- and three-layer case, we see that P-wave velocities for the upper layer become larger, when new coordinates are used, whereas P-wave velocities for lower layers decrease significantly.

3.4.1 Two-layer case

In the two-layer case, when using coordinates from Cooper and Kovach (1975) velocities of uppermost layers are lower whereas velocities of second layers are higher than results calculated with new LROC-derived coordinates from Haase et al. (2013). For coordinates by Cooper and Kovach (1975) we calculate the P-wave velocities of uppermost layers to be 310 and 275 m/s for arrival time picks from Kovach (pers. communication, 2015) and from this study, respectively. For second layers the P-wave velocities can be calculated to be 1175 and 790 m/s for old and new arrival time picks, respectively. When using coordinates from Haase et al. (2013), P-wave velocities of uppermost layers are higher (+10 m/s) and for second layers lower (−25 m/s for early Kovach arrival time picks and −15 m/s for arrival time picks from this study). The layer thickness remains almost constant when using one set of arrival time picks irrespective of coordinates used (see Figure 17).

Regardless of the travel times used, the velocities were only slightly higher for uppermost layers but dropped significantly for other layers when using new instead of early coordinates.

3.4.2 Three-layer case

When using coordinates from Cooper and Kovach (1975) velocities of uppermost layers are lower whereas velocities of second and third layers are significantly higher than in the case of new LROC-derived coordinates from Haase et al. (2013). For Cooper's coordinates we calculate the P-wave velocities of uppermost layers to be 310 and 275 m/s for arrival time picks from Kovach (pers. communication, 2015) and from this study, respectively. For second layers the P-wave velocities can

be calculated to be 1174 and 876 m/s for old and new arrival time picks, respectively, and for third layers the P-wave velocities are 3155 and 2074 m/s for old and new arrival time picks, respectively (see Figure 19).

When using coordinates from Haase et al. (2013), P-wave velocities of uppermost layers are slightly higher (+7 and +10 m/s for old and new arrival time picks, respectively) and for second and third layers significantly lower. Second layer velocities drop to 1053 and 580 m/s for old and new arrival time picks, respectively, and third layer velocities drop to 2750 and 1825 m/s for old and new arrival times picks from this study, respectively. Regardless of the travel times used, the velocities raised little for uppermost layers but dropped significantly for second and third layers when changing over from old to new coordinates.

The layer thicknesses are reduced clearly when using the new LROC-derived set of coordinates. Additionally, the layer thicknesses of all layers are reduced significantly when using the set of arrival time picks from this study (e.g. layer thickness of uppermost layer is reduced from 310 to 96 m which represents a reduction by approx. 70%).

We confirm a strong increase of seismic velocity with depth. In our new model, upper layers tend to be thinner and have lower velocities, leading to more drastic increase of velocity with depth compared to previous analyses (Cooper et al., 1974).

In general, the residual plots do not show any trends. In particular, the histogram plots of the residuals show a normal-distributed variance, and the residual lag plots show a random pattern, suggesting uncorrelated errors, as is pre-required for our regression model. Furthermore, residuals show less scattering and correlation, attesting to the appropriateness of the model (Appendix, Figures 23-25).

When using new P-wave arrival time readings from this study in combination with LROC-based coordinates, it is clearly visible that layer thicknesses are reduced compared to the velocity depth model published by Cooper et al. (1974) (Figure 14).

All models from this study suggest a more drastic increase of seismic velocity with depth. This becomes more clear when comparing the most left and most right columns in Figure 19, depicting the velocity depth models when using new P-wave arrival times in combination with new LROC-derived coordinates and old arrival time picks of Kovach in combination with old coordinate data from Cooper and Kovach (1975), respectively.

The results from this study may change the view of the structure of the upper lunar crust as depicted in “The Lunar Sourcebook” (Heiken et al., 1991, chapter 4). In their depiction of the upper lunar crust, the top most layer reaches to a depth of only 10 m with sound velocities of lower than 500 m/s, and the layer below with sound velocities between 1000 and 2000 m/s reaches to a depth of ≥2000 m. With models from this study, this depiction can be refined. We show that the use of new LROC-derived coordinates alone can set the boundary between layers of 322 m/s and more than 1000 m/s (see Figure 19, fourth column from the left) to a depth of 310 m. With new arrival time readings from this study this is set to a depth of 96 m as a boundary between layers of 285 m/s and 580 m/s. When using new coordinates and new arrival times readings seismic velocities exceed 1000 m/s not until the boundary to the third layer is reached at a depth of 773 m, where we calculated the velocity to be 1825 m/s. This is possibly implying a higher degree of compaction of the regolith. While one may try to explain these different structures by data from EP1, EP7, and the LM impact or from secondary seismic arrivals (used in the paper by Cooper et al. (1974), but not used here), this study shows that the small differences in

arrival time readings do not affect the observed trends when changing over from old to new coordinates. In contrast, it is our coordinate updates that yield significantly different structural models.

Our two-layer structures show good agreement with previously published models (compare Figure 13). In contrast, for the three layered models, the uppermost layers are thinner, suggesting a more drastic increase in seismic velocity with depth than was previously thought.

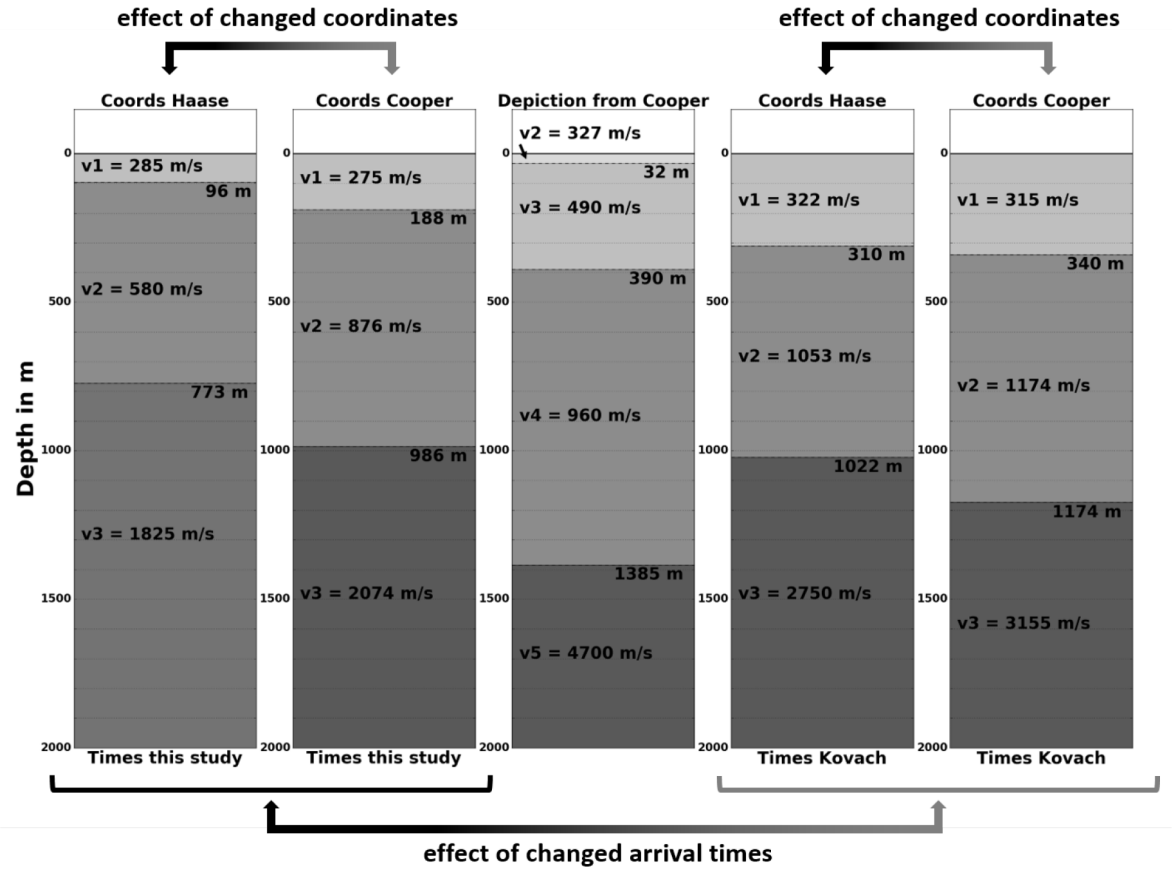

Figure 19: Comparison of depth models for the three-layer case. Chart in the middle represents a depiction of the depth profile published in (Cooper et al., 1974), the uppermost 100 m/slayer with a thickness of 4 m is not depicted here. Left side charts generated with new travel time readings from this study. Right side charts generated with travel time readings from Kovach (pers. communication, 2015). For better readability no error bars are denoted in this plot. Changing over from old to new coordinates results in a thinning of layers. Velocities slightly rise for the uppermost layers. In contrast, p- wave velocities for lower layers decrease significantly.

Acknowledgements

We like to thank the NSSDC for providing access to the original raw data streams and their friendly support. In addition, we like to thank Matthew Brzostowski and Yosio Nakamura for their great support in deciphering the original Apollo data bit stream and associated data.

Furthermore, we like to thank Robert Kovach for sharing his personal notes on the Apollo 17 LSPE. This study is supported by the Helmholtz Alliance "Robotic Exploration of Extreme Environments – ROBEX" (HA- 304).

J. Oberst gratefully acknowledges being hosted by MIIGAiK and supported by the Russian Science Foundation under project 14-22-00197.

3.5 Appendix

Data format

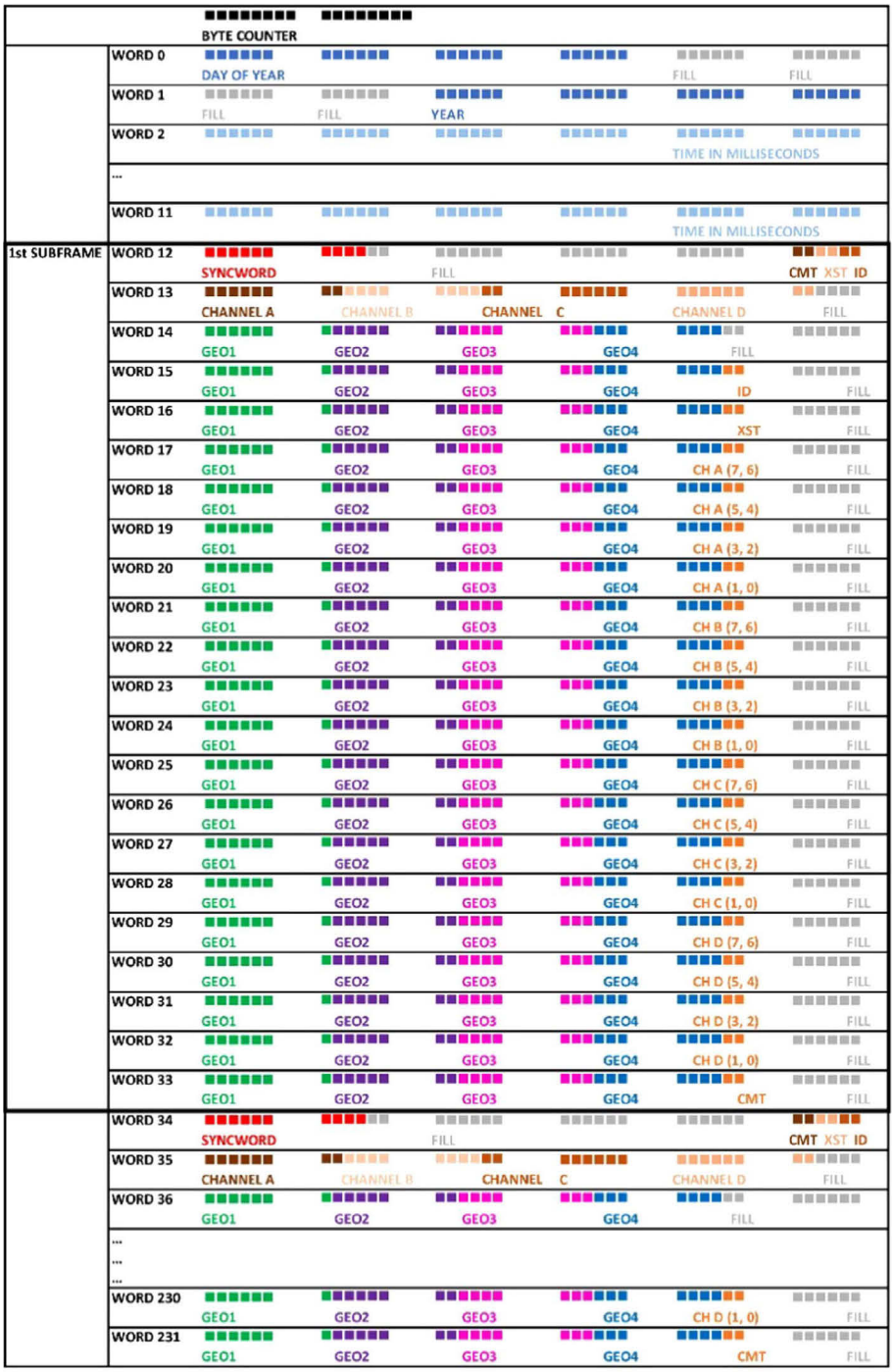

Figure 20: Scheme for deciphering original bit stream. Every box depicts one bit. 1 byte consists of 6 bits. Word 0 and 1 contain binary codes for day of year and year (dark blue boxes with filling zeros in light grey boxes). Words 2–11 contain time readings for the next 10 subframes. Every subframe starts with the synchronous word in red boxes and filling zeros are denoted in light grey boxes. Housekeeping data is depicted in this scheme with boxes in brownish colors. Geophone data is depicted in blocks of 7 bits as follows: geophone 1 in green boxes, geophone 2 in purple boxes, geophone 3 in pink boxes, and geophone 4 in blue boxes.

The Apollo 17 LSPE recorded eight detonations of the explosive packages between December 15th and 18th, 1972. These signals were recorded on the Moon and transmitted as binary sequence to Earth (and handed over to the principal investigators for research). The original Apollo 17 LSPE data set "Seismic Profiling Active Listening Mode" can be ordered at NASA Space Science Data Center (NSSDC) using the ID-code PSPG-00021 (http://nssdc.gsfc.nasa.gov/nmc/datasetDisplay.do?id=PSPG-00021). The provided data comprises the time span from 14-12-1972 to 18-12-1972, thus seismic data of all eight detonations and the impact of the LM decent stage are included. For this work we only used the detonation data.

The original data were stored on 7-track magnetic tape with a density of 800 characters per inch where 1 byte is 6 bits, which is in contrast to today's standards. Later, the data were restored and copied to 9-track magnetic tapes (6250 characters per inch) where 1 byte is 8 bits. To preserve the character nature of the data set, the 6 bits of each original character were put into the first 6 bits of an 8-bit byte and the next two bits of the 8-bit byte were filled with zeroes. This did not preserve the original bit stream. In addition, during restoration process a 2-byte counter was added every 1392 bytes indicating that 1392 bytes will follow in the next physical record. In order to recover the original bit stream it is necessary to remove the padded zeros and counting bytes.

The remaining data is written in non-fortran, binary buffered format with 36-bits per word, 232 words and ten subframes per record. Word 0 contains the day of year decoded in the first four bytes and two bytes filled with zeroes. Word 1 contains two bytes of zeroes and the year in the last four bytes. Words 2–11 contain ten time strings for the following ten subframes, where the time is decoded as milliseconds of the day (straight binary up to 236 milliseconds).

The first word of a subframe (e.g. word 12 in Figure 20) contains the 10-bits synchronous word "00001110111", 20 bits with filling zeroes, two bits of original subframe information, two bits for transmitter information, and two bits for geophone housekeeping data. The second word of a subframe (e.g. word 13 in Figure 20) contains the unpatched channel information, which is displayed in bits 29 and 30 in the following 20 words (e.g. word 14–33 in Figure 20) and four bits of filling zeroes. The channel information is still in bits 29 and 30 on each data word. The following 20 words contain the geophone data. In each data word, geophone data is written in 7-bit-blocks, so the first seven bits contain data of geophone 1, followed by 7 bits for geophone 2, 3, and 4. Then, in bits 29 and 30 parts of the channel information from the second word of the subframe can be found (as mentioned before). The last 6 bits of every data word are filled with zeroes. After that, the next subframe begins (Figure 20).

Timing errors

As mentioned before, the signals from the lunar surface were transmitted in real time to Earth. There, they were received by range stations from the NASA Deep Space Network (DSN) which were distributed around the world. At these range stations, the signals were written on magnetic tapes together with a standard time signal. Time stamps on the tapes represented the time when the signal was received on Earth, not the time when the data was received by the lunar instruments. Then the data was written on another tape set for Principal Investigator (PI) use. Sometimes, when problems occurred in reading the standard time signal, the so-called "software clock" generated time stamps for the PI tapes. But

these time stamps were extremely inaccurate and showed errors ranging from a fraction of a second to as much as a minute. Nakamura (2011) proved that the P-wave travel time for the Apollo 17 LM impact which were used to determine the deepest layer were in error, and therefore this layer can be neglected. Thus, the deepest layer of the study by Cooper et al. (1974) with a velocity of 4700 m/s was not considered in our study.

Residual analysis

Two-layer case

See Figures 21 and 22 here.

Three-layer case

See Figures 23–25 and Table 2 and 3 here.

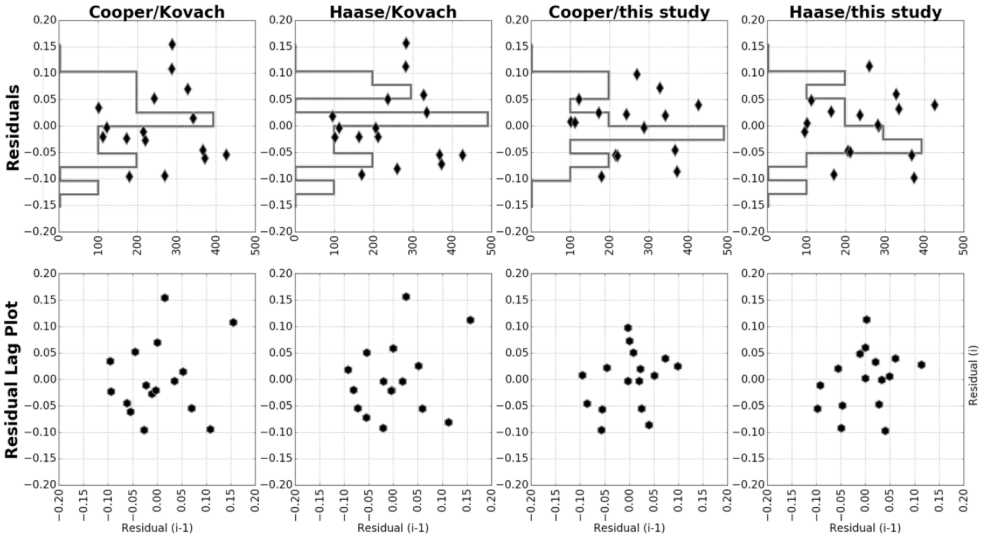

Figure 21: Residuals after model fits for the uppermost layers of two-layer case. Upper panels show residual plots of the four data sets with histogram plots of residuals in the background, lower panels show residual lag plots. Residual plots show a random pattern supporting a sufficiently accurate regression model for determining the slope. The normal distribution in histogram plots supports that. Residual lag plots show no identifiable structure, which means residuals are distributed randomly.

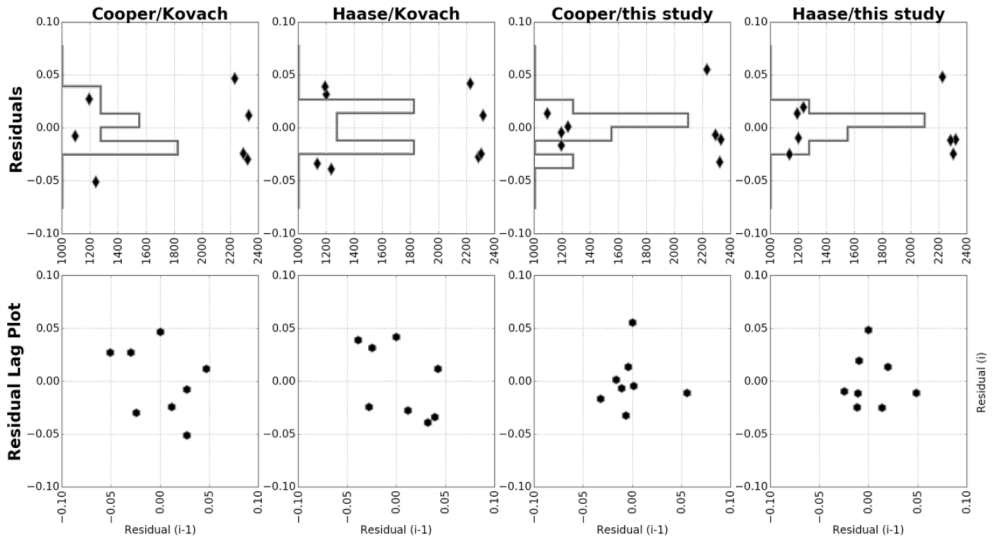

Figure 22: Residuals after model fits for the second layers of two-layer case. Upper panels show residual plots of the four data sets with histogram plots of residuals in the background, lower panels show residual lag plots. Residual plots show a random pattern supporting a sufficiently accurate regression model for determining the slope. The normal distribution in histogram plots supports that. Residual lag plots show no identifiable structure, which means residuals are distributed randomly.

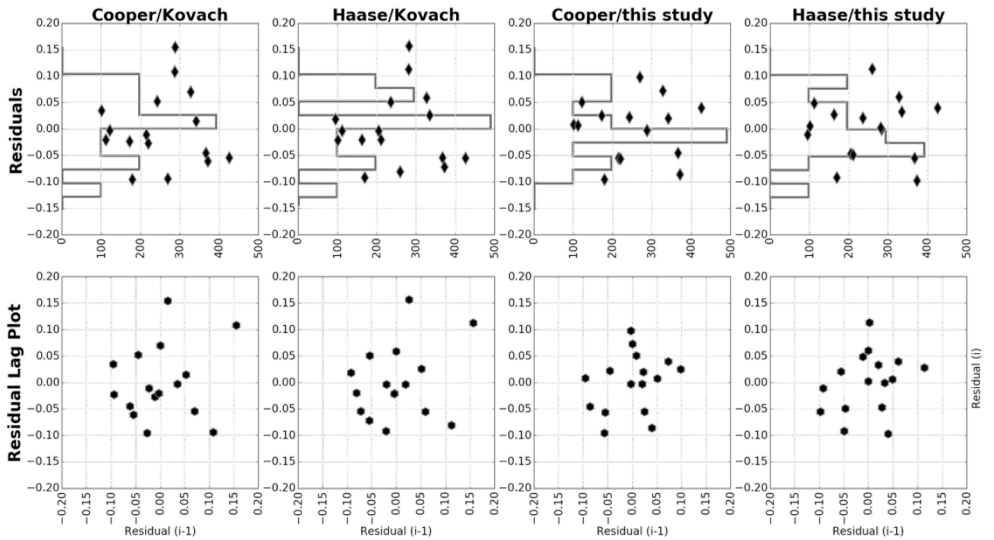

Figure 23: Diagrams for uppermost layers of three-layer case. Upper panels show residual plots of the four data sets with histogram plots of residuals in the background, lower panels show residual lag plots. Residual plots show a random pattern supporting a sufficiently accurate regression model for determining the slope. The normal distribution in histogram plots supports that. Residual lag plots show no identifiable structure, which means residuals are distributed randomly.

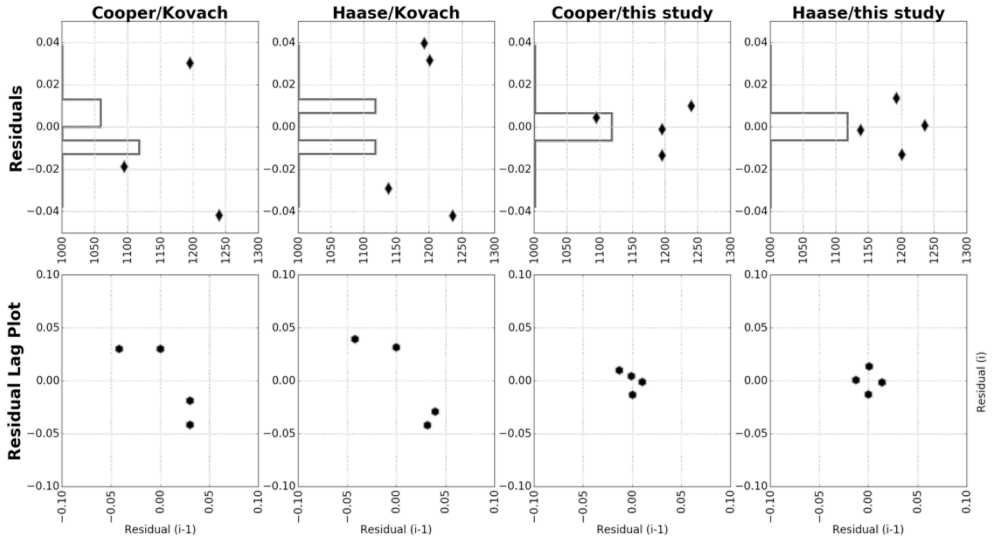

Figure 24: Diagrams for second layers of three-layer case. Upper panels show residual plots of the four data sets with histogram plots of residuals in the background, lower panels show residual lag plots. Residual plots show a random pattern supporting a sufficiently accurate regression model for determining the slope. The normal distribution in histogram plots supports that. Residual lag plots show no identifiable structure, which means residuals are distributed randomly.

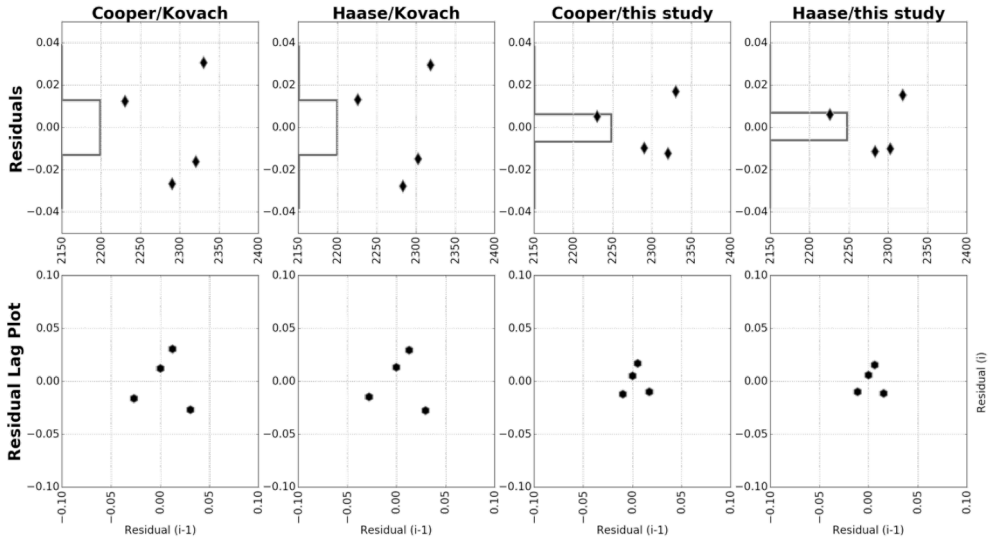

Figure 25: Diagrams for third layers of three-layer case. Upper panels show residual plots of the four data sets with histogram plots of residuals in the background, lower panels show residual lag plots. Residual plots show a random pattern supporting a sufficiently accurate regression model for determining the slope. The normal distribution in histogram plots supports that. Residual lag plots show no identifiable structure, which means residuals are distributed randomly.

Table 2: Detonation Times of Explosive Packages (from Apollo Scientific Experiments Data Handbook, 1974).

Charge No.	Explosive Weight, g (lb)	Date, 1972	Time, G.m.t.
EP6	454 (1)	Dec. 15	23:48:14.56
EP7	227 (1/2)	Dec. 16	02:17:57.11
EP4	57 (1/8)	Dec. 16	19:08:34.67
EP1	2722 (6)	Dec. 17	00:42:36.79
EP8	113 (1/4)	Dec. 17	03:45:46.08
EP5	1361 (3)	Dec. 17	23:16:41.06
EP2	113 (1/4).	Dec 18	00:44:56.82
EP3	57 (1/8)	Dec. 18	03:07:22.28

Overview of point-distances and travel times

See Table 3 here.

Table 3: Overview of point-distances and travel times

Charge No.	Geophone No.	Distance Source-Receiver from (Cooper & Kovach, 1975)	Distance Source-Receiver from (Haase et al., 2013)	P-wave Travel Time from (Kovach, pers. comm., 2015)	P-wave Travel Time from this Study
EP2	G1	327 m	327.4 m	1.19 s	1.2022 s
	G2	425 m	425.6 m	1.38 s	1.5258 s
	G3	371 m	372.9 m	1.20 s	1.2036 s
	G4	366 m	367.2 m	1.20 s	1.2258 s
EP3	G1	242 m	236.3 m	0.90 s	0.8430 s
	G2	341 m	334.9 m	1.18 s	1.2007 s
	G3	288 m	282.9 m	1.15 s	0.9852 s
	G4	287 m	281.0 m	1.10 s	0.9815 s
EP4	G1	269 m	259.5 m	0.84 s	1.0170 s
	G2	172 m	162.4 m	0.60 s	0.5910 s
	G3	215 m	205.4 m	0.75 s	0.6670 s
	G4	220 m	210.9 m	0.75 s	0.6840 s
EP5	G1	2230 m	2225.9 m	3.90 s	4.0270 s
	G2	2330 m	2318.4 m	3.95 s	4.0870 s
	G3	2290 m	2283.2 m	3.88 s	4.0410 s
	G4	2320 m	2302.6 m	3.90 s	4.0530 s
EP6	G1	1195 m	1200.7 m	3.00 s	2.6458 s
	G2	1240 m	1236.1 m	2.96 s	2.7205 s
	G3	1195 m	1192.3 m	3.00 s	2.6580 s
	G4	1095 m	1138.2 m	2.88 s	2.5495 s
EP8	G1	170 m	169.4 m	0.55 s	0.4960 s
	G2	101 m	95.0 m	0.43 s	0.3160 s
	G3	122 m	111.9 m	0.46 s	0.4350 s
	G4	112 m	101.4 m	0.41 s	0.3550 s

3.6 References

Cooper, M.R., Kovach, R.L., (1975), Energy, frequency, and distance of moonquakes at the Apollo 17 site. In: Proceedings of the Conference Paper presented at the Lunar and Planetary Science.

Cooper, M.R., Kovach, R.L., Watkins, J.S., (1974), Lunar near-surface structure. Rev. Geophys. 12 (3), 291–308.

Duennebier, F., Sutton, G.H., (1974), Thermal moonquakes. J. Geophys. Res. 79 (29), 4351–4363.

Haase, I., Gläser, P., Knapmeyer, M., Oberst, J., Robinson, M.S., (2013), Improved Coordinates of the Apollo 17 Seismic Profiling Experiment (LSPE) Components. In: Proceedings of the 44th Lunar and Planetary Science Conference (Paper presented).

Haase, I., Wählisch, M., Gläser, P., Oberst, J., Robinson, M. S., (2019), Coordinates and Maps of Apollo 17 landing site. Earth and Space Science, 6, 59-95.

Heiken, G., Vaniman, D., French, B.M., (1991), Lunar sourcebook: a user's guide to the Moon. CUP Arch.

Kilmer, E.E., (1973), Laboratory, N.O. Final Report for Explosives for Lunar Seismic Profiling Experiment (LSPE). NASA T-558A.

Kovach, R.L., (2015), Person communication.

Nakamura, Y., (2011), Timing problem with the Lunar Module impact data as recorded by the LSPE and corrected near-surface structure at the Apollo 17 landing site. J. Geophys. Res.: Planets, (1991–2012) (116(E12)).

NASA Document, (1972), Apollo Lunar Surface Experiments Package. Apollo 17 ALSEP (ARRAY E) Familiarization Course Handout, NASA-CR-128636, September.

Telford, W.M., Geldart, L.P., Sheriff, R.E., (1990), Applied geophysics 2nd Edition. Cambridge University Press.

Vostreys, R., (1980), Data User's Note: Apollo seismological investigations. NASA STI/Recon (Technical Report N, 81, 17970).

4. Research Paper II

Re-evaluation of Apollo 17 Lunar Seismic Profiling Experiment data including new LROC-derived Coordinates for Explosive Packages 1 and 7, at Taurus-Littrow, Moon

Alexandra Heffels[a], Martin Knapmeyer[a], Jürgen Oberst[a,b], Isabel Haase[c]

a German Aerospace Center - Institute for Planetary Research, Berlin, Germany

b Moscow State University for Geodesy and Cartography (MIIGAiK), 105064 Moscow, Russia

c Technical University Berlin, Berlin, Germany

The final publication is available at Elsevier via

https://doi.org/10.1016/j.pss.2021.105307

Abstract

We re-analyze data from the Apollo 17 Lunar Seismic Profiling Experiment (LSPE) using updated locations of the applied explosive sources. Specifically, we complement our models with the previously missing coordinates and P-wave arrival times of Explosive Packages EP1 and EP7.

We read new P-arrival times for all eight EP events, and solve for two- and three-layer seismic velocity models. We confirm a strong increase of seismic velocity with depth. In particular, we suggest a more drastic increase than was previously thought from post-mission coordinate information. For the three-layer model we find P-wave velocities of 315, 580, and 2680 m/s for the uppermost, second, and third layers respectively, with the transitions between the layers being at depths of 110 and 855 m.

When compared with previous results, we find (1) a slightly higher velocity (+10.5%) for the uppermost layer, (2) no differences in velocity for the second layer, and a (3) significantly higher P-wave velocity for the third layer (+46.9%).

4.1 Introduction

Apollo 17 was the sixth manned lunar landing in 1972, and the most recent. During their eight-day stay on the lunar surface, the astronauts explored the landing site and deployed several scientific experiments for studies of lunar gravity, heat flow and seismicity, amongst others (Apollo 17 Preliminary Science Report, 1973). The Apollo 17 Lunar Seismic Profiling Experiment (LSPE) comprised a Y-shaped array of four identical geophones of the moving coil-type (Vostreys, 1980), and a set of eight explosive packages (EP). The EPs varied in explosive content volume used and the setting of their mechanical securing timers (Appendix, Table 4, p. 53, Table 4**:** Detonation Times of Explosive Packages (from Apollo Scientific Experiments Data Handbook, 1974))**.**

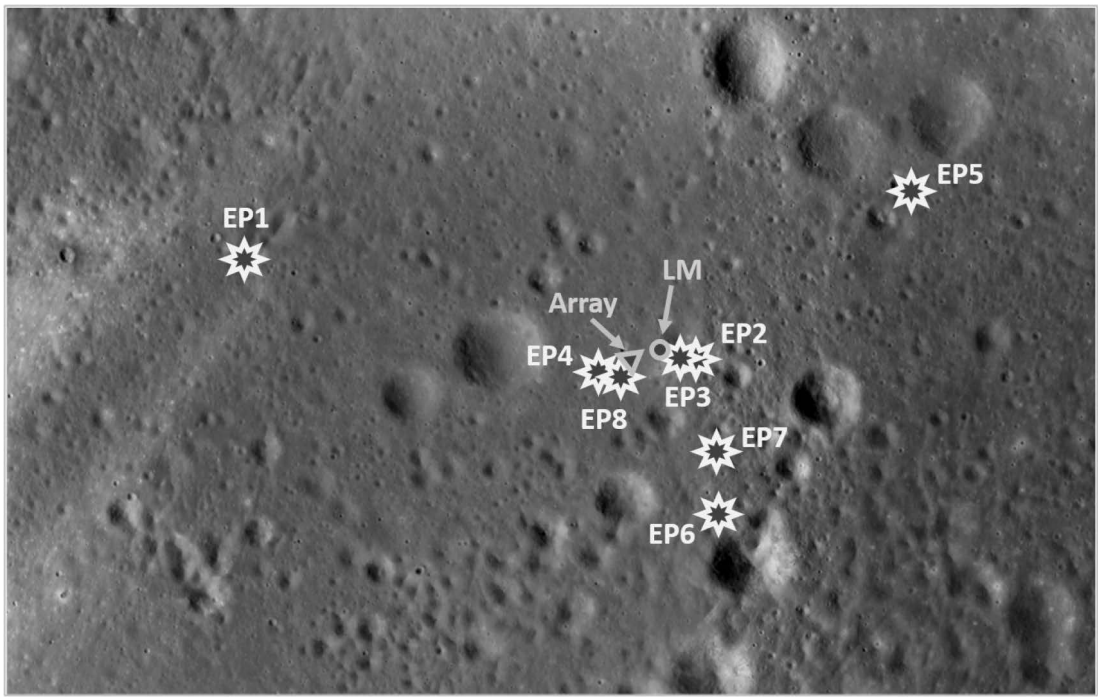

Figure 26: Mosaic of LROC-images of Apollo 17 landing site. Stars mark the location of explosive packages. Position of the geophone array and the landing module (LM) are depicted with triangle and circle.

The explosive packages were deployed at various distances from the sensor array and were detonated remotely per telecommand after the astronauts' departure (Figure 26). The aim of the experiment was to record the seismic waves generated by the eight detonations, as well as the re-impact of the Lunar Module following docking and separation, to study the internal structure of the lunar crust to a depth of several kilometers (Apollo 17 Preliminary Science Report, 1973). Additionally, the Y-shaped array was used to listen and log natural seismic events.

The Lunar Reconnaissance Orbiter was launched in 2009. From an initial near-circular polar orbit, the LRO Narrow Angle Camera (NAC) carried out mapping at a maximum resolution of 25 cm/pixel (standard operation mode 50 cm/pixel) of the surface, including all Apollo landing sites. By combination of the images with Apollo surface panoramas taken by the astronauts, Haase et al. (2013; 2019) carried out a detailed cartographic survey of the Apollo 17 landing site, which included the determination of geometrically accurate coordinates for the geophone positions and the EPs. These derived coordinates of the seismic equipment were found to be significantly different (up to 40 m) from the data previously published in the Apollo Preliminary Science Report (NASA, 1973).

Since Cooper & Kovach (1975) do not describe how distances and coordinates were obtained in the initial preliminary report, the cause of the differences can only be assumed. In all likelihood, these differences were primarily due the quality of the maps (or images) used for position determination during the Apollo deployment period, since these were less accurate than today's LROC-based orthoimage-maps. The observed differences in receiver-source distances, which increased with distance, were likely due to distortions and small scale errors in the Apollo maps, and also the inevitable placement errors resulting from deploying geophones in a rugged terrain and without the aid of surveying equipment, e.g. theodolites.

In our previous study (Heffels et al., 2017), we only considered data from the first publication by Haase et al. (2013), which reported on the coordinates of only six of the eight Explosive Packages deployed by the astronauts. More recently, Haase et al. (2019) published results for the missing EP1 and EP7 packages, which made possible evaluations of the velocity depth profiles which include the complete data collected during the full experiment with the full set of improved deployment positions, which is the topic of this paper.

Including data from EP1 and EP7 added four seismograms (one for each of the four geophones) per detonation to the existing updated EP position corrected dataset, representing an increase in available data volume of one third.

We re-evaluated the full seismic experiment data using the new seismic arrival time readings by considering these newly derived EP1 and EP7 instrument coordinates to update the seismic velocity profiles for the Apollo 17 landing site.

4.2 Method

4.2.1 Cooper model

The five-layer model from Cooper et al. (1974) can be reduced to a three-layer model, as described in our previous study (Heffels et al., 2017). The uppermost thin layer with a low velocity of 100 m/s was adopted from independent thumper data collected by Apollo 14 and 16. Unfortunately, no such supporting data were available for Apollo 17. Furthermore, we determine the inclusion of the deepest layer, with a seismic velocity of 4700 m/s, as questionable, since arrival time readings from only one event – the Apollo 17 LM impact – were used to model this layer. These readings possibly involved errors in the timing (Nakamura, 2011). By excluding the deepest layer of the five-layer model by choice, and the uppermost layer because of data unavailability leaves us with a reduced three-layer model for the Apollo 17 site.

In addition to the three-layer models, simplified two-layer models are also presented in this paper.

4.2.2 Arrival time readings

Lunar seismograms exhibit well-known peculiarities (Cooper and Kovach, 1975; Duennebier and Sutton, 1974), including emergent arrivals and long signal decay times, which impede the reading of arrival times, not to mention the identification of secondary phases. In addition, periodic noise from the transmitter has contaminated all recorded signals (Cooper et al., 1974).

The identification of the first arrival of P-waves is hardly possible from the raw data, therefore digitally processing of the data is required to increase the visibility of P-wave first arrivals. We removed any trends that may appear in the data by subtracting the mean from each individual trace. Cooper et al. (1974) use an error prediction filter for their analyses, but do not specify details on the form of this filter. We opted for a Wiener prediction error filter. A short data sample was used to estimate an autocorrelation function to design the filter. Various filter properties were varied in ways that ensured that the best possible filter results were obtained. Varying the Wiener filter window from 5 to 15 samples for each parameter, as well as changing the noise power from an estimated average to values from 0.5 to 10 for the local variance were useful modifications to the settings of the applied Wiener filter for this regional application (Figure 27). We used the scipy.signal.wiener code from the Python SciPy library for our calculations (SciPy 1.5.0 released 2020-06-21; www.scipy.org).

We carried out travel time inversions by using the new readings (including data from all four geophones and eight EPs) in combination with LROC-based point distances from Haase et al. (2019). For comparison we used the previous arrival times from Kovach (2015, pers. comm., see Appendix, Table 5) and coordinate data from Cooper and Kovach (1975).

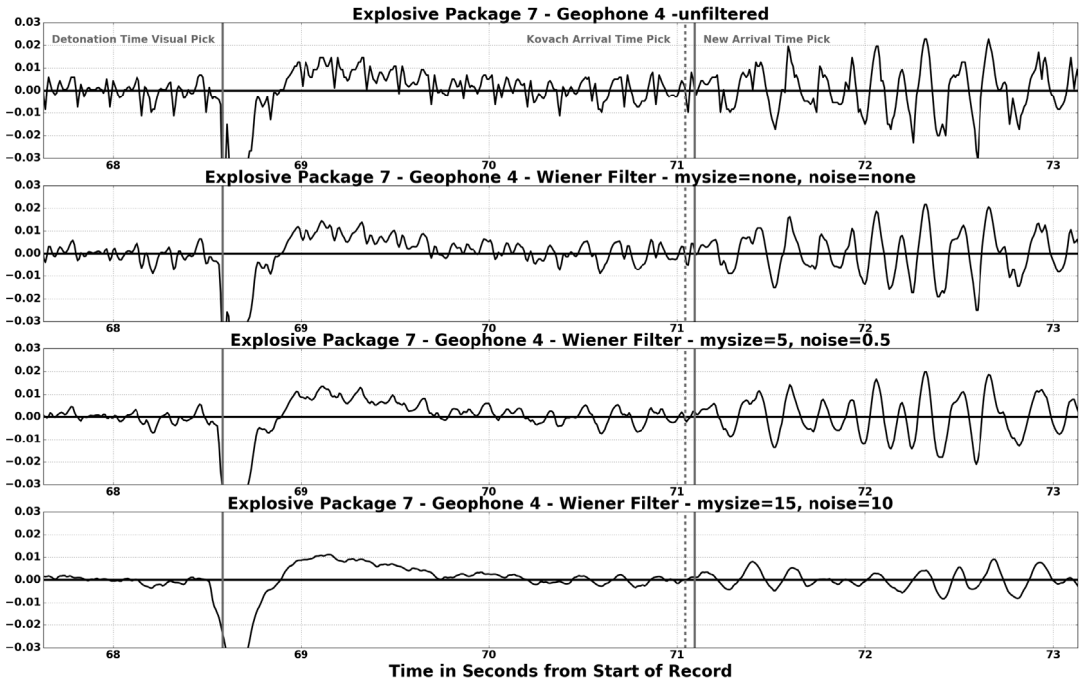

Figure 27: Seismogram plots of EP7 detonation recorded with geophone 4. The uppermost plot shows raw data. The plots below show different Wiener filters applied to find first arrival picks. Since the transmitter was constantly transmitting on the same channel as the seismic data, the electronic detonation impulse remains clearly visible as a strong peak in the data. The bold line marks our visual picks of detonation and seismic wave arrival times. The dashed line marks the arrival time pick from Kovach (pers. communication, 2015).

As in our previous study, combining old and new coordinate data with old and new travel time readings allowed us to obtain four different output combinations: (a) new travel time readings from this study with point distances from Haase et al. (2019), (b) new travel time readings with point distances from

Cooper and Kovach (1975), (c) Kovach's travel time readings with point distances from Haase et al. (2019), and (d) old Kovach's travel times readings with point distances from Cooper and Kovach (1975). We also compared these to the five-layer model of Cooper et al. (1974).

4.2.3 Inversion of arrival times

The velocity-depth profiles were calculated using standard refraction seismic equations (e.g., Telford et al., 1990). A straight line was fitted through the points which belonged to the same layer. Then, the P-wave velocity of a layer was represented by the reciprocal value of the slope.

Intercept times $t_2 = \frac{2h_1 \cos i_{12}}{v_1}$ and $t_3 = \frac{2h_1 \cos i_{13}}{v_1} + \frac{2h_2 \cos i_{23}}{v_2}$ were used to calculate layer thicknesses $h_1$and h_2 (Figure 28).

There are some assumptions underlying the presented travel time inversion, e.g. horizontal layer boundaries and an increase in velocities with depth.

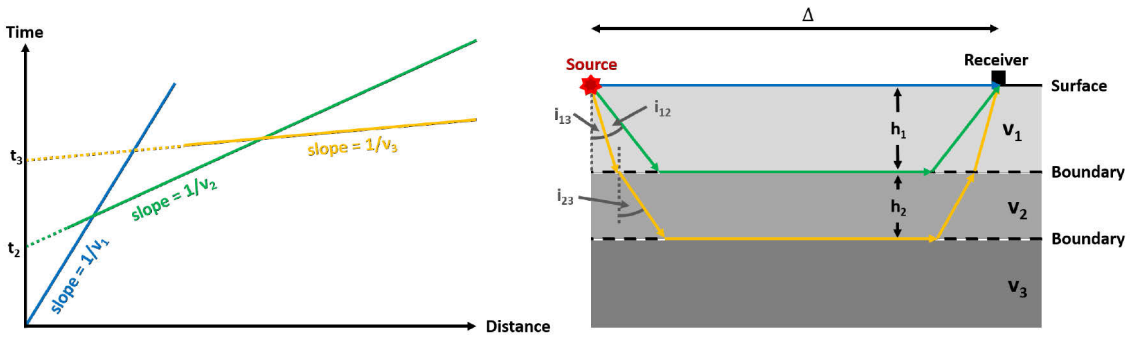

Figure 28: Standard refraction seismic ray paths for a three-layer case. The left figure shows an example of a travel time diagram for a three-layer case. The right figure shows an example of the travel path of seismic head waves in a three-layer case.

Inclined layers are of course conceivable, but non-horizontal layer boundaries cannot be constrained with the available data set. A velocity that decreases with depth would become noticeable as a so-called shadow zone. In order to recognise such gaps in the travel time curve as such, there would have to be a gapless data coverage. However, as already mentioned, the data are unevenly distributed over the entire distance, a shadow zone could occur at any distance where there is currently no data available. Accordingly, it is not possible to prove or disprove the existence of low velocity layers with the present data set.

4.2.4 Analysis of Residuals

In order to check the quality of our analysis, we analyzed the residuals (e.g. lag plot or histograms). Analysis of residuals tests model assumptions of statistical methods with respect to their distribution of the data. This serves to ensure the validity and reliability of the results. A residual is a way to show by how much a best fit regression line vertically misses an actual data point. For a good fitting, linear model shows properties such as (a) residuals which are independent from each other and (b) have a mean of zero. The independence is best shown by evaluating a so-called lag plot, which allows a visual check that the values of the residuals e[i] are independent of e[i+1]. Furthermore, such a check is useful

to determine whether the residuals have a constant variance and are evenly distributed, as these properties also indicate a good model. If the aforementioned properties are not met, the model fails to capture the results optimally and will exhibit bias (cf. Heffels et al., 2017).

4.3 Results

4.3.1 Two-layer case

In this case both layers were complemented with data from one EP, which represented four additional data points (one detonation recorded by four geophones) for each layer. The upper layer is constrained by arrivals of of EP 8, 4, 3, 2, and the new values of EP7, while the arrivals from EP 5, 6, and EP1 constrained the lowermost layer.

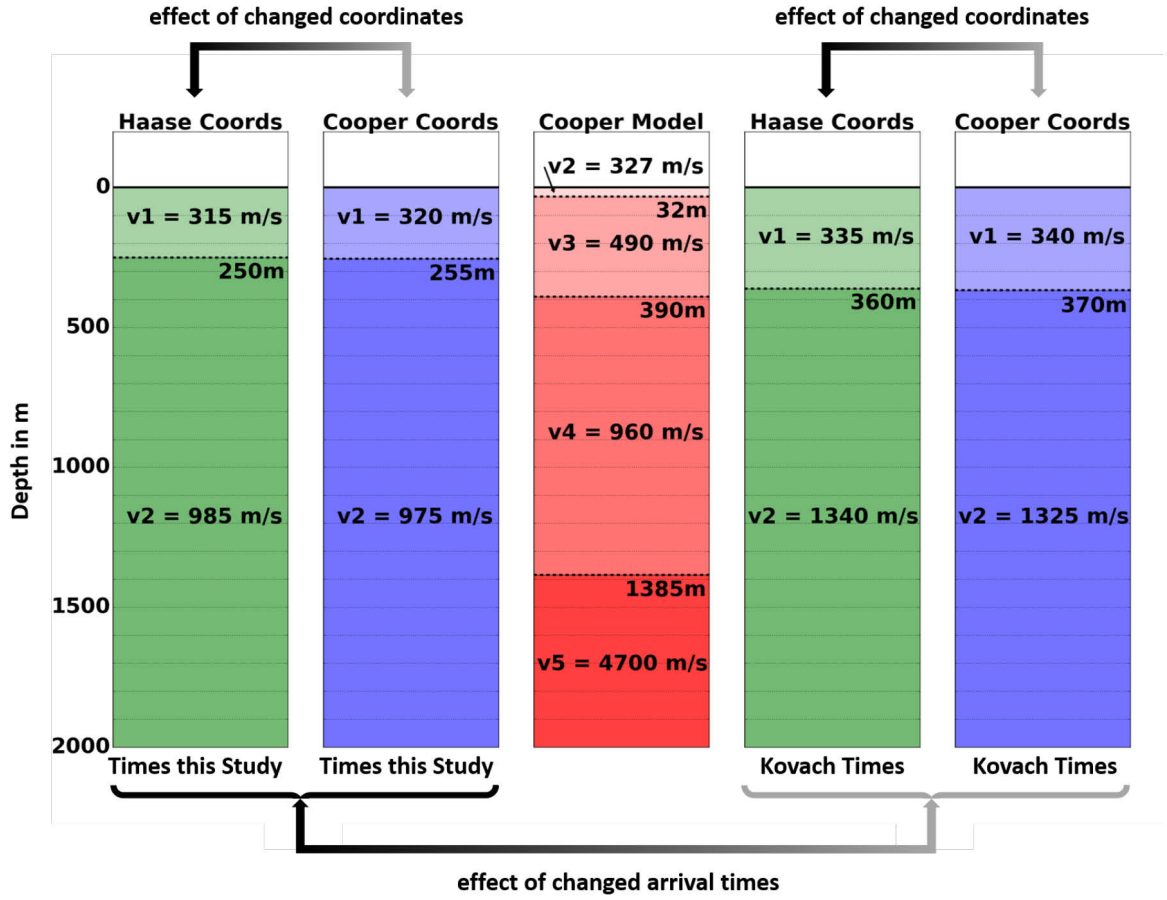

Figure 29: Comparison of depth models for the two-layer case. The column in the middle represents the velocity-depth profile of Cooper et al. (1974); for better readability of the figure the uppermost 100 m/s-layer with a thickness of 4 m is not depicted here. Left hand columns were generated with new travel time readings from this study. Right side columns were generated with travel time readings from Kovach (pers. communication, 2015). In the two-layer case, almost now change in layer thickness is observable when changing over from old to new coordinates. Trends in the velocity changes: velocities slightly drop for the uppermost layer. In contrast, p- wave velocities for the layer below increase.

When using our new arrival time readings and new LROC-based coordinates (Appendix, Table 5), we found velocities of 315 and 985 m/s for the two layers, respectively, with the depth of the layer

boundary at 250 m. Using the earlier travel time readings from Kovach (pers. communication, 2015), we obtain velocities of 335 and 1340 m/s for the first and second layer, respectively, with the transition between the two layers at 360 m.

For comparison we also used the coordinates from Cooper & Kovach (1975) in combination with our new arrival time readings. In this case the velocities of the layers were 320 and 975 m/s for the first and second layer, respectively, and the layer boundary at 255 m. Using the Kovach travel time readings, we obtained velocities for the first and second layer of 340 and 1325 m/s, respectively, and a transition at a depth of 370 m (see Figure 29).

Evaluating the residuals, the histogram of residuals, and the residual lag plot for each of the four cases showed that for both layers the mean value of the residuals was close to zero (appendix, Figure 32 and Figure 33, upper panels). When using our own arrival times, we found that random errors were independent from each other for the first layer (appendix, Figure 32, lower panel), but a certain trend was visible for the second (appendix, Figure 33, lower panel). This residual trend indicates that the chosen two-layer model does not adequately represent the data and may require the extension to a third layer.

4.3.2 Three-layer case

Considering our newly derived P-wave arrival times for EP7, it was evident that this point should be assigned to the uppermost layer. Our P arrival time reading for EP7 fit on a straight line together with the respective times for EP 2, 3, 4, and 8, constraining the top layer (Figure 30 A). In contrast, this allocation was not so clear-cut when considering the Kovach times. With the Kovach times, it is debatable if EP7 arrivals are on the travel time curve from the first or second layer. However, if we assume that arrival time from EP7 together with EP6 form the travel time curve for the second layer, seismic P-wave velocities of more 4200 m/s and 3700 m/s were calculated for the new and old coordinates, respectively. Which means that $v_2 > v_3$, hence the third layer would become a low velocity zone and P arrivals should not exist at all. Since high P-wave velocities, and in addition a low velocity zone below, seem unrealistic for a second layer, this case was not considered further in this paper.

The plot of travel time curves showed distinctive features for the EP7 arrival times. The straight lines of the first and second layer intersect before the arrival of the signals from EP7 (Figure 30). A double check of the data did not reveal any reading errors. The intersection of the straight lines corresponds to the critical distance beyond which the incoming signals represented the head waves of the lower layer. Therefore, the arrival from EP7 should rather be assigned to the second layer, but as described earlier, a straight line representing the second layer and passing through the points of EP6 and EP7 has a higher velocity than the layer below. We conclude therefore that the signals from EP7 are delayed.

Additionally, it should be mentioned that the new LROC-derived coordinates of EP6 and EP7 showed the largest deviations from the historical coordinates (in some instances >40 m, cf. Haase et al., 2019). Furthermore, the signals of these two EPs were the only ones coming from a southern direction (all other EPs were deployed east or west of the array). Geologic research on the Apollo 17 landing site indicates that a particular geologic unit was evident south of the landing module. The Apollo 17 Preliminary Science Report (1975) refers to this unit as the "Central Cluster Ejecta". In this context, this area was characterized by a large number of near-surface blocks that were not completely covered by

younger deposits or haven't been extensively eroded by later impacts. This is due to the young age of this unit. More recent studies on this topic (Iqbal et al., 2019) indicate that the first extra-vehicular activity (EVA-1), which included EP6 and EP7 deployment, was conducted on an area of Copernican age material. This material consisted of loose ejecta and/or material reprocessed by secondary crater clusters. It is therefore likely that much lower seismic velocities can be expected from this region than it is the case for the high density volcanic material of the rest of Taurus Littrow Valley. Being close to the boundary of this material, a lateral variation of thickness appears likely, such that travel times from EP6 and EP7 were affected to differing extents. The standard equations from refraction seismics show that the travel times from EP7 would be affected more strongly than those of EP6, thus the EP7 times were prone to form "outliers" in the travel time plot (Figure 30).

Resolving these structures unambiguously would however require a dedicated experiment with a higher number of source locations and a higher spatial resolution.

In summary, the local geology of the area suggested that there was a locally confined, near-surface layer with extremely low seismic velocities. We have modelled this layer as a pocket underlying EP7.

The models showed that a 20 m thick layer in the path from EP7 with similar low velocities as Surveyor I and III (33-70 m/s, cf. Choate et al., 1969) could explain the observed delays in arrival times of EP7. Layer thicknesses below this value resulted in implausibly low P-wave velocities. A layer thickness of more than 40 m resulted in velocities that were higher than surface velocities of Apollo 14 and 16, which no longer represented a pocket with a significantly lower P-wave velocity as originally envisaged.

In the 3-layer model discussed here, the first layer was therefore determined with the data from EP8, 4, 3, 2 and EP7. The second, underlying layer was, as in the previous work, only determined from the arrival times from EP6. The third, lowest layer was determined with the data from EP5 and EP1 (see Figure 31).

When the new travel time readings were combined with the coordinates by Haase et al. (2019) the P-wave velocities were 315 m/s, 580 m/s, and 2680 m/s for first, second, and third layer, respectively, with transitions between the layers at depths of 110 m and 855 m. In contrast, when the new arrival time readings from this study and the coordinates of Cooper & Kovach (1975) were used in combination, we obtained velocities of 320 m/s, 880 m/s, and 2480 m/s for first, second, and third layer, respectively, and transitions between the layers at depths of 225 m and 1040 m.

For comparison, we calculated the velocities depth models with travel time readings from Kovach (pers. communication, 2015). When combining these with the Haase et al. (2019) coordinates, the P-wave velocities were 335, 1055, and 2125 m/s for first, second, and third layer, respectively. The transitions between the layers were calculated to depths of 320 m and 885 m. When combining Kovach's travel time readings with the coordinates from Cooper & Kovach (1975), these velocities were 340 m/s, 1410 m/s, and 1970 m/s for first, second, and third layer, respectively, with layer boundaries at depths of 370 m and 965 m.

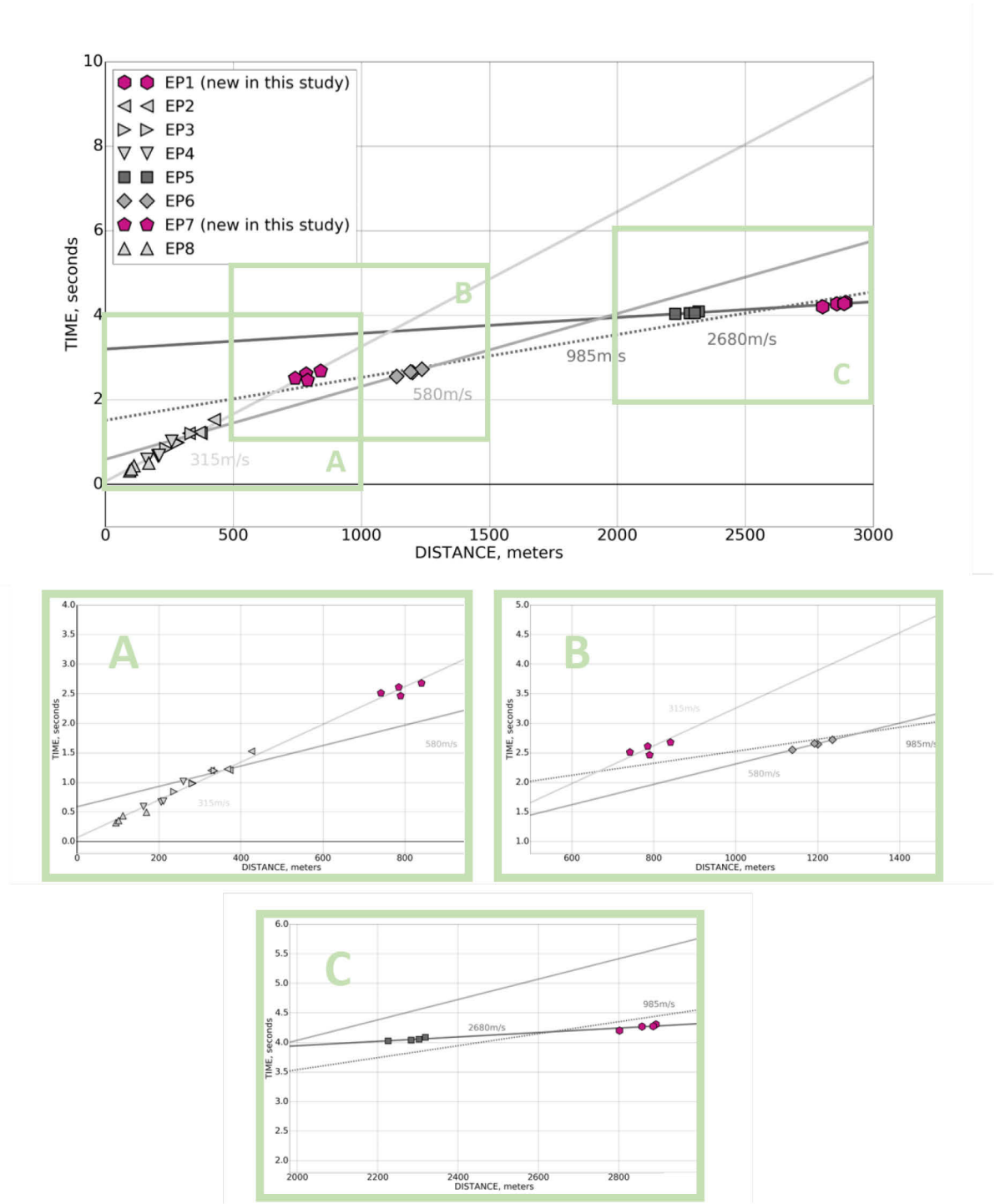

Figure 30: Three-layer case travel time plot for data from this work (LROC-based coordinates and P-wave arrival times from this study). Pink markers show newly included data points. The light grey line represents the best fitting line through data points of EP2, EP3, EP4, EP8 and EP7. The reciprocal slope of this line gives a P-wave velocity of 315 m/s. Best fitting line for the second layer is constrained by EP6 arrivals only and represents a P-wave velocity of 580 m/s. The dark grey line represents the best fitting line through arrival times of EP5 and EP1. The reciprocal slope of this line gives a P-wave velocity of 2680 m/s. For comparison a dashed line is added, depicting the best fitting line for the second layer in the two-layer case (running through EP1, EP5, and EP6). The dashed line represents a P-wave velocity of 985 m/s. Boxes A, B, and C zoom on critical distances.

Evaluation of the residuals, the histogram of residuals, and the residual lag plot for each of the four cases shows that for all three layers the mean value of the residuals was close to zero and that there was no visible trend. Additionally, the random errors were independent from each other as shown in the residual lag plots (appendix, Figures 34-36).

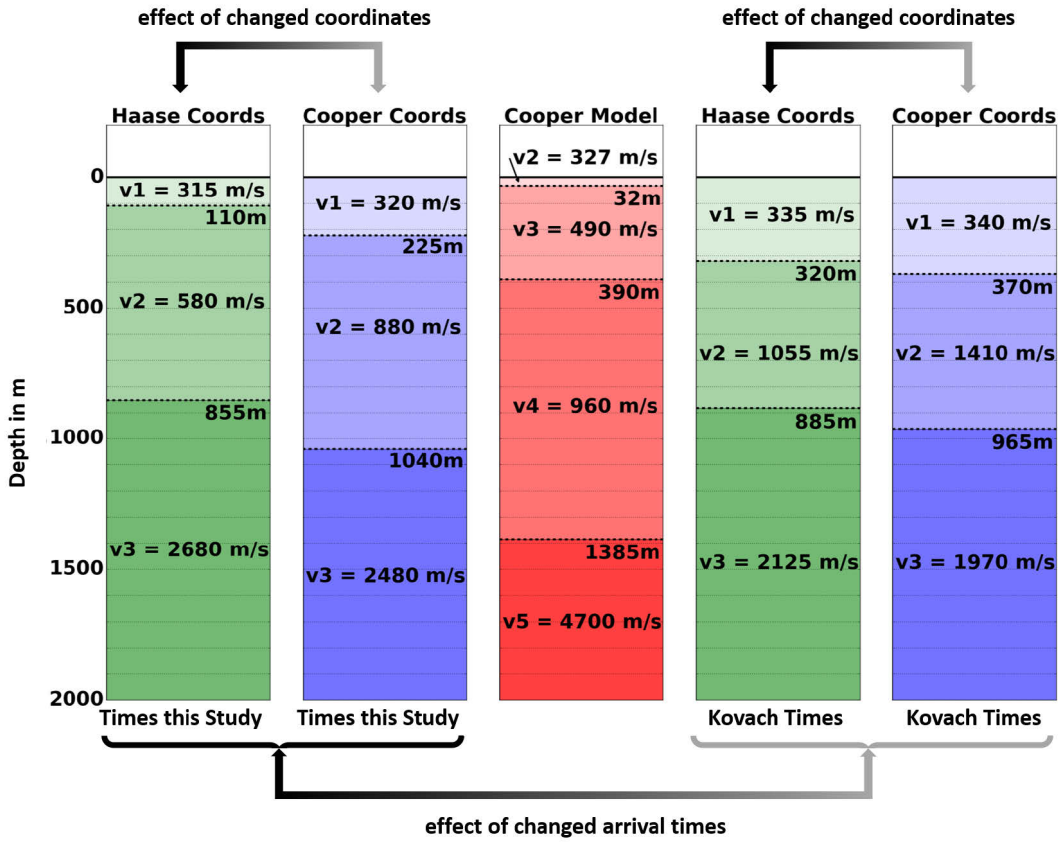

Figure 31: Comparison of depth models for the three-layer case. Chart in the middle represents a depiction of the depth profile published in (Cooper et al., 1974), the uppermost 100 m/s-layer with a thickness of 4 m is not depicted here. Left side charts generated with new travel time readings from this study. Right side charts generated with travel time readings from Kovach (pers. communication, 2015). Changing over from old to new coordinates results in a thinning of layers. Velocities decrease for the uppermost and middle layers. In contrast, P-wave velocities for lowest layers increase significantly.

4.4 Discussion

It is clear in our previous paper that with data from EP7 not available at the time of that study influenced the modeling of the uppermost layer, whereas EP1, at greatest distance from the sensor array, would support the modeling of the deepest layer.

Nakamura (2005) discussed the uncertainty of arrival time picks made on lunar seismograms. This study showed that both in readings of individual seismograms and in stacked versions several different studies determined strongly deviating first arrivals (in some cases even tens of seconds).

It has to be taken into account that Nakamura's study was made for teleseismic events (deep moonquakes), and the scattering of the teleseismic signals cannot be transferred 1:1 to the LSPE.

Nevertheless, these data make it clear that in some cases large uncertainties can be associated with the evaluation of lunar seismograms. Based on our personal estimation of uncertainty, we would assess that the P-wave arrival times determined in this study are well estimated at about 0.01 s.

Owing to uncertainties of the various arrival time readings, absolute values for calculated P-wave velocities and layer thicknesses cannot be readily compared, but trends can be seen.

Model selection

As mentioned before, the dataset we used here has some peculiarities compared to terrestrial datasets. With only 32 data points, the dataset was very small. Furthermore, the points were not uniformly oriented along a profile line, but rather the seismic signals were incident from very different directions and at unevenly distributed distances.

We decided to consider both 2-layer and 3-layer models in this work.

Other, simpler models would be theoretically conceivable. A linear increase in velocity with increasing depth would also be possible. This would have three free parameters: Velocity at the surface, layer thickness, and a velocity gradient. Each additional layer adds another three parameters, such as a possible velocity jump at the layer boundary, layer thickness and the gradient. A possible velocity jump at the layer boundary must be allowed, as there is no geologically plausible reason for two layers of different materials to have the same properties at their contact surface. However, the linear arrangement of the travel times at distances below 500 m shows that a velocity model with a single gradient layer is not a suitable model to represent the data. Thus, a gradient model would only be considered below a cover layer with constant velocity. This type of model would be computationally solvable, but it remains to be clarified whether a non-linear velocity increase might not be an even better way to describe an increase in velocity with depth as the material compacts. Further model variants such as 2-layers-plus-gradient then entail that it must be justified why this model is again preferable to 2-constant-layers or 3-constant-layers. The latter two are already difficult to distinguish, so the introduction of further model classes that are difficult to distinguish from each other does not seem to us to be expedient. Therefore, in this paper we have decided to discuss only constant velocity models in 2- and 3-layer versions.

4.4.1 Two-layer case

Including EP1 and EP7 in the analysis reverses the previously observed trends for P-wave velocities (when changing over from old coordinates to new LROC-derived coordinates, velocities slightly rise for uppermost layers and slightly drop for second layers, c.f. Heffels et al. (2017)). Using the old (and less accurate) Cooper & Kovach (1975) coordinates leads to an overestimation of P-wave velocity of the upper layer, and an underestimation of P-wave velocity of the lower layer. For coordinates by Cooper & Kovach (1975) we calculate the P-wave velocities of uppermost layers to be 340 m/s and 315 m/s for arrival time picks from Kovach (pers. communication, 2015) and from this study, respectively. For second layers the P-wave velocities can be calculated to be 1325 m/s and 975 m/s for old and new arrival time picks, respectively. When using coordinates from Haase et al. (2019), P-wave velocities of uppermost layers are lower (-5 m/s for arrival time pick from Kovach (2015) and -5 m/s for travel times picks from this study) and for second layers higher (+15 m/s for early Kovach arrival time picks and +10 m/s for arrival time picks from this study). The layer thickness remained almost constant when using one set of arrival time picks irrespective of coordinates used (see Figure 26).

4.4.2 Three-layer case

In this case, using the old Cooper & Kovach (1975) coordinates also yielded a slight overestimation and a significant overestimation of P-wave velocities for the upper and middle layer, respectively. In contrast, the velocity of P-waves in the third layer was significantly underestimated. For Cooper's coordinates we calculated the P-wave velocities of uppermost layers to be 340 m/s and 320 m/s for arrival time picks from Kovach (pers. communication, 2015) and from this study, respectively. For second layers the P-wave velocities were calculated to be 1410 m/s and 880 m/s for old and new arrival time picks, respectively, and for third layers the P-wave velocities are 1970 m/s and 2480 m/s for old and new arrival time picks, respectively (see Figure 30).

When using coordinates from Haase et al. (2019), P-wave velocities of uppermost layers were slightly lower (-5 m/s for old and new arrival time picks, respectively) whereas P-wave velocities of second layers dropped significantly to values of 1055 m/s and 580 m/s for old and new arrival time picks, respectively. In contrast, third layer velocities increased significantly to 2125 m/s and 2680 m/s for old and new arrival times picks from this study, respectively. Regardless of the travel times used, the velocities dropped little for uppermost layers whereas these dropped significantly for second and increased significantly for third layers when changing from the old to new coordinates.

The layer thicknesses of uppermost layers were clearly reduced when using the new LROC-derived set of coordinates (e.g. appr. 50% for travel time picks of this study). Changing from old to new coordinates in the model resulted in a reduced layer thickness of the second layer for both Kovach (2015) times and arrival time picks from this study.

Once more, we confirm a strong increase of seismic velocity with depth. The new model conducted in this study, which included data from all 8 EP detonations, indicated that upper layer thicknesses and seismic velocities therein were previously overestimated, while the velocity contrast with lower layers was underestimated.

As in our previous study, the data of the residual plots do not show any trends. In particular, the mean values of residuals were close to zero, and the residual lag plots showed no visible trends, suggesting uncorrelated errors, a prerequisite for our regression model. Furthermore, residuals showed less scattering and correlation, attesting to the appropriateness of the model.

Once more, the two-layer models show a good agreement with the earlier model of Cooper et al. (1974) (see Figure 29, middle column). In contrast, the three-layer models, including data of EP1 and EP7, showed significantly thinner upper layers, and thus indicated a more drastic increase in seismic velocity with depth.

Choice of the proper model

It remains to be discussed which of the models presented is to be preferred. In general, it should be mentioned that the entire Apollo 17 LSPE data set, with its eight detonations, each recorded by four geophones, comprises only 32 seismograms. Thus, the LSPE in its entirety provides only 32 P-wave arrival times. This is a very small data set and, moreover, the points are also not evenly distributed over the distance range of the experiment. In addition, the EPs do not form a classical seismic profile,

but are distributed over a large area (Figure 26). With the principles of refraction seismics, these circumstances lead to an underdetermined inversion problem.

Any meaningful model should use the new LROC-based coordinates of Haase et al. (2019). These coordinates are geometrically accurate and no longer contain estimates, as has been the case for models using the historical positioning data. Therefore, the differences between the models were based solely on the choice of P-waves first arrivals. This means that all results from model variations based on the old coordinates should be neglected. However, these neglected versions can still be used to estimate whether the use of old coordinates leads to an overestimation or underestimation of results.

The remaining models are those calculated with old and new arrival time readings (Figures 29 and 31, green columns). As mentioned earlier, the special characteristics of lunar seismograms (feature-less spectra, emergent arrivals, long signal decay times, transmitter noise) make arrival time reading challenging. For this reason, the determination of travel times for the P-wave first arrivals still involves a certain degree of subjectivity. This subjectivity requires that results are well traceable to the actual arrival times, and particular filter settings, this has not always been the case in the literature. As we discussed in our earlier work, even information on data formats is at risk of being lost. We attempt in this study to provide a better documented and traceable basis for future investigations, until new experiments can be conducted in situ.

The appendix of our first paper on this topic (Heffels et al., 2017) provides instructions for decoding the raw binary data stream. This allows other researchers to decode the binary data and process it with new and appropriate techniques and/or filters to determine afresh new P- wave first arrivals and calculate new (and improved) models. Especially, the application of new filter techniques or automated picking routines which could potentially offer new insights, which have not been considered.

4.5 Conclusions

Complementing the LSPE data set with data from the previously missing detonations of EP1 and EP7 represents an increase in available data volume of one third. Although this represents a decisively large expansion, the LSPE data set remains of manageable size due to experimental design (4 geophones recording 8 detonations). The small number of data points combined with the fact that data points are not evenly distributed over the complete experiment distance also means that evaluations are subject to more uncertainty than it is the case for other (Earth-based) seismic experiments. In the case of the LSPE, small changes in P-wave arrival time picks can, under certain circumstances, lead to larger changes in the calculated models. It can be shown that the use of the new LROC-based coordinates, according to Haase et al. (2019), is a crucial improvement of the database. Furthermore, we can show that the transition from old to new coordinates - independent of the selected set of P-wave arrival times - leads to certain trends in data analysis (see previous chapters). The results of our investigation confirm a more drastic increase in P-wave velocity with depth than was previously thought (Cooper et al., 1975). Therefore, it seems reasonable to suggest that all evaluations of Apollo 17 experiment data that have some position or distance dependence benefit from using the modern LROC-based coordinates.

Closer examination of the distinctive features of EP7 data points in the travel time plot suggests that the lateral variation of LSPE data is larger than previously thought. Previous studies neglected this detail. The data from detonations of EP6 and EP7, the only signals arriving at the monitoring array from a southerly direction, appear to be influenced by the "Central Cluster Ejecta" region, which is characterized by a blocky appearance and lower seismic velocities (Apollo 17 Preliminary Science Report, 1973; Iqbal, 2019). Future research studies on LSPE data should keep in mind that lateral variation in the data is possible if not indeed, probable. While a full analysis of the structures beneath EP6 and EP7 lies outside the scope of this paper, this issue deserves further study. Hence, investigation of different models for subsurface structures including geological context would be beneficial.

Acknowledgements

We like to thank the NSSDC for providing access to the original raw data streams and their friendly support. This study is supported by the Helmholtz Alliance “Robotic Exploration of Extreme Environments – ROBEX” (HA-304).

We would like to thank Wajiha Iqbal, Jörg Knollenberg, Roberto Bugiolacchi, and Harrison Schmitt for their insights and advice.

4.6 Appendix

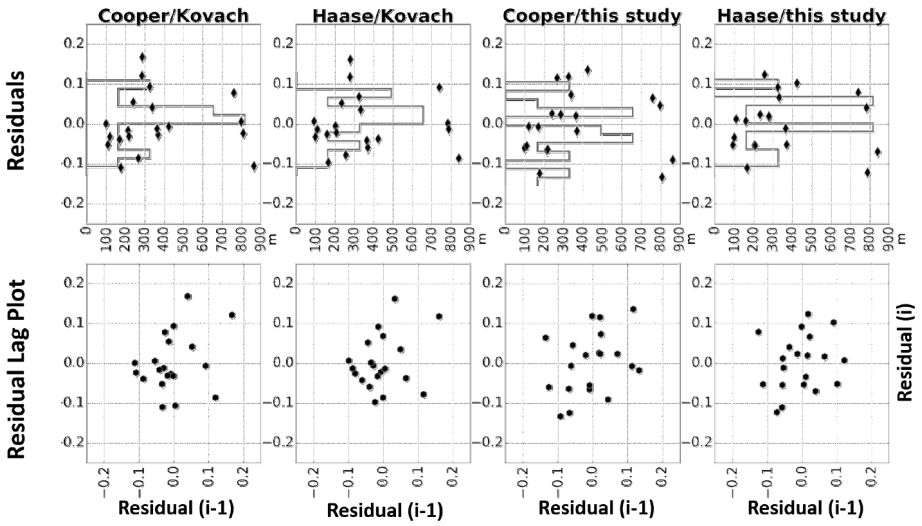

Figure 32: Residuals after model fits for the uppermost layers of two-layer case. Upper panels show residual plots of the four datasets with histogram plots of residuals in the background, lower panels show residual lag plots.

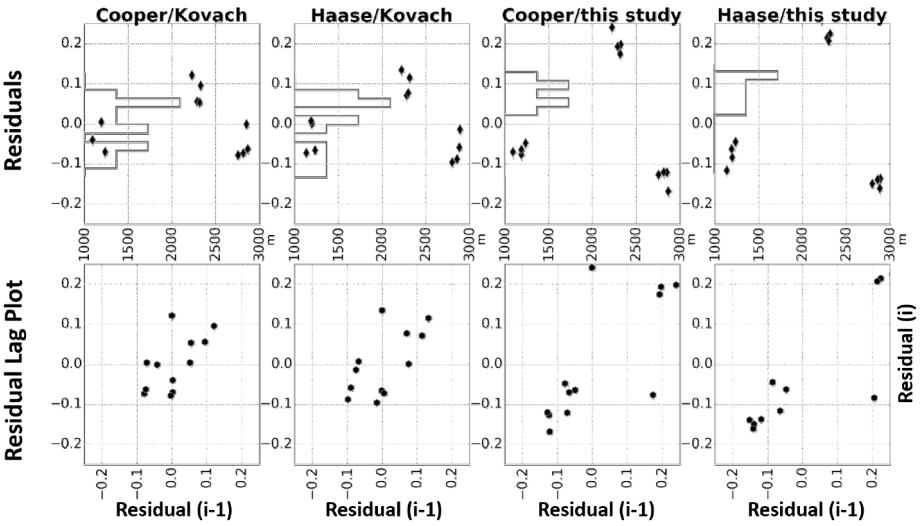

Figure 33: Residuals after model fits for the second layers of two-layer case. Upper panels show residual plots of the four datasets with histogram plots of residuals in the background, lower panels show residual lag plots.

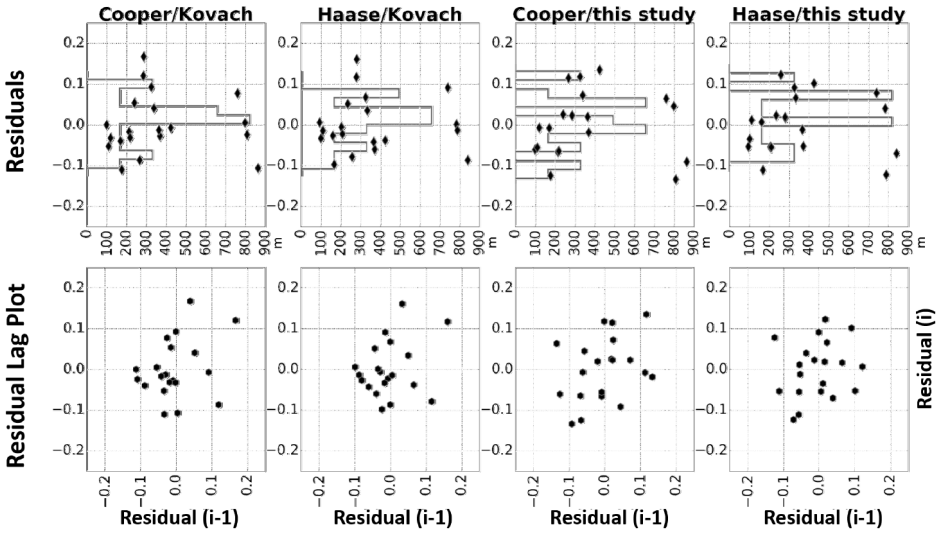

Figure 34: Diagrams for uppermost layers of three-layer case. Upper panels show residual plots of the four datasets with histogram plots of residuals in the background, lower panels show residual lag plots.

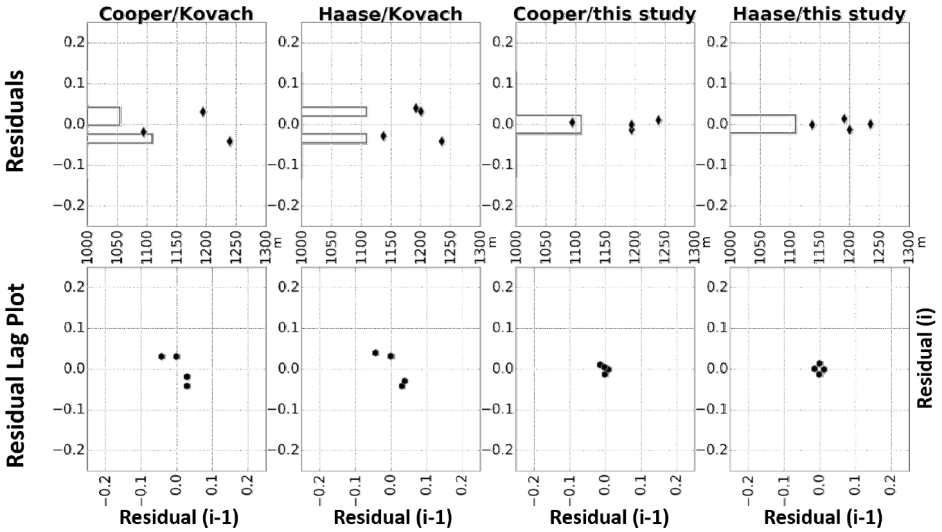

Figure 35: Diagrams for second layers of three-layer case. Upper panels show residual plots of the four datasets with histogram plots of residuals in the background, lower panels show residual lag plots.

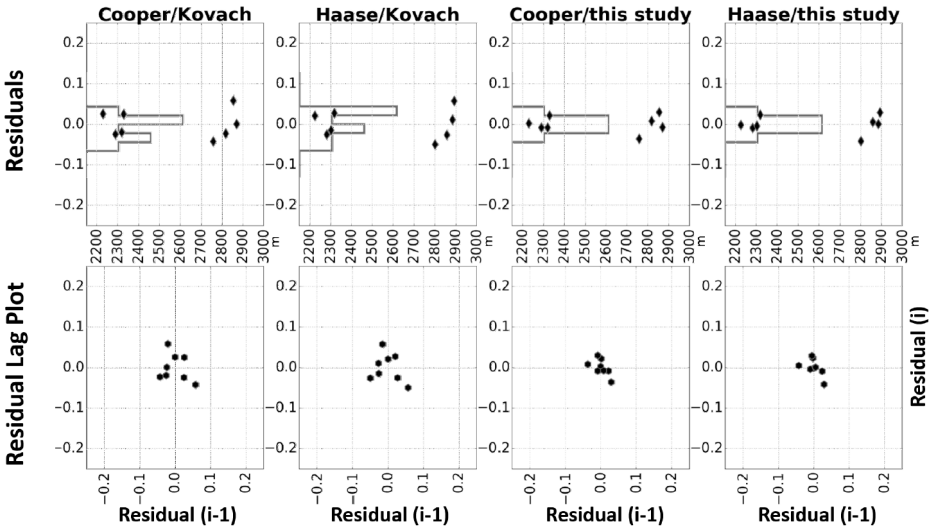

Figure 36: Diagrams for third layers of three-layer case. Upper panels show residual plots of the four datasets with histogram plots of residuals in the background, lower panels show residual lag plots.

Charge No.	Explosive Weight, g (lb)	Date, 1972	Time, G.m.t.
EP6	454 (1)	Dec. 15	23:48:14.56
EP7	227 (1/2)	Dec. 16	02:17:57.11
EP4	57 (1/8)	Dec. 16	19:08:34.67
EP1	2722 (6)	Dec. 17	00:42:36.79
EP8	113 (1/4)	Dec. 17	03:45:46.08
EP5	1361 (3)	Dec. 17	23:16:41.06
EP2	113 (1/4)	Dec. 18	00:44:56.82
EP3	57 (1/8)	Dec. 18	03:07:22.28

Table 4: Detonation Times of Explosive Packages (from Apollo Scientific Experiments Data Handbook, 1974)).

Charge No.	Geophone No.	Distance Source-Receiver from (Cooper & Kovach, 1975)	Distance Source-Receiver from (Haase et al., 2019)	P-wave Travel Time from (Kovach, pers. comm., 2015)	P-wave Travel Time from this Study
EP1	G1	2855 m	2892.4 m	4.25 s*	4.307 s*
	G2	2758 m	2801.5 m	4.10 s*	4.202 s*
	G3	2818 m	2857.7 m	4.15 s*	4.270 s*
	G4	2870 m	2885.5 m	4.20 s*	4.276 s*
EP2	G1	327 m	327.4 m	1.19 s	1.2022 s
	G2	425 m	425.6 m	1.38 s	1.5258 s
	G3	371 m	372.9 m	1.20 s	1.2036 s
	G4	366 m	367.2 m	1.20 s	1.2258 s
EP3	G1	242 m	236.3 m	0.90 s	0.8430 s
	G2	341 m	334.9 m	1.18 s	1.2007 s
	G3	288 m	282.9 m	1.15 s	0.9852 s
	G4	287 m	281.0 m	1.10 s	0.9815 s
EP4	G1	269 m	259.5 m	0.84 s	1.0170 s
	G2	172 m	162.4 m	0.60 s	0.5910 s
	G3	215 m	205.4 m	0.75 s	0.6670 s
	G4	220 m	210.9 m	0.75 s	0.6840 s
EP5	G1	2230 m	2225.9 m	3.90 s	4.0270 s
	G2	2330 m	2318.4 m	3.95 s	4.0870 s
	G3	2290 m	2283.2 m	3.88 s	4.0410 s
	G4	2320 m	2302.6 m	3.90 s	4.0530 s
EP6	G1	1195 m	1200.7 m	3.00 s	2.6458 s
	G2	1240 m	1236.1 m	2.96 s	2.7205 s
	G3	1195 m	1192.3 m	3.00 s	2.6580 s
	G4	1095 m	1138.2 m	2.88 s	2.5495 s
EP7	G1	800 m	785.1 m	2.50 s	2.6106 s
	G2	865 m	840.8 m	2.58 s	2.6778 s
	G3	810 m	789.8 m	2.50 s	2.4630 s
	G4	672 m** (762 m)	741.7 m	2.46 s	2.5103 s
EP8	G1	170 m	169.4 m	0.55 s	0.4960 s
	G2	101 m	95.0 m	0.43 s	0.3160 s
	G3	122 m	111.9 m	0.46 s	0.4350 s
	G4	112 m	101.4 m	0.41 s	0.3550 s

Table 5: Distances and P-wave travel times. *A 0.5 s delay for Camelot crater is already applied to these values. **Haase et al. (2019) noticed a most probable transposition of numbers in the table given by Cooper and Kovach (1975). A distance of 762 m is more plausible and the corrected values are given in brackets.

4.7 References

Choate et al., 1969, Lunar Surface Mechanical Properties, in: Surveyor Program Results, (pp.129-169). NASA SP-184, Washington, D.C.

Cooper et al., 1974. Lunar near-surface structure. Reviews of Geophysics, 12(3), 291-308.

Cooper, M. R., Kovach, R. L., 1975. Energy, frequency, and distance of moonquakes at the Apollo 17 site. Paper presented at the Lunar and Planetary Science Conference Proceedings.

Duennebier, F., Sutton, G.H., 1974. Thermal moonquakes. J. Geophys. Res. 79 (29), 4351-4363.

Haase et al., 2013. Improved Coordinates of the Apollo 17 Seismic Profiling Experiment (LSPE) Components. Paper presented at the 44th Lunar and Planetary Science Conference.

Haase et al., 2019. Coordinates and maps of the Apollo 17 landing site. Earth and Space Science, 6(1), 59-95.

Heffels et al., 2017. Re-evaluation of Apollo 17 lunar seismic profiling experiment data. Planetary and Space Science, 135, 43-54.

Iqbal et al., 2019. New geological maps and crater size-frequency distribution measurements of the Apollo 17 landing site. 50th Lunar and Planetary Science Conference, The Woodlands, TX, USA.

Kovach, R. L., 2015. Person. communication.

Nakamura, Y., 2005. Farside deep moonquakes and deep interior of the Moon. Journal of Geophysical Research, Vol. 110, E01001.

Nakamura, Y., 2011. Timing problem with the Lunar Module impact data as recorded by the LSPE and corrected near-surface structure at the Apollo 17 landing site. Journal of Geophysical Research: Planets (1991–2012), 116(E12).

NASA Editorial Board and Parker, R. A., 1973. Apollo 17 preliminary science report. JSC S-381, NASA SP-330.

NASA Document, 1974. Apollo Scientific Experiments Data Handbook, JSC-09166, NASA TM-58131, August 1974.

Telford, W.M., Geldart, L.P. and Sheriff, R.E., 1990. Applied Geophysics. 2nd Edition, Cambridge University Press, Cambridge, 770.

Vostreys, R. ,1980. Data User's Note: Apollo seismological investigations. NASA STI/Recon Technical Report N, 81, 17970.

5. Research Paper III

Laboratory Tests and System Design for an autonomous Seismic Measurement Station for Application in Remote Field Test Scenarios

Alexandra Heffels[a], Caroline Lange[b], Norbert Tóth[b], Stephan Jahnke[b], Patrick Kleinermann[b]

a German Aerospace Center - Institute for Planetary Research, Berlin, Germany

b German Aerospace Center – Institute of Space Systems, Bremen, Germany

The final publication is available at Elsevier via

https://doi.org/10.1016/j.pss.2022.105489

Abstract

We introduce a reference concept for a small and lightweight instrument carrier system for operation in isolated areas on Earth (or even on other celestial bodies) that autonomously records data after deployment at a site remote from the main station, thus called Remote Unit (RU). In particular, we present here concepts for realizing an autonomously operating seismometer, including support functions provided by encapsulating the actual instrument into the RU carrier. The conceptualization of the RU is based on the design of MASCOT, and intended for evolving into an instrument carrier for lunar exploration. Still in this paper we focus on the functionality needed for realizing the remote and autonomous aspects of the concept. Evolutionary steps needed for the system design to survive on a planetary body are briefly discussed, but not intensively covered in this paper, but elsewhere.

We developed two prototypes of this RU including three seismic sensors each, either fixed, the other one with a built-in self-leveling mechanism. We used standard seismic sensors, which were integrated into a lightweight instrument carrier equipped with all required support structures for remote terrestrial operation, including power, thermal control, and data acquisition (total mass of prototypes not exceeding 3 kg and 10 kg, respectively). We have carried out laboratory tests and evaluated seismic data from these two types of RU to evaluate noise levels, spectral response, and overall performance of the systems. We demonstrate that the systems provide reproducible data at high signal levels, which warrant comfortable scientific interpretation of seismic data from active and passive experiments. Noise level and detected spectral anomalies (due to mechanical structure and associated Eigenfrequencies) are well within expectations.

5.1 Introduction

5.1.1 Previous lunar seismic experiments

There were early attempts to place seismometers on the Moon, but these were not successful, for example the Ranger 3,4,5 missions (1962) or the early Luna E6 landers from 1963 to 1965 prior to Luna 9 (Siddiqi, 2018). But it was not until the Apollo program that seismic experiments were finally successfully set up in a lunar environment.

The Apollo program was the third human space flight program conducted by NASA and accomplished six manned lunar landings (Apollo 11, 12, 14, 15, 16, and 17) between 1969 and 1972. The main purpose of the Apollo program can be described as "landing a man on the Moon and returning him safely to the Earth" (J. F. Kennedy in an address to American Congress on May 25, 1961) However, the scientific goals for the Apollo program were the geological, geophysical, and astrophysical exploration of the Moon. Therefore, all Apollo missions carried a scientific package called Apollo Lunar Surface Experiments Package (ALSEP), which comprised a suite of scientific experiments to measure seismic events, fluxes of charged particles, properties of the lunar exosphere, gravity, magnetic field, and solar wind. The experiments were set up by the astronauts and operated until shutdown in 1977.

One of the experiments carried out on the Moon by Apollo 17 is the Lunar Seismic Profiling Experiment (LSPE), which consisted of eight explosive packages, whose remotely fired detonations were recorded with four single-channel geophones in order to investigate the structure of the uppermost layers of the lunar regolith (Cooper et al., 1974; Cooper and Kovach, 1975; Heffels et al., 2017; Haase et al., 2019).

Apollo missions used geophones of the magnetic-coil type recording the vertical component of ground motion. These geophones were light (complete with outer case approx. 177 g (NASA-CR-147760, 1976)) and designed in a way that an astronaut in a space suit could handle them properly. Hence, they were robust and fail-safe.

5.1.2 Robotic experiment approach

In the frame of the Helmholtz Alliance ROBEX "Robotic Exploration of Extreme Environments" that brought together deep sea and space sciences, we considered how an experiment like the Apollo 17 LSPE could be realized without astronauts and limited resources. This led to the development of a new scenario for a seismic experiment conducted with autonomous robotic devices. A high degree of autonomy is desirable for many reasons. Astronauts on the Moon are highly skilled and extremely expensive professionals who should not waste their working time on activities that can also be done robotically. This includes most aspects of deployment. Moreover, real time remote control during deployment is hardly feasible even for relatively short distances like Earth-Moon. A robotic deployment therefore needs autonomy. Nevertheless, scientists should be able to take over control of certain steps and for final control. The ROBEX scenario comprises a Remote Unit (RU) equipped a threechannel seismometer in solo use (in a first stage) as well as four of them set up in a Y-shaped array (as second stage of the experiment). These RUs can be used for passive listening and for active experiments if used with an active seismic source. Therefore, the ROBEX experiment is divided into two stages. In the first active part a seismic profiling experiment is carried out. An autonomous rover will take one RU to the first point of profile, places it on the ground and levels it. Then the active seismic source is fired and the signals are recorded. Afterwards, the rover picks up the sensor, drives to the next point of profile. This will be repeated for all desired profile points. Afterwards, in the second part, the rover builds up a Y-shaped array (in analogy to Apollo 17 LSPE) for passive listening (cf. Figure 37).

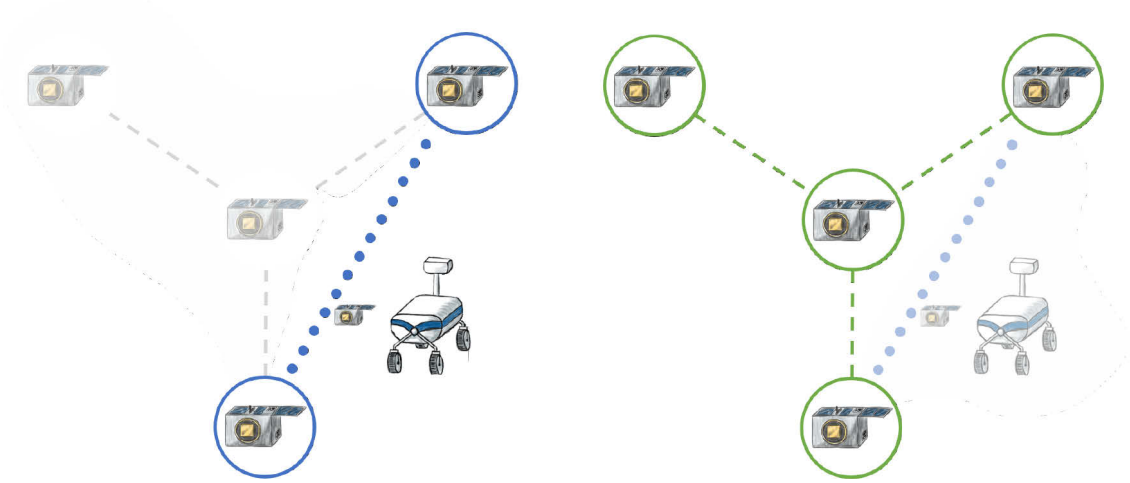

Figure 37: Depiction of the ROBEX scenario. In the active part of the experiment conducted on Mt. Etna, the source was moved along the dotted blue line, with shot points every meter. The rover moves a single Remote Unit from point to point along a profile line, performing measurements at each profile point. Passive part of the experiment highlighted in green. After measuring the active profile, the rover will build up a y-shaped array for passive listening. The active seismic source can be positioned anywhere within a reasonable distance of the array.

For these experiments it is desirable to have robotic systems with a high degree of autonomy. One of the most important reasons to aim for a high degree of autonomy is to enable more meaningful science, because simple movements of the robots do not need to be time-consumingly planned, checked and commanded by scientists on Earth. The described scenario has been demonstrated in an analogue field test on Mount Etna, Italy (Lange et al., 2017). In the frame of ROBEX, the Remote Unit is the actual seismic monitoring station and contains all elements that are required in order to operate the seismometer. In this paper, we want to present our work done in designing, constructing, and integrating the all-in-one solution suggested with the RU. In addition, we verify that the data gathered with a RU is sufficient for modern seismic evaluations by estimating the internal noise levels and investigating resonances of the RU hardware, which might interfere with seismic signals.
Additionally, we want to emphasize that the RUs presented here (RU-3 and RU-10) are only reference models. The state of the RUs described here is therefore not suitable for flight and there are no plans to put the units on the Moon in their current state. For this, many more development steps would have to follow, which could not be undertaken by us in the context of this work. Nevertheless, we present here our results with regard to the registered data quality.

5.2 Instrumentation and Methods

5.2.1 Remote Unit design

5.2.1.1 System overview

The RU developed in the frame of ROBEX is based on the idea of a lightweight instrument carrier as developed for the MASCOT (Mobile Asteroid Surface Scout) mission (Ho et al., 2016). The structural design of MASCOT served as the basis for the RU design. While the MASCOT system has been built for self-deployment onto an asteroid, the RU has been designed to being handled and deployed by robots. It has been designed for a baseline lunar robotic scenario as described above, using a modular approach in combination with a central base station (the lander) (Lange et al., 2017). The RU in its

original lunar design has been subsequently de-scoped to incorporate only functional elements, which are needed for the demonstration in a terrestrial analog field scenario. In addition, in the analog field scenario Earth gravity is affecting robotic handling capabilities, which would not be the case in the reduced (1/6) lunar gravity. Consequently, the RU as designed for the Moon would not have been manageable in the analog test scenario due to excessive forces at the end of the robotic arm and exceeded torque limits inside the motors. developed: the RU-3 (for 3 kg mass limit) and RU-10 respectively, with the former being within robotic handling requirements and the latter offering an opportunity to demonstrate more advanced features such as instrument levelling and long-lifetime of the units.

Despite the fact, that the ROBEX scenario describes a lunar experiment, our earth-based experiments would use GPS time to discipline internal clocks. This approach would of course not be suitable for a lunar application. The GPS signal is used to synchronize data streams in time as needed for the seismic evaluations. For a lunar scenario, other possibilities for time synchronization would have to be developed. We will come back to this in section 3.1.3.2 Time Synchronization below.

The RU-generic design houses the instrument for shelter and provides all essential support functions such as rudimentary thermal control (via foil covering), power, as well as data acquisition, handling and transmission to the Control Center – i.e. the operator and subsequently to the scientist. The central components of the Remote Unit are installed in one of two compartments: the payload compartment (within the ROBEX scenario this is a tri-axial seismometer) and the bus electronics compartment (Figure 38). Differences between the two versions shall be mentioned hereafter wherever they occur.

The following features and components are characteristic for the RUs.

- Structure: ultra-lightweight (<18–26% of total system mass) carbonfiber- reinforced plastic (CFRP) structure frame, enclosed by cover foil
- Power: CubeSat PCDU and battery (10–30 Whrs) and solar panels (RU-10 only)
- Data Handling: on-board computer based on an ARM Cortex microcontroller, a 24 bit analog-digital converter (ADC) for seismometer data acquisition, a Global Positioning System (GPS) module for seismic measurements time synchronization
- Communication: Wireless communication (WLAN) for Telemetry and Telecommand using off-the-shelf transceiver and whip antenna. The telemetry protocol is The Consultative Committee for Space Data Systems (CCSDS) with Packet Utilization Standard (PUS).
- Thermal: only temperature monitoring
- Interfaces: grapple interface and docking interface, inductive charging and data interface for RU-10; visual fiducial reference estimation for robotic perception based on so called APRIL tags (cf. Olsen, 2011)
- Instrument: triaxial Lennartz LE-3Dlite Mark III in both RU types, fixed accommodation in customized housing in RU3 vs. self-leveling cardan suspension in RU10 (Geisler, 2016)
- Sensors: tetrahedral accelerometer configuration for attitude determination (RU-3 only)
- Mechanisms: antenna deployment and solar panel deployment (RU- 10 only)

5.2.1.2 Mechanical design

The Remote Units have been designed with regard to existing experience from similar space-related projects. The baseline design for the Remote Unit's primary structure is the MASCOT (Mobile Asteroid Surface Scout) asteroid lander. While MASCOT's structure has been optimized to withstand the loads during launch into space, the Remote Unit has to basically handle the loads under Earth's gravity and during robotic handling, while being as lightweight as possible to meet the mass limitations given by the robotic capabilities. The design solution is a differential carbon-fiber-reinforced plastic (CFRP) framework with dedicated payload and bus compartment (see Figure 39). The FEA (Finite Element Analysis) shows a minimal natural frequency of 7.5 Hz for the primary structure including main components (Jahnke et al., 2017).

For protection against dust and humidity, the primary structure in both versions is wrapped with ESD foil. Additionally, the RU-10 is equipped with six photovoltaic panels to achieve an extension of its operational lifetime. The panels themselves are made from the same material as the primary structure with the COTS solar cells glued to it. Five of these panels are attached to the primary structure using stand-offs to allow for some clearance for harness and mechanical connections. One panel can be unfolded using spring-loaded hinges to increase the illuminated surface. Around the surface body, targets for robotic perception, so called April Tags, are attached to the structural frame. This 2D bar code style “tag” allows a robust detection of the unit and estimation of its attitude even in rough environments (Olsen, 2011). The same primary structure is used for both Remote Unit versions (RU3 and RU-10) with differences only in accommodation and connection of the seismometer. The fixed seismometers are mounted directly onto the removable cover of the payload section using three countersunk bolts. Thus, this panel is in direct contact with the ground during measurements. The geophones and the front-end electronic are accommodated in a cylindrical aluminum housing designed after the associated Lennartz LE-3D/lite Mark III seismometer (c.f. Figure 38, left) (Jahnke et al., 2017). The fixed installation of the seismometer requires the whole Remote Unit to be aligned with the required accuracy normally applied to the seismometer alone.

This issue is circumvented in the RU-10. The seismometer inside the RU-10 is attached to a gimbal mechanism. This allows the seismometer to align itself to the gravity field. The contact with the ground in uneven environments is realized by means of three extendible legs attached to the seismometer housing. In this case a cover panel is not required and is removed accordingly (c.f. Figure 39), leaving the bottom of the payload compartment open. The geophones and the seismometer front-end electronics are accommodated in a 3D-printed housing made of Alumide.

5.2.2 Seismic data aquisition

5.2.2.1 General features

Within the ROBEX scenario, the RU's main function is the acquisition of seismic data. The core of the RU is the On-Board Computer (OBC), which manages the (entire) system. The OBC receives Commands (TC) from the Command Center (CC) and sends Telemetry (TM) back. Three Texas Instruments ADS1282 ADCs are used to digitize the seismometer's X, Y and Z axis analog signals, which will be directly transferred from OBC to the CC, without any onboard data storage. In the current version of the RU and its OBC the tradeoff between data storage and direct downlink was solved in this way, as any available and suitable memory storage solution was not capable to being fit into the design constraints of the current OBC and RU E-Box. It will be investigated how to implement this in future

versions of the RU. In addition, downlink should normally be permanently available, but robustness analysis has shown that this is not the case under all conditions.

The measurement system is powered from the power distribution unit inside the Remote Unit, which consists of a Clyde Space 3rd generation EPS providing different voltage levels to the onboard components and a lithium polymer battery for energy storage. Solar panels for the RU-10 are customized from off-the-shelf equipment. A Waveshare Neo-6M GPS receiver is used to make the GPS time available as a time reference to enable evaluation and comparison of recorded event data. Figure 40 shows a block diagram of the overall measurement chain. The whole RU electronic stack (OBC, ADC, Power, GPS, and WLAN) is integrated into an Electronic Box (E-Box, see Figure 41).

The analog-to-digital converter ADS1282 provides 32 bits conversion bandwidth, the maximum sample rate is 4 kHz. The features of the ADC fulfilled the following measurement and data acquisition requirements derived from the seismic experiment:

- a sampling frequency of 250 Hz per default, which could also be tunable
- a resolution of 24 bit
- a synchronization between the ADCs of the different channels

For test purposes the sampling rate was increased to more than 500 Hz, however this resulted in problems with the RU wireless communication. The ADC's data bus is connected to the OBC. All three ADCs are synchronized via the SYNC input in order to sample the seismic signals at the same time from the Seismometer's X, Y and Z axis. The Data Ready (DRDY) signal will be pulled low if the OBC is permitted to receive data via the Serial Peripheral Interface (SPI).

Due to production uncertainties, the ADCs' negative voltage reference and offsets of each RU are not always constant, but have to be adapted by setting a positive reference complementary to the offset. This means that the RUs have a different full scale. The ADCs equation accounts for this offset in the voltage reference values, where lsbCh is the bit resolution, refP is the positive voltage reference and refN is the negative voltage reference:

$$sampleValueV = (sampleValueRaw * lsbCh) - offset$$

$$where\ lsbCh = \frac{(refP - refN)/2}{0x7FFFFFFE}$$

The seismic data is received in the Control Center computer, where a Graphical User Interface (GUI) is used for RU commanding, data display, unpacking and storage. A time stamp in human readable format is added to the data in order to compare it with other sensors operated in the same time frame. Time synchronization is done using GPS, which will be discussed more extensively below. For the communication with the Remote Units we used The Consultative Committee for Space Data Systems with Packet Utilization Standard, called CCSDS-PUS. Seismic records are written in CCSDS TM source packets, where one package contains 50 records. Each record consists of a time field (CCSDS Unsegmented Code (CUC), 7 bytes), GPS flag (1 byte, 0x00 – GPS invalid, 0xFF– GPS valid), X axis measurement (raw, 3 bytes), Y axis measurement (raw, 3 bytes) and Z axis measurement (raw, 3 bytes). Table 6 shows one seismic record and Table 7 shows the full Seismic CCSDS TM Source Packet. Typically, the data is unwrapped by the Control Center GUI software and subsequently stored in CSV-Files separately for each RU. In order to reconfigure the seismic measurement it is possible to use specific commands which e.g. change the sample rate or the resolution.

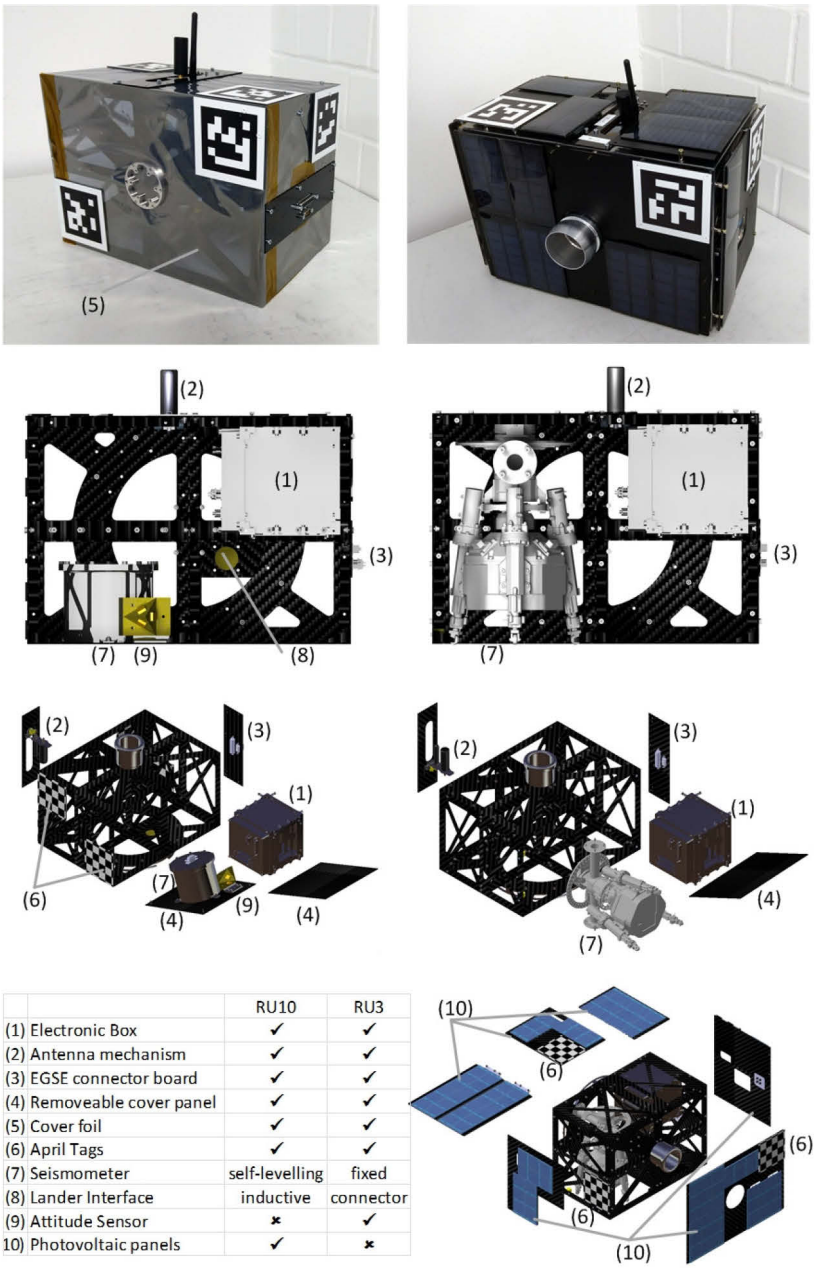

	RU10	RU3
(1) Electronic Box	✓	✓
(2) Antenna mechanism	✓	✓
(3) EGSE connector board	✓	✓
(4) Removeable cover panel	✓	✓
(5) Cover foil	✓	✓
(6) April Tags	✓	✓
(7) Seismometer	self-levelling	fixed
(8) Lander Interface	inductive	connector
(9) Attitude Sensor	✖	✓
10) Photovoltaic panels	✓	✖

Figure 38: Overview and comparison of main components inside the RU3 (left) and RU10 (right) (Jahnke et al., 2017).

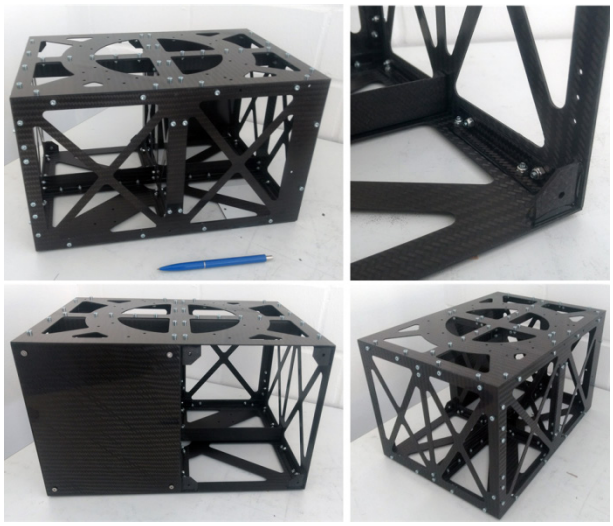

Figure 39: Multi-view of the Remote Unit`s CFRP primary structure [Jahnke et al., 2017]

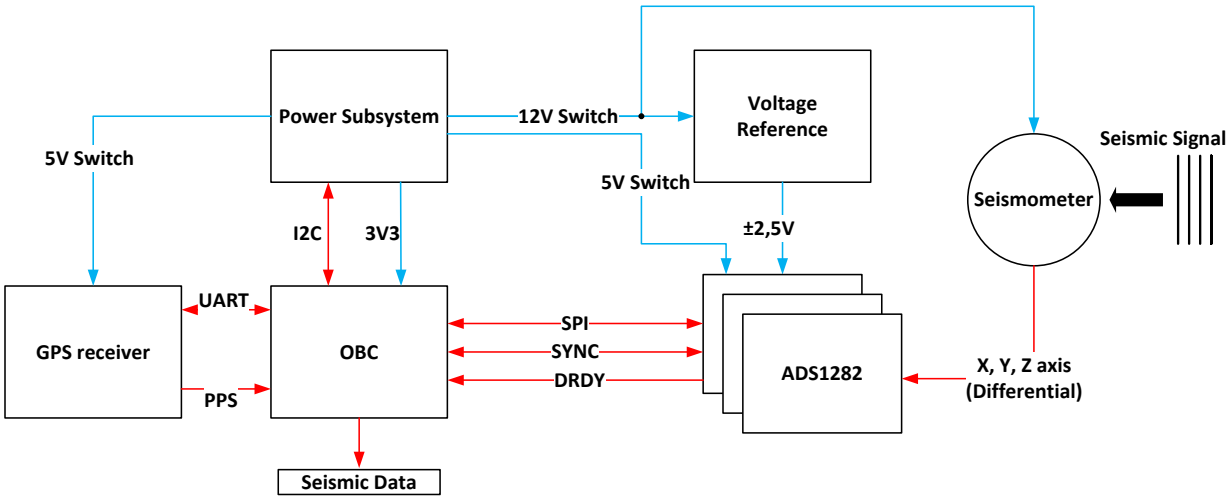

Figure 40: Block diagram of the measurement chain for seismic signal acquisition. Red lines represent data flow direction. Blue lines represent power flow direction.

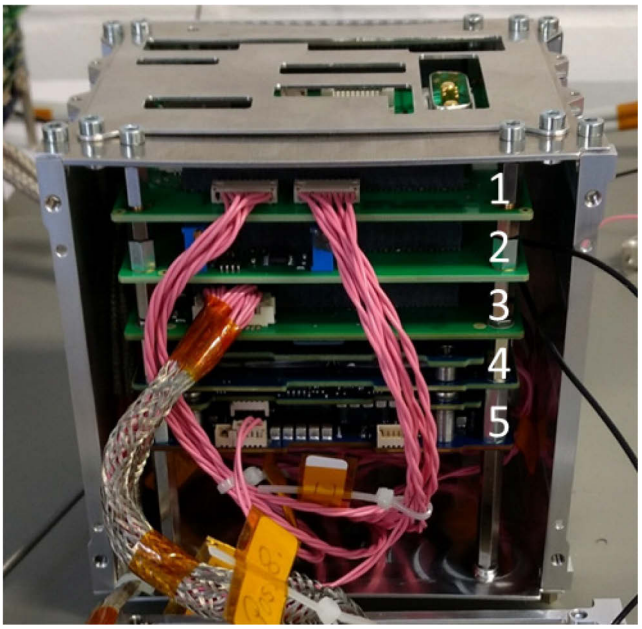

Figure 41: Remote Unit electronics stack integrated into E-Box housing, showing the functional units as depicted in the Block diagram: (1) Interface Board (2) analog-digital converter (3) OBC board with WLAN and GPS module (4) battery board (5) electrical power subsystem (EPS)

CUC time 7 bytes	GPS flag 1 byte	X 3 bytes	Y 3 bytes	Z 3 bytes

Table 6: Data structure of seismic TM

CCSDS TM Source Packet header	Record 1	…	Record 50

Table 7: Seismic CCSDS TM Source Packet

5.2.2.2 Time synchronization

First of all, it should be said that there is currently no GPS available on the Moon. Instead, time synchronization can be enabled via the data link to Earth using appropriate protocols. In fact, this is a common practice, as spacecraft navigation requires clocks that are synchronized with Earth. For example, Knapmeyer et al. (2016) described the clock drift between two experiments on the Rosetta mission.

In order to synchronize events obtained on different channels and in different nodes of a network, time handling and synchronization are of eminent importance. All devices have to run synchronously to warrant accurate measurements of differences in arrival times of seismic waves. While the RU has an internal system time represented in microseconds since OBC activation, it can also be synchronized with the GPS time, thus increasing the accuracy. Either the system time or the internal GPS time representation is used to mark the seismic data with time stamps. To represent a time stamp, the

CCSDS Unsegmented Time Code (CUC) was chosen. CUC, in our configuration, consists of four bytes CUC Coarse Time and three bytes CUC Fine Time. The internal GPS time representation has the same format.

GPS receivers usually provide time data in a quantization of a second. The beginning of every second is indicated by a Pulse-Per-Second (PPS) signal. To deliver timestamps that are in the order of sub seconds, we needed to choose a second time reference which is the clock cycle counter of the on-board computer. The quantization of the on-board computer's clock cycle counter in its configuration is approximately 6 ns. If the RU is synchronized with GPS time, the system time will only be used to calculate the CUC Fine Time and has no influence on the CUC Coarse Time. The incrementing of CUC Coarse Time is triggered by the PPS-signal. If no PPS-signal is available, the system time instead of the internal GPS Time representation will be used as a fall back solution. Due to different clock drift characteristics, this time is not as precise (30 ppm). The PPS-signal loss is detected by waiting approximately 2 s and checking if the CUC Coarse Time was increased. More details of the GPS synchronization are described in (Kleinermann, 2015).

5.2.3 Evaluation of seismic data quality

As the Remote Unit's exact transfer functions are not known, we used three-channel correlation analysis (Sleeman et al., 2006) for evaluation of the instrumental noise. The Sleeman method uses three linear systems recording a common input signal. This is realized by placing three sensors side-by-side assuming that they record the same ground motion. The power spectra of the system noise are expressed in terms of cross-power spectra Pji and autopower spectra Pii of the recordings made with the three digitizers/sensors.

The noise autopower spectrum for digitizer I is given by:

$$N_{ii} = P_{ii} - P_{ij}\,\frac{P_{ik}}{P_{jk}}$$

with $i, j, k = 1, 2, 3$ and $i \neq j \neq k$.

This method is robust compared to the commonly used two-channel approach as self-noise and relative transfer functions can be calculated directly from measurements with no a priori information needed.

5.2.4 Laboratory tests

The tests took place from August 22-25, 2017 in the basement of the DLR Bremen test facility. For our tests, we operated four seismometers, two standard seismometers and two Remote Units, side-by-side (see Figure 42). With this setup we could assure to perform suitable noise level measurements with two Remote Units during only one measurement cycle. We used two standard Lennartz LE3Dlite MkII seismometers each connected to a Nanometrics Centaur-3 datalogger which recorded the data in MiniSEED format (Ahern et al., 2007).

We used two different types of Remote Units, one RU-3 type device (unit name RUG2) and the RU-10 with built-in self-leveling mechanism. Both Remote Units recorded the data on a local computer system in a human-readable ASCII format comprising data for time stamps, raw data and converted (current and velocity) data for all three channels, and some housekeeping information one file comprising approximately 15 min of records. For later evaluation these data files had to be (1) merged together and then (2) converted to MiniSEED format. All measuring devices were placed together at one location (see Figure 42). Unfortunately, both Remote Units are unable to receive a valid GPS signal

inside the DLR test facility, thus preventing acquisition of time information. Therefore, to achieve alignment of the seismic recordings of standard and test equipment we had to preprocess the data. In a first step, we generated a characteristic signal by knocking several times on the facility floor with a rubber mallet. By that we were able to roughly align the seismic recordings by identifying the peaks of our rubber mallet strokes since they were clearly visible and distinguishable from other noise or events in the recordings. In a second step, we calculated the correlation between the two recordings to determine the time shift and correct for it.

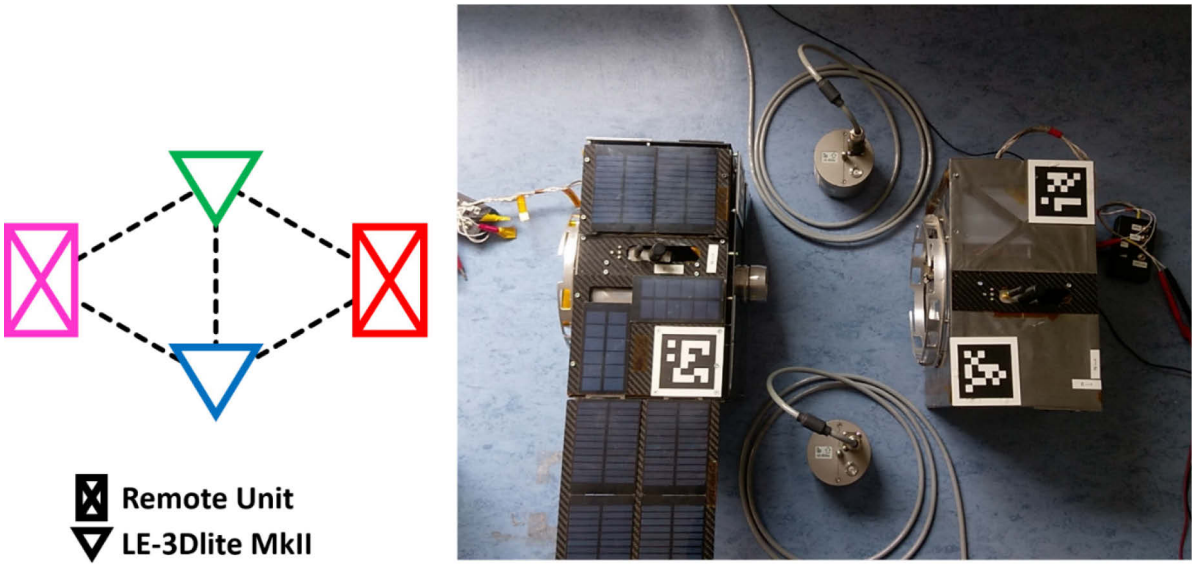

Figure 42: Left: Schematic view of experiment setup. Two standard Lennartz LE-3Dlite sensors and one Remote Unit build a set of three seismometers for evaluation technique used here. Right: Laboratory set-up. Lennartz LE-3Dlite has a diameter of 97 mm.

5.3 Results

5.3.1 Recorded data

We operated the system during night time to avoid environmental noise in the data. All data were recorded at a sampling frequency of 250 Hz. Two data sets were evaluated: (A) recording with the two standard Lennartz seismometers in combination with the RU-10 unit with self leveling mechanism in use and (B) recordings sampled with the two standard Lennartz seismometers in combination with a RU-3 (RUG2) unit.

During the evaluation we recognized problems with data quality of the Remote Unit data due to connection failures during the measurements which led to shortened data streams. For better data

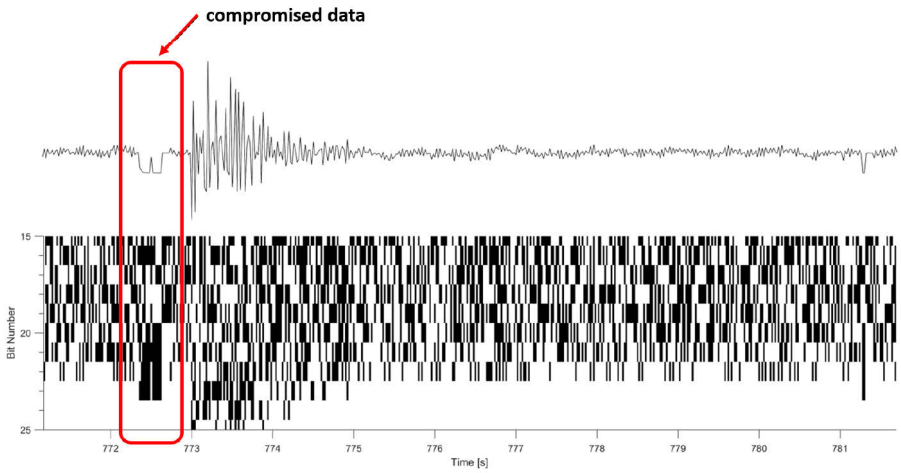

Figure 43: Upper panel shows seismogram with faulty measurement data right before useful signal. Lower panel depicts signal in terms of used bits. It is obvious that bits 18 to 23 are flipped to 1 during the faulty recording. Lower bit numbers do not seem to be affected by that temperature induced fault.

handling these erroneous data parts were padded with zeros before converting the streams into MiniSEED format. Thereby, gaps became clearly visible and suitable time windows for noise level estimation could be identified. This led to a time window of 1 h and a time window of 12 min of continuous, undisturbed recordings for RU-10 and RU-3 data, respectively.

Additionally, it became apparent that the ADC produced faulty measurements during certain times of the experiments (cf. Figure 43). The investigation of this problem showed that the errors are caused by bit flips of the ADC. The ADC is slightly susceptible to high temperatures, which leads to certain

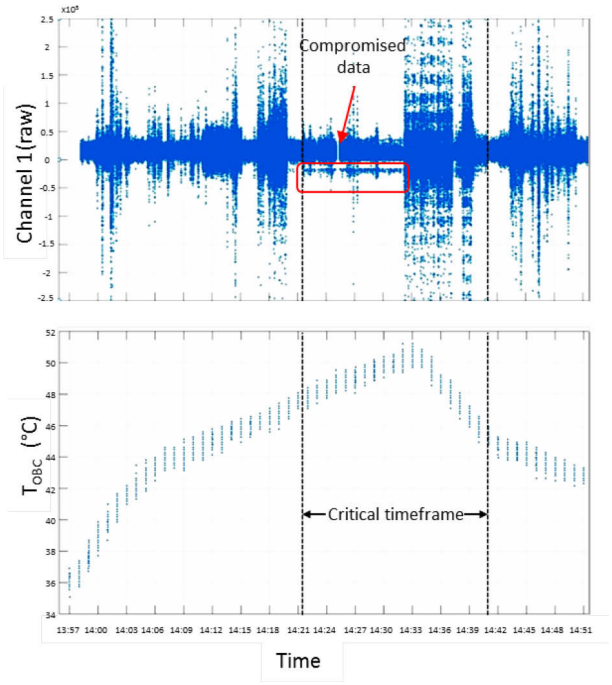

Figure 44: Upper panel shows sample seismic plot with compromised data. Lower panel shows OBC temperature. Since the ADC board has no own temperature sensor but is located directly above the OBC board (see Figure 41) this temperature can be considered as a good approximation.

operating conditions that provide faulty measurement data. Essentially above around 50 C board temperature the ADC produced spikes and offsets in the data attributed to bit flipping (see Figure 43). The behavior is shown in Figure 43, an exemplary seismic data plot (raw data/counts) obtained during an indoor measurement with a RU-3 in a test run of 1:20 h. It is clearly seen, that the issues start around 47 C temperature (the image shows OBC temperature, which is one board above the ADC board in the stack) and vanish, once the temperature drops again (see Figure 44).

5.3.2 Coherence

During a lunar scenario the use of GPS is not possible, but for our earth-based tests in the laboratory for investigation of internal noise levels we decided to use a GPS signal. In this experiment, the GPS signal should only be used to synchronize the data for following noise level analysis. The standard LE-3Dlite devices were connected to Centaur dataloggers which were equipped with long GPS antennas

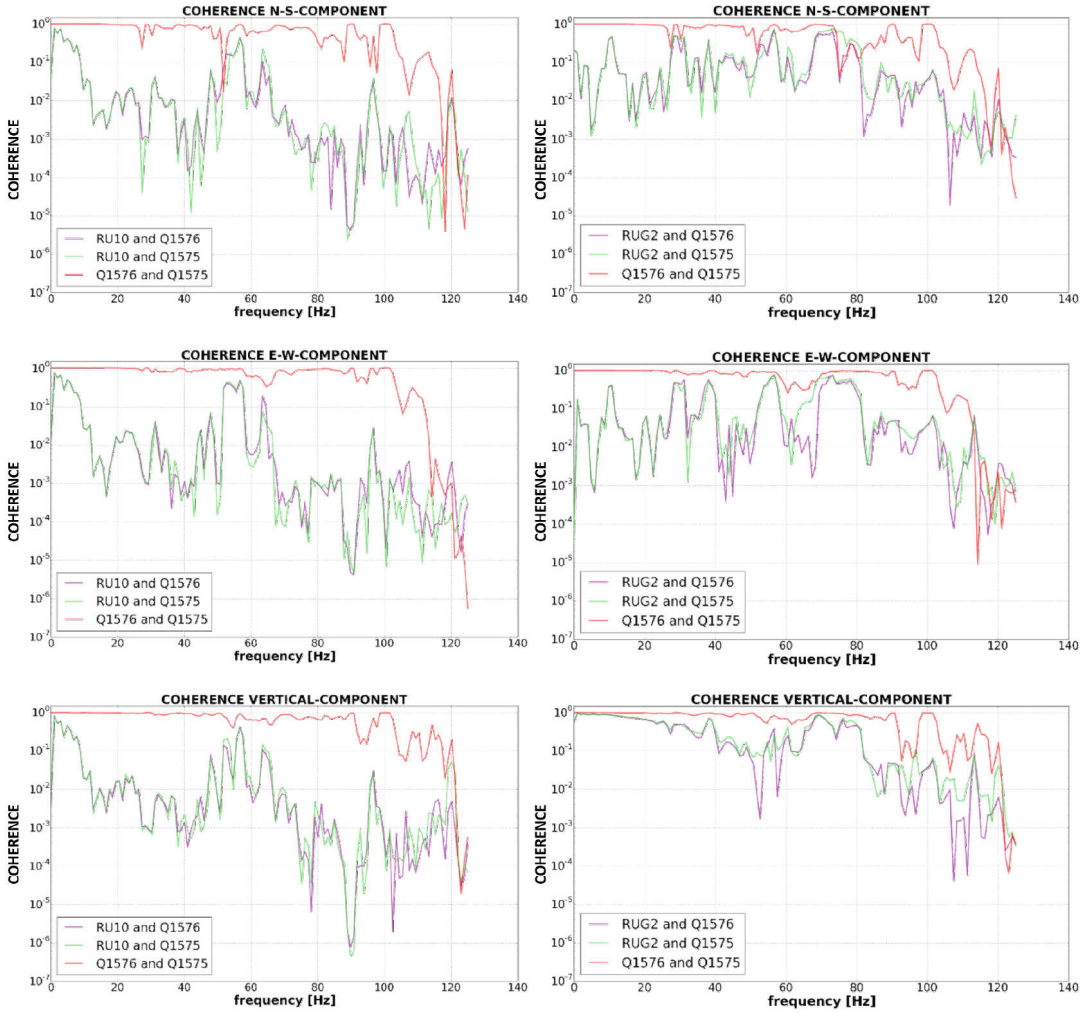

Figure 45: Coherence plots. Standard LE-3Dlite devices marked with Q1575 and Q1576. Left side panels show coherence between RU-10 and LE-3Dlite devices. Right side panels show coherence between RU-3 and LE-3Dlite devices. From top to bottom are shown the north-south (N–S), east-west (E–W), and vertical components of data.

that could be installed in a way that both devices had contact to a valid time signal. In contrast, for both Remote Unit devices it was not possible to establish a GPS connection in our test facility. Therefore, seismic recordings had to be manually aligned in time between standard and RU recordings. Thus, it is beneficial to also evaluate signal coherency plots. Since LE-3Dlite data were recorded with a valid GPS time signal, we can observe a coherence of 0.5 and better between these signals (Figure 45, red lines in all plots) up to frequencies around 90 Hz and a rapid decrease for higher frequencies. Additionally, we observe a good coherence (>0.7) between RU-10 and LE-3Dlite data for very low frequencies (1 Hz).
It is clearly visible that we achieved a slightly better coherency values for RU-3 data.

5.3.3 Noise level estimation

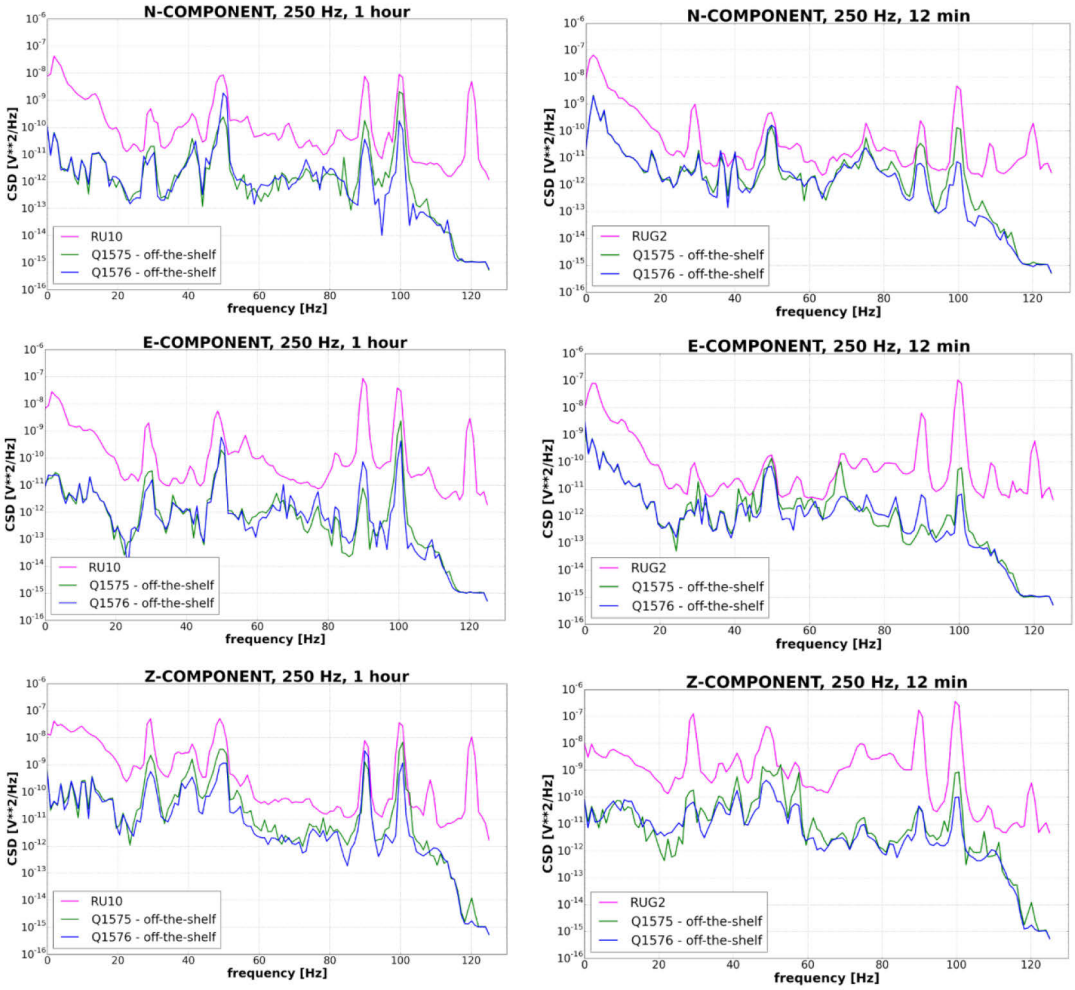

Figure 46: Calculated self-noise recorded at DLR basement by two standard seismometers (Q1575 in green and Q1576 in blue) and the RUs (pink). Left side panels show results for RU-10 type device with self-leveling mechanism in use, measured at a sampling frequency of 250 Hz for 1 h, right side panels show results for RU-3 type device measured at a sampling frequency of 250 Hz for 12min. From top to bottom are shown the north-south (N), east-west (E), and vertical (Z) components. All graphs show clearly elevated self-noise levels for RU data.

Figure 46 shows the calculated self-noise levels for our measurements. All panels show clearly elevated noise levels for both systems (RU-3 and RU-10) and on all channels. We observe several peaks in all plotted lines at the same frequencies: approximately 30 Hz, 40 Hz, 50 Hz, 90 Hz and 100 Hz. The pink lines of RU data also show a strong peak at 120 Hz which is not visible in LE-3Dlite noise levels. Additionally, in RU-3 data a sector of elevated noise level is indicated between 70 Hz and 90 Hz with some smaller peaks at 75 Hz and 80 Hz. This sector is not clearly visible in RU-10 data.

5.4 Discussion

Evaluation of noise level show elevated noise levels for both Remote Unit types. This may be due to the structure around the actual sensors. As described in section 3.1 the RU was designed on the base of the MASCOT, a small and lightweight instrument carrier. The RU houses the sensors and provides support functions like power, thermal control etc. In contrast, a standard Lennartz LE-3Dlite only comprises a solid housing, sensors and a small electronics board. It does not house any supporting systems and has to be powered with an external source. In addition, inside the Remote Units the seismometers are attached to a carbon-fibre bottom plate for RU-3 or to a self-leveling cardan suspension for RU-10, which results in a different ground contact pattern as for the standard seismometers, which are aligned using three solid metal feet. The effects described are of mechanical/structural origin and could, at least to some extent, explain the higher noise levels in RU data.

Since, the peaks at 30 Hz, 40 Hz, 50 Hz, 90 Hz and 100 Hz are visible in all power spectra (LE-3Dlite and RU data) it is evident that these frequencies are characteristic for the self-noise of the measuring systems. The peak at 120 Hz is only visible in RU data which suggests that this is caused by the RU design.

Differences between RU-3 and RU-10 are caused by the different structure and masses. The RU-3 system has a mass of 3 kg and is covered with a thin heat isolating foil, in contrast to the RU-10 system with its leveling device. It has a stronger outside structure due to mounted solar panels and a mass of 10 kg. This has a visible impact on the seismic records and the resultant noise level spectra, e.g., between 75 Hz and 90 Hz we observe elevated noise for RU-3 data (Figure 46, right side panels) but not in RU-10 data.

We had to align data streams in time between the different measuring systems (standard seismometers and Remote Units). A manual and/or calculated alignment in time after the data recording is not a desirable procedure since it could bring in uncertainties. A reliable and robust GPS connection should fix timing problems in future tests. In addition, an onboard time reference (quartz clock) could be installed in the data handling system, thereby achieving independence of an external time reference for a longer amount of time. A stable GPS connection would also be desirable with regard to future earth-related potential applications of the RU.

Another source of uncertainties could be identified in the incomplete Remote Unit CSV-file writing. This was caused by a jammed wireless connection to the operating computer system or by lags on the computer system itself. The gaps had to be padded with zeros for further data handling. This is inefficient and the gaps make it hard to find continuous data streams for evaluation. For RU-3 data, e.g. the longest time window without gaps only measures approximately 12 min. Longer time spans are desirable. In any future tests a major fix concerning data buffering should be implemented to avoid data loss and improve data quality.

Basically, there are various possible causes for the increased noise levels of the Remote Units. Increased self-noise could be due to mechanical/ structural reasons or from electronic components used. Evaluations have already shown that the ADC used tends to bit flipping with rising temperatures and thus generates erroneous measurements. This behavior is unpredictable and can hardly or not at all be corrected. Therefore, exchanging the ADC should be considered.

Nevertheless, it is important to document the bit flipping in the ADC, since such errors also occur in flight hardware. That we quickly recognized the artefacts as bit flips is because these were known from the Apollo seismic data. Knapmeyer-Endrun and Hammer (2015) show that the Apollo seismic data contain bit flips in several bits and that these have to be fixed to avoid timing errors (and to make the data analyzable again). Since in our case it is a temperature-dependent problem and the equipment on the lunar surface would be exposed to extreme temperatures or temperature changes, this type of problem must be known and taken into account early in the development process. Especially when using COTS components, it cannot be assumed that everything works flawlessly in extreme environments. Due to a lack of funding, a further characterization of whether the self-noise originates from the mechanical or electronic parts is not foreseen. Nevertheless, the design of the Remote Unit is promising. There are many useful areas of application for a system for seismic applications that operates fully autonomously in remote areas or even hazardous environments. Additionally, the Remote Units developed and investigated in this work have already proven their field capability in an extensive field study during the ROBEX demo mission 2017 at Mt. Etna (Witte et al., 2020).

5.4.1 Remote Unit design evolution for planetary applications

The presented design of the Remote Unit is focused on sustaining the seismometer operation in a Remote terrestrial environment. For lunar exploration for example, the thermal control concept is of high importance and would thus highly influence the architecture of the RU and its detailed design and consequently in the end the mass and volume. In addition, the communication architecture needs to be adapted to the constraints of the lunar surface communication considering also the provided infrastructure by the carrying lunar lander. Finally, this has to be optimized in terms of power subsystem architecture, considering input energy obtained by solar arrays and storage capacities of batteries. Subsequently, the chosen architecture would have to be designed in detail against the mechanical environment during all phases of such a mission, against the radiation environment and other space environmental aspects. Such investigations have been performed by Witte et al. (Witte et al., 2020) and show the general feasibility of the concept, despite it certainly requiring many more modifications to the structure and the electronics, which would always be accompanied by further changes in the noise levels. During structural and electronic adaptations to a space (or lunar) mission, it would be an essential step to observe and evaluate the effects of changes made to the generated self-noise and, if necessary, to strive for further optimizations.

Concluding, it should be mentioned that earth-based applications e.g., at remote locations are also conceivable. Such a system could be exposed for a longer period of time at a place that is e.g. difficult to access or potentially dangerous for humans. Data could be collected in an internal memory until the system is recovered again, or a regular data downlink could be established. Since the RU is designed as a generic mobile instrument carrier, the implementation of payloads other than the seismometers presented in this paper should be investigated.

Acknowledgements

This work was supported by the Helmholtz Alliance: “Robotic Exploration of Extreme Environments – ROBEX”, grant number HA-304.

We would like to thank Martin Knapmeyer and Jürgen Oberst for their insights and advice.

We thank Autun Purser for help with proofreading and checking the English.

5.5 References

Cooper, M. R., & Kovach, R. L. (1975). Energy, frequency, and distance of moonquakes at the Apollo 17 site. Paper presented at the Lunar and Planetary Science Conference Proceedings.

Cooper, M. R., Kovach, R. L., & Watkins, J. S. (1974). Lunar near-surface structure. Reviews of Geophysics, 12(3), 291-308.

Haase, I., Wählisch, M., Gläser, P., Oberst, J., & Robinson, M. S. (2019). Coordinates and maps of the Apollo 17 landing site. Earth and Space Science, 6(1), 59-95.

Heffels, A., Knapmeyer,M., Oberst, J., Haase, I. (2017). Re-Evaluation of Apollo 17 Lunar Seismic Profiling Experiment Data. Planetary and Space Science, 135 (2017), 43-54.

Sleeman, R., van Wettum, A., & Trampert, J. (2006). Three-Channel Correlation Analysis: A New Technique to Measure Instrumental Noise of Digitizers and Seismic Sensors. Bulletin of the Seismological Society of America, 96(1), 258-271.

Ahern, T., Casey, R., Barnes, D., Benson, R., Knight, T., & Trabant, C. (2007). SEED Reference Manual, version 2.4. IRIS (http://www. iris. edu/software/pqlx/).

Geisler, S. (2016) Development and design of a level-adjustable seismometer carrier for the alignment of the scientific payload in the Remote-unit of the ROBEX-system. University of Applied Sciences Bremen. Available at: http://elib.dlr.de/103711/.

Ho, T.-M. et al. (2016) 'MASCOT---The Mobile Asteroid Surface Scout Onboard the Hayabusa2 Mission', Space Science Reviews. Springer Netherlands, 208(1–4), pp. 1–36. doi: 10.1007/s11214-016-0251-6.

Jahnke, S. S. et al. (2017) 'Mechanical design of a modular experiment carrier for a terrestrial analog demo mission and its potential for future space exploration', in Proceedings of the 68th Astronautical Congress (IAC).

Kleinermann, P. (2015) Zeitsynchrone Erfassung seismischer Sensordaten. Universitaet Bremen. Available at: http://elib.dlr.de/103360/.

Lange, C. et al. (2017) 'A Seismic-Network Mission Proposal as an Example for Modular Robotic Lunar Exploration Missions', Acta Astronautica, 134, 121-132. doi: 10.1016/j.actaastro.2017.02.004.

Lange, C. et al. (2017) 'First Results from the ROBEX Demonstration Mission on Mt. Etna: A modular lunar architecture deployed to perform seismic experiments on a volcano as terrestrial validation of a lunar mission scenario', in Proceedings of the 68th Astronautical Congress (IAC). Adelaide, Australia.

The European Cooperation for Space Standardization (2016) 'ECSS-E-ST-70-41C – Telemetry and telecommand packet utilization'. ESA Publications Division ESTEC, The Netherlands. Available at: http://ecss.nl/standard/ecss-e-st-70-41c-space-engineering-telemetry-and-telecommand-packet-utilization-15-april-2016/.

6. Discussion and Outlook

This chapter discusses the results of the presented research papers and points out additional research opportunities. At the end, a small selection of future planned missions is presented, which have the Moon or its immediate surroundings as target.

6.1 New seismic velocity-depth profiles

With no doubt the Apollo mission data can be described as unique. It not only improved our appreciation of our nearest neighbor, but also broadened our understanding of the formation of our solar system. Especially the Lunar Seismic Profiling Experiment (LSPE) of Apollo 17, which was in the focus of attention in the first two research papers, is still considered the most complex seismic experiment on a celestial body other than Earth itself and thus represents a special resource in both the scientific and technical sense.

The early results of the Apollo 17 mission on the seismic velocity-depth profiles presented by Cooper et al. (1974) showed a five-layer model, which should be treated with caveats today. It should be noted that the top lowest-velocity layer (100 m/s) was not derived from data of the Apollo 17 mission itself. It was assumed that the data generated by the so-called thumper experiment during Apollo 14 and 16 could be used for Apollo 17 landing site as well. Also the existence of the fifth, i.e. lowest, and thus highest-velocity layer (4700 m/s) may be regarded as questionable. Its existence was based solely on the P-wave arrival times of the Apollo 17 Landing Module impact. The work of Nakamura (2011) showed that these data have a timing error, and therefore a separate fifth layer may not be needed to explain the remaining observed data. In total, a three-layer model may be sufficient to describe the subsurface structure of the Apollo 17 landing site, which could be calculated from the historical data of the LSPE and the detonation of the eight Explosive Packages (EP) used during the experiment.

The Lunar Reconnaissance Orbiter (LRO), launched in 2009, provided new high-resolution maps of the lunar surface. It became apparent that the historic coordinates of the LSPE equipment and EPs, and the their respective distances, which are essential for seismic wave travel time estimates, deviated significantly from the LRO-derived coordinates. Research paper I and II showed analyses to what extent the recalculated coordinates and the resulting distances between the devices changed the results for the velocity-depth profiles. The first step was to extract the original bitstream from historical binary data. For this purpose I restored the decryption scheme for these binary data (see Appendix of paper I).

Lunar seismograms were difficult to read due to various anomalies (strong scattering with hardly any attenuation) and were a challenge even for experienced seismologists. In order to make P-wave first arrivals more visible, a Wiener filter was applied to the restored original bitstream. Initially, the evaluation was carried out without EP1 and EP7 (paper I), since no LROC-based coordinates were available for these points at the time of publication. Later, the results were revised again with the data of the missing points (paper II). In both papers, the historical values for P-wave first arrivals (according to Kovach, pers. comm., 2015) and coordinates (according to Cooper and Kovach, 1975) were used on one hand, and the newly determined P-wave first arrivals and LROC-based coordinates (Haase et al., 2013; 2019) on the other hand.

Since the three-layer model corresponded closely to the model of Cooper et al (1974), neglecting the first and last layer for the reasons mentioned above, this model should be considered more closely.

Errors in arrival time readings and implications

An important issue is the discussion of the results in terms of their accuracy. As mentioned previously, the specific characteristics of slowly emerging lunar seismic signals greatly complicates the determination of first arrival times. Thus, it may happen that different seismologists working on the same data set end up at determining completely different first arrivals, far beyond any definition of formal Gaussian errors. These deviations may be in the range of seconds, in some cases even tens of seconds, as was demonstrated for teleseismic events (Nakamura, 2005). It is clear that the differing arrival time readings will result in greatly different velocity-depth profiles. Cooper et al. (1974) writes about the accuracy of his 5-layer model: "All velocities and depths have approximately a 10% error." Whereas the estimated uncertainty for the determined p-wave arrival times in Heffels et al. (2021) is assumed to be 0.01s. Nevertheless, adding error bars varying from 0.01s to 10s and/or 10% would make the plots extremely confusing without producing any actual gain in knowledge. Therefore, in both papers there are no formal error estimates given in any plots.

Instead, a slightly different approach was taken in order to maintain the clarity of the evaluations, especially of the plots. Historical and modern coordinate data as well as historical and modern arrival time picks are presented together with the model of Cooper et al. (1974). Thus, both the change due to differently chosen arrival time picks can be evaluated and the effect due to the use of the improved LROC-based coordinates can be observed.

Under the condition that only the velocity-depth profiles obtained with LROC-based data are considered as the most reasonable evaluation scenario, it becomes clear that the improvement of the position information alone represents a meaningful gain in knowledge. This still leaves the differences between the evaluations of the various arrival time picks. Owing to the great difficulties in identifying arrival times in general, the decision which set of p-wave arrival times is the best to use is left to the reader. One can trust the old data set of Kovach (pers. communication, 2015), where the details on the procedure used for the arrival time picks are lacking. However, one can also trust the p-wave arrival time picks of Heffels et al. (2021), which describe exactly how the data are handled and which filter and filter settings are used for this outcome. However, a third option remains open: in its appendix, paper I provides the reader with detailed instructions for decoding the Apollo 17 LSPE raw binary data. Therefore, it gives every scientist the possibility to use other data processing- or filter techniques to determine his or her own arrival times, and to obtain a feeling for the accuracy of p-wave arrival time picks.

Limitations of layered structures

Besides the estimation of the accuracy, there is also the question of the chosen models. Some approaches can be found on this topic in both papers. In general, a first step in the evaluation of refraction seismic data is, as already described, the calculation of travel-time plots (cf. Fig. 30 or Fig. 66). Here the distances are plotted on the x-axis and the y-axis represents the time that a signal needs to travel from source to receiver. In principle, only points are plotted. The question now arises, how many layers can be represented by these points, or formulated differently: How many lines can be fitted by appropriately chosen point clouds to obtain a suitable velocity-depth model?

In general, Occam's razor is a reasonable choice, which, for the purposes of this work, means that the simplest model is the best. Therefore, 2-layer models represent a reasonable choice, which are presented in both papers. It is noteworthy, however, that Cooper et al. (1974) presented a 5-layer model, even if, for reasons discussed in the papers, the existence of distinct top and bottom layers are only marginally supported by the observations, which therefore can be disregarded. Therefore, the remaining 3-layer models seems to be a useful extension to the 2-layer model in spite of its higher complexity.

As described in paper II (see chapter 4.3.2), attention has to be paid to certain data points, which can be assigned to one or the other layer. For example, a special case arises when the points of EP7 and EP6 are combined and thus form the second layer of the model. In this case, for this second layer the p-wave velocities are 3700 m/s and 4200 m/s for old and new coordinates respectively, which in turn leads to the result that $v_2 > v_3$, and which leaves the third layer a low-velocity layer with no p-wave arrivals at all. Although such unusually large p-wave velocities with a directly following low velocity zone seem unrealistic, this example nevertheless shows that other plausible models have to be considered. Paper II also mentions that the points of EP7 lie in a transition zone (cf. Fig.30). These points show anomalously late arrivals therefore they cannot be assigned to the first layer. However, assigning them to the second layer results in the previously mentioned and rather unrealistic low-velocity layer problem. Therefore, it is suggested here that the arrivals have a delay. In addition, other noticeable features can be observed. Thus, exactly these points show the largest deviations between historical and modern coordinates. Furthermore, only the signals from EP6 and EP7 arrive from southern direction. Together this leads to the conclusion that south of the Apollo 17 landing site a special geological unit, called “Central Cluster Ejecta”, is evident (Apollo 17 Preliminary Science Report, 1973; Iqbal, 2019).

Of course, dipping layers could also offer a reasonable explanation at this point. However, the nature of the Apollo 17 LSPE data does not allow any investigations in this regard. The data include only eight detonations, which were recorded with four geophones each. In total this makes 32 seismic traces. This is a tiny data set compared to terrestrial applications. If you look at the structure of the LSPE (Fig. 10), it also quickly becomes clear that this experiment setup is not a classical profile with evenly spaced receivers along a line. The signals of the detonations come from different cardinal directions. Additionally, there is no counter shot experiment which would allow for identifying dipping layers.

Generally speaking, it can be said that some other possibilities such as low velocity zones and/or dipping layers are always a possibility to explain the observed data, but the limitations of the LSPE setup do not really allow a comprehensive conclusion of the actual structures below the Apollo 17 landing site. Thus, this quickly comes to the ROBEX question "What could be improved in future missions?".

Nevertheless, some general observations can be made. The evaluations showed that the small deviations in time between old and newly determined P-wave arrivals had only a small influence on the structural models. However, the use of the improved coordinates led to significant changes in these models.

The evaluations clearly showed that a transition from old to new coordinates, generally, led to a reduced layer thickness. The P-wave velocities of the uppermost layers decreased slightly, whereas the

P-wave velocities of the layers below increased significantly. For example, the velocity of the bottom layer was calculated to be 2680 m/s when using the LROC-based coordinates and the newly determined first arrivals under consideration of all eight EPs. Using the historical coordinates, this speed was calculated to be 2480 m/s. So, the change of coordinates alone led to an increase of the P-wave velocity for this layer by about 8.1%. This showed that the LROC-based coordinates and the resulting changes in the distances between the equipment had a strong influence on the resulting velocity-depth profiles. Especially considering the thinner layer thickness, this led to a more drastic increase of seismic velocities with depth than assumed by previous studies (Cooper et al., 1975). The newly calculated P-wave velocities of the layers and the depth of the boundaries between these layers thus indicate that the regolith under Apollo 17 landing site must have a significantly higher degree of compaction.

From this work it becomes clear that analysis of the lunar seismograms can be optimized. As already mentioned, the nature of lunar seismograms made it difficult to identify seismic arrivals and hardly possible to determine the arrivals of later phases (Cooper and Kovach, 1975; Duennebier and Sutton, 1974). In addition, the evaluation was further complicated by the fact that the transmitter left a permanent noise on the data channel.

In my work for research paper I (and II), I decided to use a Wiener filter to improve identification of the first arrivals. This prediction error filter used a short data example to filter the data by autocorrelation. Hence, the noise typically generated by the transmitter could be reduced to a level where it was possible to determine the signal onsets. This could be the starting point for further research. Other filtering techniques or approaches might improve the readability of the seismograms and possibly the identification of secondary arrivals. It is in particular the identification of secondary arrivals which could significantly improve our interior structure models.

As the LSPE data set used (eight explosions recorded with four geophones each) was not very large, I determined the first arrivals of P-waves manually, possibly involving biases. In further studies it could be discussed if and to what extent the use of automated picking routines would possibly lead to internally consistent readings and improved model results here.

An improvement of the velocity-depth profiles could further refine our understanding of the composition and structure of the Moon and its evolutionary history.

6.2 Remote Units and their fields of application

The third research paper presented here (paper III) could be divided into two parts. The first part describing the design, construction and its implementation and will not be considered further here. In the second part, I analyzed the quality of the recorded data with respect to its scientific use.

The design developed for MASCOT (Mobile Asteroid Surface sCOuT) served as basis for the developed Remote Units. The aim of this development was to accommodate the measuring instruments used for an experiment including all necessary subsystems (such as thermal control, power, data handling and transmission, etc.) in a small and lightweight instrument carrier. Such an autonomously operating system could then be placed individually or as part of a group at almost any remote location, hence the name Remote Unit (RU).

In general, due to the modular design of the RU it would be possible to accommodate a wide variety of measuring devices or scientific equipment. Within the framework of ROBEX and this work, however,

a scenario was designed following the setup of the Apollo 17 LSPE experiment. Therefore, the RUs were equipped with three-channel seismometers to record seismic data. Two types of remote units were developed. One was the RU-3 was equipped with fixed seismometers. Unfortunately, it was limited to a weight of 3 kg, owing to the fact that the ROBEX rover LRU (Lightweight Roving Unit, Wedler et al., 2015) used during the field campaign could not operate more than 3 kg at Earth's gravity. The other type was the RU-10, which had a self-leveling cardan suspension triaxial seismometer and fold-out solar panels. Only when considering the gravity on Moon, the LRU used during the field campaign could handle the RU-10 as well. Data from both types of RUs have been analyzed with regard to signal quality, in particular, their noise levels. Although the sensors in the RUs consisted of standard Lennartz LE-3Dlite Mark III devices, the evaluations showed that the RUs had increased noise levels compared to standard Lennartz LE-3Dlite Mark II devices, possibly due to specifics of the instrument electronics but also mechanical-structural vibrations.

As various technical problems occurred during data recording for the noise level measurements, electronic causes were very likely. For example, there were repeated interruptions in the radio link from the RUs to the recording computer, which reduced the number of suitable time windows for data evaluation. In addition, the GPS reception of the RUs was disturbed, so that no suitable time stamp was available to synchronize the recorded data. Hence, synchronization had to be achieved both manually and by coherence analysis. Furthermore, the evaluation of the tests showed that the ADC tends to irregular and unpredictable bit flipping at higher temperatures. Although the affected time windows were clearly visible in the seismic data, this error could not be corrected and the data of the affected time windows could not be analyzed.

Additionally, the mechanical-structure of the RU prototype, including the accommodation of various instrument components and appropriate housing, probably added to the observed data noise. The contribution to the data noise induced by the mechanical-structure of a RU-3 with the fixed seismometers was certainly different than for the RU-10 with the self-leveling seismometer in cardan suspension, without having examined this in greater depth at this point.

While the current design of the RU can be considered a prototype, a space flight version will require many development steps to be taken.

For example, it must be ensured that the devices survive the harsh mechanical stress from launch and the landing on the Moon. To do this, for example, the structure would have to be reworked and reinforced in order to survive the vibrations and high-g forces that occur during launch and (to lesser extent) the landing. Radiation resistance and other performance targets would also require further changes and adjustments to the structure of the RU. Each of these changes would again provide a contribution to the noise levels. Thus, in the development of a space qualified model, it would be absolutely necessary to monitor the changes made to the structure for their contribution to the noise levels and, if necessary, to make changes in this respect.

Since a RU could work autonomously, even in remote and possibly dangerous regions, it would be conceivable to further develop this approach for Earth applications. If equipped with appropriate memory, it would be conceivable to deploy a Remote Unit (or even a set of RUs) for autonomous offline operation. The collected data could be temporarily stored in an internal memory. These could then either be collected together with the RUs when the measurement setup is disassembled, or the data could be retrieved at regular intervals via a radio link if the equipment is equipped with the appropriate technical features.

If the RUs were designed and adapted to be sufficiently robust, it would also be possible to deploy them in areas potentially dangerous to humans. For example, a remote-controlled robot could deploy a suitable RU in the vicinity of a volcanic crater where heat or toxic gases prohibit people from staying for longer periods. In this case, the modular design of the RUs would also allow the placement of various other measuring instruments, since the platform of the RU is not limited to carry seismic sensors alone.

6.3 Field studies with robotic equipment

The Apollo missions endowed mankind with a vast treasure of data of indescribable value. But on the other hand, immense resources in form of material, manpower, working hours and especially money had to be spent to obtain this treasure. Moreover, many dangers were also connected with the missions.

Then as now, one would like to keep the dangers for people as low as possible. Today, autonomous robotic systems offer us new possibilities that were not available in the 1970s. With the robotic systems of our time, remote areas that are hostile to human life can be visited and explored.

The use of robotic systems for space applications is on the increase. For example, the remote-controlled Mars rover Curiosity has been exploring the surface of the red planet since August 2012 (Grotzinger et al, 2012). Curiosity was a remote-controlled rover, but due to the longer data transmission times, such a probe could hardly be controlled interactively, since a camera signal could only give a reaction to any control command after 8 minutes at the earliest (minimum delay of around 4 minutes and maximum delay of around 24 minutes for one way signal transmission). Therefore, especially when considering even more distant mission objectives, an obvious solution for future missions will be to consider an autonomous - or even partially autonomous - robotic system.

The Rover Lightweight Roving Unit (LRU) (Wedler et al., 2015) used by ROBEX was able to demonstrate its capabilities during the demonstration mission carried out on Etna in 2017. Paper IV (in the appendix) presented the scientific proof-of-concept in section 4.4 (cf. page 88).

In this section, the data recorded by the autonomous robotic system were scientifically evaluated in accordance with a real lunar mission. The results showed that in the investigated area near the Laghetto cinder cone comprised a loose rock layer with a low P-wave velocity of about 92.4 m/s, which lay above a more solid layer with a P-wave velocity of about 245.5 m/s. This was not only a good approximation of the scientific studies published by Coltelli et al. (2007) on this area, but also showed striking similarities to the results of Apollo mission 14, 16, and 17, which also showed a loose cover layer with very low seismic P-wave velocities of about 100 m/s. This agreement led to several conclusions. Firstly, the chosen test site at Etna could be confirmed as a good analogue territory for lunar missions due to the similarities to the Apollo results. On the other hand, this also showed that the scenario developed and discussed within the framework of ROBEX for an active, robotic experiment to explore the Moon could achieve good results compared to a mission carried out with astronauts.

The paths for future research were particularly diverse here. From a purely technical point of view, many further developments are already conceivable here: Further developments of autonomous navigation, object handling, or motorized movement on different surfaces are only a few examples. Within the framework of ROBEX the active seismic source required for the scenario was not further

explored. Already during the first CEF (Concurrent Engineering Facility) study it became clear that the development of such a source could not be managed within the limited time and financial framework of this Helmholtz Alliance project. For the demonstration mission, a sledgehammer with an impact plate was chosen (inexpensive and easy to implement). But several versions were discussed, so different systems with reusable or rechargeable mechanisms were conceivable (e.g. spring mechanisms, railguns, drop weights, etc.).

The use of Explosive Packages, as with the Apollo 17 LSPE, provided a limited scenario due to the limited availability at the test site (you only have as many usable signals as you have brought explosive charges). Therefore, the development of a reusable and rechargeable active source would be an important step for future missions.

6.4 Future lunar exploration

The Moon continues to fascinate scientists of all disciplines and is still of great interest. This is clearly shown by the fact that many future missions have our Moon as their target. After some remote sensing missions, such as the Lunar Reconnaissance Orbiter, landings are now again a focus of planned missions.

The Japan Aerospace Exploration Agency (JAXA) is planning the Smart Lander for Investigating Moon (SLIM). SLIM can be seen as a kind of technology demonstration. It is intended to test newly developed landing techniques. Up to now the target body, in this case the Moon, has been searched for suitable landing sites that could be optimal for landing a spacecraft, which did not always mean that the landing site was of high scientific value. With new techniques it should now be possible to land a spacecraft at any desired and hence scientifically interesting point. It is hoped that this technical trial will also provide a new push/boost for the entirety of lunar research. (Source: JAXA, https://global.jaxa.jp/projects/sas/slim/, request May 2020).

Not only Japan shows a continued and developing interest in lunar exploration. The Russian space agency ROSKOSMOS is also planning further missions. Until 1976 the Soviet Union carried out a long series of lunar missions within the Luna program. Now they want to resume and continue these early Soviet Moon missions. Among the missions currently planned (and approved by the Russian government) are both lander and orbiter missions. Hence, Luna-25 (also known as Luna-Glob-Lander) will be the restart of the new Russian lunar missions and will land on the lunar surface. This time an area near the lunar south pole is planned for the landing. The following Luna-26 (also known as Luna-Resurs-Orbiter) will be an orbital mission in a deep polar orbit (approx. 50-100 km). This will be followed by another landing mission with Luna-27 (or Luna-Resurs-Lander). Luna-27 will explore in-situ lunar regolith.

In addition, further missions within the framework of the Lunar Polar Sample Return mission (LSPR, or Luna-Grunt) with European participation are already being planned (source: Space Research Institute of the Russian Academy of Sciences - IKI, www.iki.rssi.ru/eng/moon.htm, request May 2020).

These aforementioned missions are unmanned and mainly technical demonstrations, but the new technologies demonstrated here open up previously unexplored landing areas and new science objectives (e.g. exploration of ice deposits and volatiles).

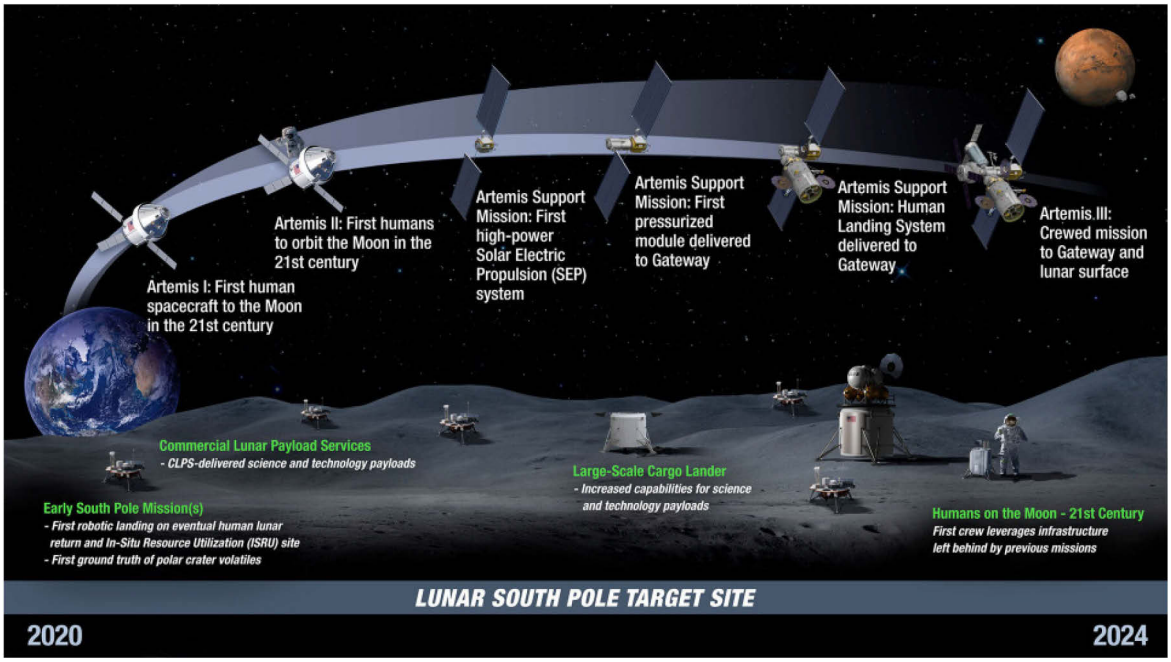

Figure 47: Timeline for Artemis programm. (Credit: NASA).

Also In addition, NASA has ambitious plans concerning the Moon. The Moon is seen here as a proving ground for new technologies and as a step stone for manned missions to Mars. But manned landings on the Moon are also being discussed again. As the then US Vice President Mike Pence said: "The next man and the first woman on the Moon will be American astronauts." (Source: NASA Twitter, November 14, 2019). This is the goal of the Artemis program which is developed with the cooperation of international partners. The timeframe is very tight, and the plan is to land human astronauts on the lunar surface by 2024. Artemis comprises several sections. A network of launch structures on Earth, an extremely powerful rocket called Space Launch System (SLS), the deep space Command Module Orion, the Gateway space station in lunar orbit, a highly sophisticated lander to bring people to the lunar surface and special surface spacesuits. All together should make it possible to bring people to the Moon again by 2024. With robotic, but also manned landings, more of the lunar surface shall be explored than ever before.

In particular, NASA intends to cooperate with international partners in the construction of the Gateway Space Station. The Gateway Station is not only suitable as an intermediate station to the Moon, but should be able to serve as a kind of spaceport in the future. It combines the characteristics of a research platform, communication center and orbiting base camp for Moon missions, but is also intended to serve as a springboard for missions to Mars or even further out in our solar system. The many missions planned for the Moon demonstrate the continuing importance of lunar research even beyond the Apollo era. People want to learn more and more about Earth's satellite in order to better understand the Moon, its formation and the Earth-Moon system. But the Moon also offers the unique opportunity to test technologies in the immediate vicinity of the Earth that are necessary for manned and robotic missions to more distant planets (Mars).

6.5 References

Coltelli, M., Proietti, C., Branca, S., Marsella, M., Andronico, D., & Lodato, L. (2007). Analysis of the 2001 lava flow eruption of Mt. Etna from three-dimensional mapping. Journal of Geophysical Research: Earth Surface, 112(F2).

Cooper, M.R., Kovach, R.L., (1975), Energy, frequency, and distance of moonquakes at the Apollo 17 site. In: Proceedings of the Conference Paper presented at the Lunar and Planetary Science.

Cooper, M.R., Kovach, R.L., Watkins, J.S., (1974), Lunar near-surface structure. Rev. Geophys. 12 (3), 291–308.

Duennebier, F., Sutton, G.H., (1974), Thermal moonquakes. J. Geophys. Res. 79 (29), 4351–4363.

Grotzinger, J. P., Crisp, J., Vasavada, A. R., Anderson, R. C., Baker, C. J., Barry, R., ... & Wiens, R. C. (2012). Mars Science Laboratory mission and science investigation. Space science reviews, 170(1), 5-56.

Haase, I., Gläser, P., Knapmeyer, M., Oberst, J., Robinson, M.S., (2013), Improved Coordinates of the Apollo 17 Seismic Profiling Experiment (LSPE) Components. In: Proceedings of the 44th Lunar and Planetary Science Conference (Paper presented).

Haase, I., Wählisch, M., Gläser, P., Oberst, J., Robinson, M. S., (2019), Coordinates and Maps of Apollo 17 landing site. Earth and Space Science, 6, 59-95.

Kovach, R.L., (2015), Person communication.

Nakamura, Y., (2011), Timing problem with the Lunar Module impact data as recorded by the LSPE and corrected near-surface structure at the Apollo 17 landing site. J. Geophys. Res.: Planets, (1991–2012) (116(E12).

NASA Document, (1972), Apollo Lunar Surface Experiments Package. Apollo 17 ALSEP (ARRAY E) Familiarization Course Handout, NASA-CR-128636, September.

Wedler, A., Rebele, B., Reill, J., Suppa, M., Hirschmüller, H., Brand, C., ... & Lichtenheldt, R. (2015, May). LRU-lightweight rover unit. In Proc. of the 13th Symposium on Advanced Space Technologies in Robotics and Automation (ASTRA).

Smart Lander for Investigating Moon (SLIM), JAXA, https://global.jaxa.jp/projects/sas/slim/, last request May 2020

Luna Program, Space Research Institute of the Russian Academy of Sciences - IKI, www.iki.rssi.ru/eng/moon.htm, last request May 2020

Artemis Project, NASA, https://www.nasa.gov/specials/artemis/, last request May 2020Gateway, esa, https://www.esa.int/Science_Exploration/Human_andRobotic_Exploration/Exploration/Gateway , last request May 2020

7. Synthesis

The goal of this thesis was to study whether the position changes detected by the Lunar Reconnaissance Orbiter of the instruments used on the Apollo 17 LSPE and the associated distance changes between the instruments lead to changes in the calculated velocity-depth profiles. Motivated by these experiences from Apollo 17 an active seismic experiment was developed that would be suitable for future lunar exploration.

In a first step, the deciphering scheme for the Apollo 17 binary data had to be reconstructed within the framework of research paper I. With the help of this scheme it was possible to use the original bitstream in its entire length for the re-analysis of the seismic data. The seismic signals were processed with a Wiener filter to determine new arrival times of the P-waves. Previous P-wave arrival times (Kovach, 2015, pers.comm.), newly determined P-wave arrival times (from this study), previous coordinates (Cooper and Kovach, 1975), and new LROC-based coordinates (Haase et al., 2013, Haase et al., 2019) were then used for creating alternative models of the subsurface structure near the Apollo 17 landing site. The results of the different combinations were discussed in research papers I and II. In summary, the use of different arrival times (new and old) causes only minor changes in the seismic velocity-depth profiles. However, the transition between old and new coordinates leads to significantly different models. In general, the layers become thinner and the P-wave velocities become higher, which leads to a stronger increase of seismic velocities with depth. This is an indication that the subsurface beneath Apollo 17 landing site is more compacted than previously thought.

The so-called Remote Units were developed within the ROBEX Alliance. These units contain all required subsystems in a compact instrument carrier and autonomously record scientific data over a certain period of time. In research paper III two types of these Remote Units were presented, suitable for recording seismic data. A 3 kg version with fixed three-channel seismometer (RU-3) and a 10 kg version with fold-out solar panels and a three-channel seismometer in cardan suspension (RU-10). One part of the work was then to test whether the developed Remote Units were suitable for recording seismic data in a scientifically usable quality. For this purpose the noise levels of the units were compared with those of standard off-the-shelf seismometers of Lennartz 3Dlite Mark II type.

As mentioned before, the Remote Units (in their current state) showed increased noise levels for which various structural and electronic reasons have to be considered. If the devices should undergo further development with regard to their structure and features, an ongoing investigation of the noise level would be necessary. Then further adjustments with the aim of reducing the noise level to a standard level would have to follow.

The developed Remote Units were subjected to performance tests during a demonstration mission at Mt. Etna, Italy.

Within the framework of ROBEX, an active seismic experiment for lunar exploration was developed, which could be carried out with (partly) autonomous robotic systems. The developed scenario is similar to the set up used during Apollo 17. The Y-shaped setup of four Remote Units (equipped with seismometers) is well suited for recording natural quakes including their localization. The array was used both actively and passively in the developed scenario. In the active part, one of the Remote Units was placed by a rover at regular intervals along a profile line, placed for measurements then - after recording the seismic signals generated by an active seismic source - picked up again by the rover and

transported to the next point of profile. To make the best use of the rover's resources, the profile line was chosen to lie along one of the outer edges of the array. After the active part, the rover then built up the rest of the Y-shaped array, which could then be used to record and locate naturally occurring events (like quakes or impacts).

An additional paper ("paper IV", see Appendix) describes the developed scenario and the demonstration mission at Mt. Etna, Italy, carried out within the framework of the ROBEX Alliance. The goal of the mission was to demonstrate the feasibility of the experiment in a lunar analogous landscape. Not only the scenario itself was demonstrated, but also different experiments of other research areas were tested (e.g. rover navigation and locomotion, lander setup and communication, etc.). As a focus of the work, the Remote Units were tested in the field (RU-3 and RU-10). Section 4.4 of research paper IV presents the evaluation of the data recorded during the demonstration mission. On the one hand, the evaluations could show that the knowledge gained about the near-surface subsurface at the test site corresponds to the known results for this region at the Laghetto cinder cone (Coltelli et al., (2007), and on the other hand, the results were very similar to those for the uppermost strata below the Apollo landing sites, which could confirm the choice of the test area at Etna as a lunar analogous terrain.

By combination of the original Apollo 17 LSPE data and modern LROC-based (and thus geometrically accurate) coordinates, this work has contributed to an improved understanding of the near-surface structures below the Apollo 17 landing site.

In a terrestrial field test near Mt. Etna, it could be demonstrated that local subsurface structures exist that resembled very much those discovered on the Moon during the Apollo missions. Hence, the field test area may act as lunar surface analogues. The Remote Units developed for this purpose are still in an early stage of development (i.e. they are not space flight certified), but show their general suitability for exploration of the Moon.

7.1 References

Coltelli, M., Proietti, C., Branca, S., Marsella, M., Andronico, D., & Lodato, L. (2007). Analysis of the 2001 lava flow eruption of Mt. Etna from three-dimensional mapping. Journal of Geophysical Research: Earth Surface, 112(F2).

Cooper, M.R., Kovach, R.L., (1975), Energy, frequency, and distance of moonquakes at the Apollo 17 site. In: Proceedings of the Conference Paper presented at the Lunar and Planetary Science.

Cooper, M.R., Kovach, R.L., Watkins, J.S., (1974), Lunar near-surface structure. Rev. Geophys. 12 (3), 291–308.

Haase, I., Gläser, P., Knapmeyer, M., Oberst, J., Robinson, M.S., (2013), Improved Coordinates of the Apollo 17 Seismic Profiling Experiment (LSPE) Components. In: Proceedings of the 44th Lunar and Planetary Science Conference (Paper presented).

Haase, I., Wählisch, M., Gläser, P., Oberst, J., Robinson, M. S., (2019), Coordinates and Maps of Apollo 17 landing site. Earth and Space Science, 6, 59-95.

Kovach, R.L., (2015), Person communication.

NASA Document, (1972), Apollo Lunar Surface Experiments Package. Apollo 17 ALSEP (ARRAY E) Familiarization Course Handout, NASA-CR-128636, September.

8. Appendix

Research Paper IV

A ROBOTICALLY DEPLOYABLE LUNAR SURFACE STATION FOR GEOPHYSICAL AND ASTRONOMICAL OBSERVATIONS

Lars Witte, Alexandra Heffels, Matthias Killian, Martin Knapmeyer, Caroline Lange, Norbert Toth, Geogios Tsakyridis, and Armin Wedler

a German Aerospace Center - Institute for Planetary Research, Berlin, Germany

b German Aerospace Center – Institute of Space Systems, Bremen, Germany

The final publication is available at Elsevier via

https://doi.org/10.1016/j.pss.2020.105080

Abstract

This article presents a system design and a surface operations concept for a robotically deployable, small scientific observatory on the lunar surface. The design reference mission scenario considers its implementation as part of larger international exploration mission such as the European Exploration Envelope Programme. The underlying science case particularly addresses scientific objectives for long term observations as part of scientific networks. Considered strawman payload for this surface station focuses on instruments which are – or could be – candidates for geophysical and astronomical observation networks. A seismometer, a radio experiment and an IR telescope have been taken as sizing case to assess the station's system budgets. First part of the article looks at the station design from engineering perspective whether a small modular station can address common needs of such instruments such as a sustained operation in the lunar environment. Focus is given to design features to enable the station's deployment by robotic assets. Secondly, the core unit of the conceptualized station has been built as engineering model including its basic system functions, interfaces to neighboring mission elements such as the lander vehicle and the rover and a set of geophones as representative for a science instrument. This hardware realization was used in a functional end-to-end demonstration from robotic deployment to delivery of geoscientific data. The mission demonstration has been carried out in a Moon analogue field test on Mt. Etna, Sicily/Italy and confirmed the general feasibility of the proposed concept for lunar scientific exploration. Particularly, the evaluation of the acquired seismic data confirmed its suitability for sub-surface exploration. Results from the Moon analogue test are presented together with the design details of the surface station and the necessary conditions for its implementation and use in a robotic exploration scenario.

8.1 Introduction

The Apollo missions carried scientific instruments for deployment onto the lunar surface and long-term operations after the astronaut's departure back to Earth. The Apollo Lunar Surface Experiment Package (ALSEP) was a self-contained system designed to sustain the scientific experiments for at least one year and transmit data directly to Earth. The scientific objectives were to obtain lunar geophysical and environmental data with varying experiments between the missions. A detailed overview of the various experiments can be found in NASA ALSEP, 1971. A central station contains the power distribution (excluding the radio-isotopic power source) and data subsystem as well as the back-end electronics of some of the scientific experiments. The experiments themselves are satellite stations around the central unit, interfacing it with umbilical cables. Until today, the rich data sets obtained by ALSEP are the only source of long-term observational data from the lunar surface. However, these data sets are limited to the lunar near side.

The Apollo missions 12 and 14 to 16 deployed ALSEP including seismometers forming a triangular network with approximately 1000 km baseline. Apollo 17 deployed a small Y-shaped array of four geophones with a base length of approximately 100 m (Haase et al., 2019). The purpose of this array was to record signals from explosive packages deployed by the astronauts (Cooper et al., 1974), the impact of the Apollo Lunar Module ascent stage and Saturn IV-B stages, meteorite impacts, and other natural seismicity in the vicinity of the Apollo lander.

Since then, seismology and the used instruments have evolved and latest instrument technology is used on Mars InSight mission (Lognonné et al., 2019). Scientific findings about the Moon's mantle are based on the seismic data gathered by afore mentioned ALSEP stations. Today, a state-of-art seismic network equipped with more advanced technologies would add to this knowledge base. Especially a lunar far side seismic network, e.g. in Schrödinger Basin, would thereby complement these Apollo near side data sets, as it is currently unknown if seismic activity on the far side of the Moon exists at all, and if the far side crust has the same overall structure as the near side crust. The lunar farside has been suspected to have a higher thickness than the nearside crust ever since it was found that the Moon's center of figure is offset from its center of mass towards the far side (Wollenhaupt and Sjogren, 1972). High resolution gravity data supports a difference in thickness of tens of kilometers (Wieczorek et al., 2013). The obvious absence of large maria on the farside and the presence of the Procellarum KREEP terrane on the nearside (Joliff et al., 2000) can be modelled in terms of an asymmetric thermal evolution (Laneuville et al., 2013) according to which the structure of the farside crust is actually the typical one. In view of coming initiatives for renewed lunar exploration the deployment of new networks such as proposed by Kawamura et al. as "Autonomous Lunar Geophysical Package" dubbed ALGEP in response to the long-term plan of the ESA Science Program.

Another lunar surface science case candidate under discussions by its stakeholders is the astronomy case, although this case has not yet a similar back log like the Apollo-based seismic network observations. Nevertheless, there is much consensus (Foing, 1994; Crawford, 2008; Silk, 2018; Harwit, 1994) among the science community that the lunar far side provides a suitable and stable ground for the deployment of radio science observatories. For the radio science case this site profits from the shielding of Earth radio emissions creating a radio quiet zone. Lack of Earth atmosphere enables low frequency observations below 30 MHz. Less consensus is in the astronomer's community regarding the suitability of the lunar surface for optical or infrared observations. Mentioned advantages are that observations would profit from the very cold thermal background, the absence of atmospheric disturbances. Opinions differ about the adverse impact of lunar dust which is recognized as disadvantage compared to free-flying observatories (Crawford 2008). Oppositely, dust and cleanliness

are not regarded as prohibitive factors by Harwit1994 given the 20 years (at date of his publication) of experience with the Apollo deployed laser reflectors. This assessment is backed by recent results and the operational experience of China's Chang'e 3 mission about environment-related performance degradation, reported by Wang et al., (2015). Particularly interferometric observations could benefit from a very geologically stable surface. Such optical interferometric installations require the deployment of an array of telescope and have been described over the past years by several working groups, e.g. Rayman and Saunders (1996), and Schneider et al. (2019). Proposed array dimensions are in the order of 100 m and are in that regards similar to the Apollo 17 geophone array set-up.
The effort for the installation of astronomical observatories is regarded as a major disadvantage which can or must be traded as well against the costs and benefits of orbiting observatories. The potentially high installation effort is recognized as well by the geophysical community although there is obviously no alternative to be traded against such surface installation. In response to these scientific needs a system engineering study and a field-testing campaign was done with the two mainmobjectives:
The first objective of this engineering study was the conceptualization of a long living and lunar-night operating surface station. This station shall become robotically deployable for the purpose to set up scientific networks within the framework of a larger lunar surface operations concept. The reference mission scenario into which the presented study results are assumed to be embedded is introduced in chapter 8.2. Here the concept of operations is provided together with the reference scientific instruments. The investigated scenario and the later functional demonstration in an analogue environment are limited to surface operations, thus excluding launch, cruise and landing phases. The baseline design of the monitoring station is then outlined in chapter 8.3. It addresses basic questions on thermal and power subsystem design with regard to lunar night time survival. It shows the conceptual design of observatories for a reference mission equipped with a notional payload consisting of a seismometer and astronomy instruments together with the resulting overall systems budgets for mass, power and data.
The second objective of the project was to validate a surface exploration mission concept involving several robotic assets with a field tests. Chapter 8.4 summarizes the implementation of the relevant mission elements as bread boards and functional mock-ups and their testing in a Moon analogue environment on Mt. Etna/Sicily. In this context, the concept of operations and its functional building blocks are validated. Additionally, the chapter provides insight into the needed effort for the installation of such system. The hardware implementation is however limited to the core unit of such observatory with a set of geophones for a functional end-to-end demonstration.

8.2 Reference mission and concept of operations

New opportunities to deploy such long-term observatories arise in the frame of future robotic lunar exploration missions such as ESA's European Exploration Envelope Programme (Carpenter, 2019).
A region of interest is the Schrödinger basin, which has been identified as area satisfying needs and interests of different scientific communities (Kring, 2013). Accordingly, associated detailed engineering and scientific preparatory work has been done by international working groups to assess the outline and feasibility of such mission (or several). This existing preparatory framework is used by this study as reference for finding a baseline design for the observatory's core system and mission elements.
Landing site and operations area are inside the Schr€odinger basin around coordinates of 141.33°E/75.47°S and 141.89°E/75.30°S. Those are identified as "Schrödinger 1" and "Schrödinger 2"

in the Human Lunar Exploration Precursor Program's Mission Analysis Guideline (Renk et al., 2017) and are taken as reference for further analysis. In this study, the Lander element acts as central station during surface operations supporting the operation of the rover and the seismic network and acts as data relay for communication between the surface elements and the ground station. The deployment considers the required accessibility of the monitoring stations by a rover element and its manipulator arm. The rover deploys the monitoring stations while ground segment intervenes only at check gates to assure and confirm the correct build-up. Therefore each one of the four monitoring stations is ianded over to the rover. The rover thereby travels to the assigned points of scientific interest and handles and places the station. This activity is repeated until a Y-shaped network is built (Figure 48).

Environmental protection for the instrument over the total mission duration is provided by an external housing. The surface station is capable of providing thermal control and power to the payload instrument while acts as a relay for data exchange (tele-commands and telemetries).

The reference instrumentation considers (i) seismometers and a suite of astronomy payloads which is either (ii) a radiofrequency antenna experiment or (iii) an infrared telescope or combination

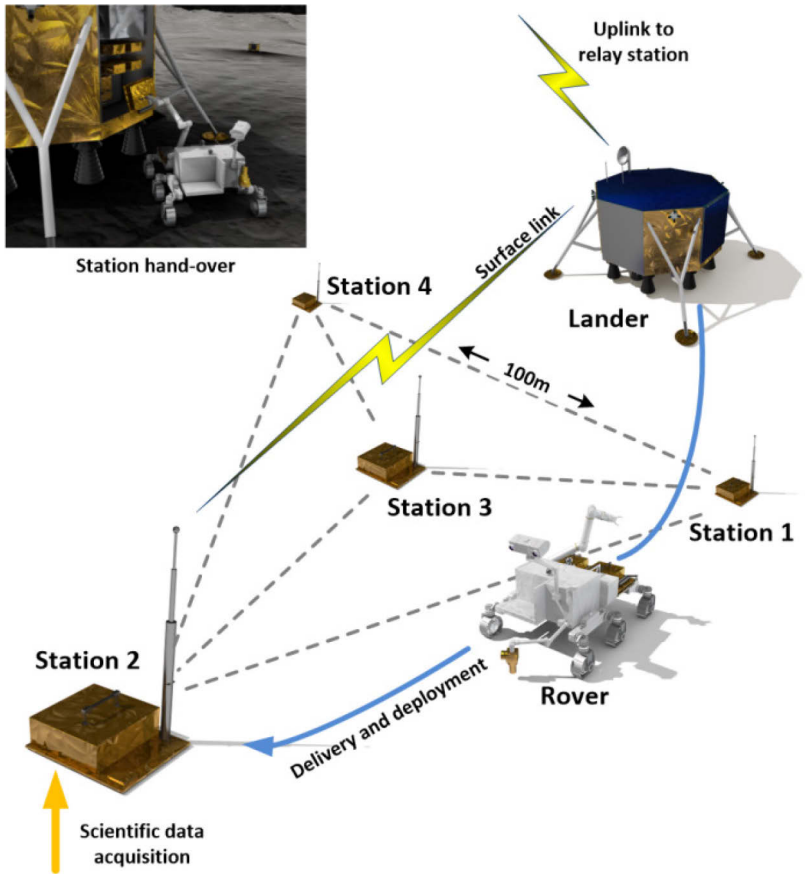

Figure 48: Early system architecture, its main mission elements and Y-shaped array similar to the Apollo 17 geophone array.

therefrom. Strawman instruments and their requirements considered in this study have been already operated or at least proposed and studied to a suitable readiness level.

(i) Seismometer µ-SEIS: The µ-SEIS is a micro-electro-mechanical system (MEMS) based sensor design which strapped onto its housing structure and described by (Pike et al., 2014). A similar design is currently operational as short period (SP) seismometer as continuously operate both during lunar day and night being coupled to the lunar surface in a defined orientation with regard to the North-East-Up (NEU) frame. The instrument generates an output of approximately 155 Mbyte of uncompressed data per day. An array of four seismometers, placed at the corners and the center of an equilateral triangle (thus forming a "Y") will work as a phased array antenna, allowing for determination of the propagation direction of incoming wave fields. To compare with the performance of the Apollo 17 seismic experiment, the corners of the triangle shall be about 100 m apart. Artificial seismic sources such as hammer strokes, high explosives and impacts of spent spacecraft stages allow sounding the subsurface to a depth of several hundred to a few thousand meters, depending on their distance to the sensors.

(ii) Lunar Radio Experiment (LRX): The LRX instrument described by Klein Wolt et al., (2012) has the objective to demonstrate the suitability of the lunar surface for low frequency astronomy. It could thereby act as a precursor element for a lunar low frequency array. It consists of a single tri-pole antenna and operates in the 10 kHz to 100 MHz frequency range with specific bands of dedicated to radio plasma science and to radio astronomy. Budgets, technical and operational requirements for this instrument are taken from the former ESA Lunar Lander Payload Definition Document, compiled by Carpenter (2010). The LRX shall operate during the Lunar day and night and requires radio silence or sufficient bandwidth spacing to operations communication links. It works in two different modes which are: the nominal measurement mode of 5 min duration every 20 min and the burst measurement mode with a prolonged duration of 5 h per week. Both the nominal mode and the burst measurement mode generate 100 Mbit of data each.

(iii) Infrared (IR) Telescope: the telescope reference design is based on the Skyhopper 12U cubesat-borne IR telescope proposed by Greiner et al. 2017, designed for a low Earth orbit mission. Its objectives are the detection and study of exoplanets and the detection of early star formation after the Big Bang using the afterglows of Gamma-ray burst. The optical systems features an aperture of 19 x 9 cm for the main mirror with a focal length of 2000 mm and a 4 channel optical to near-infrared imager in the range of 0.8–1.7 µm. The 2 k x 2 k IR sensor detector requires cooling down to a temperature of 140 K. Its technical properties are described in Teledyne (2012). The IR sensor is actively cooled in this orbiter scenario. In the lunar surface science scenario considered in this study however a modified variant of this telescope is assumed with an aperture of 19 cm. Instrument cooling shall be achieved passively through utilization of the cold lunar night environment.

8.3 Surface stations and baseline design

The observatory's core unit shall be able to support the instruments and provide the below specified functions for the total duration of the mission and over the expected range of environmental parameters, e.g. temperature, radiation or others for Earth environments). In order to ensure no loss

of functionality or system degradation, the supporting bus system shall provide the following functions:

- Self-sustaining operations
- Deploy antennas and solar arrays
- Supply power to bus and payload
- Provide data handling and communication with other mission elements (lander, rover)
- Measure attitude with regard to the local gravity vector
- Provide service functions for payload operations such as data compression

Sizing constraints regarding mass and volume arise from the bearing capacity of the rover/manipulator element. No assumption on a specific bearing capacity or predetermination by an existing rover design is made here. Nevertheless, it is assumed that the arising mass limit is in the order of 25 kg at best. Modularization of the station would be required to meet a rover's handling limits. A cube or brick-shaped housing with easily accessible handling interfaces is pursued as facilitating rule for this purpose. Drawing upon DLR's successful Mobile Asteroid Surface Scout (MASCOT) system (see Figure 49, described by Ho et al., 2017), the design follows the MASCOT configuration of having dedicated warm and cold compartments, enabling a physical separation between the compartments as well. The system concept has been further developed in concurrent engineering studies and further design workshop. The core avionics with on-board computer and data handling are inherited from MASCOT, with minor adaptations. Further heritage design principles are the carbon fibre structure design and the Common E-Box (CEB or E-Box) which houses both system avionics and payload back-end electronics.

Figure 49: MASCOT flight model whose core design is adapted in this study as a baseline for lunar science surface station.

Table 8:Total masses and mass breakdown of the surface station.

	Components	Mass [kg] inkl. Margin
Core Unit	OBC/DHS	0.85
	Communication	0.42
	Power	12.19
	Attitude Sensor	0.05
	Harness þ Interfaces	1.97
	Structure	1.96
	Thermal Control	0.42
	Payload (Seismometer)	0.36
	Payload (LRX Electronics)	1.00
		19.21
Payload Unit	Harness þ Interfaces	1.21
	Structure	0.85
	Mechanisms	1.10
	Thermal Control	0.12
	Payload 2 (LRX Antennae)	0.66
	Payload 3 (IR-T.)	7.20

Major modifications of the core unit comprise a new power subsystem, accommodating solar generators, larger battery capacity and an improved thermal design. The mechanical interfaces have been redesigned to enable interaction with the rover element and handling. The domain specific analyses and design justification are provided later in this work in more details.

Table 9: Daily data volume generated by instruments and system.

Unit	Data volume [MByte/day]
System Housekeeping	33
Seismometer	257
IR Telescope	859
Radio Experiment	966
Total	2115

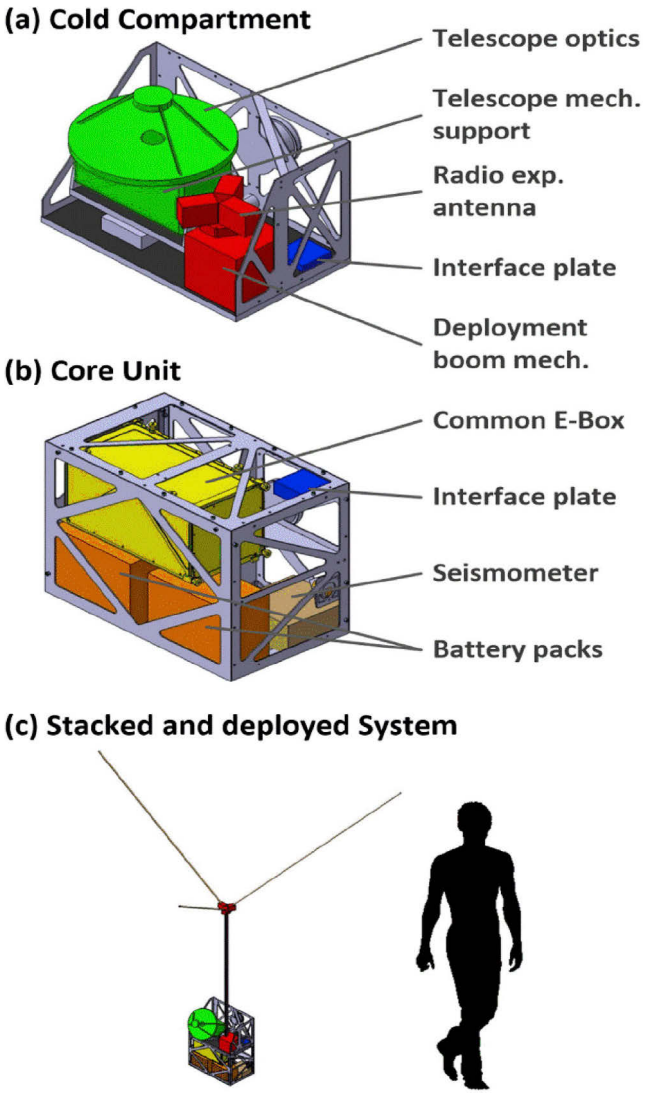

Figure 50: Accommodation drawings of the lunar observatory with two stackable modules.

The resulting system configuration and its principal dimensions for the above mentioned reference mission are depicted in Figure 50. The monitoring station consists of a core unit (depicted in Figure 50 b)) which contains the E-Box, battery packs and the seismometer. The E-Box houses the on-board computer, the power distribution and control unit, the communication system, and payload back-end electronics. An electronic interface is also considered in this concept study as port towards the stackable cold compartment. The cold unit (depicted as a) in Figure 50) is designed as a dedicated unit, exposing astronomical instruments to the cold night sky. It carries mechanisms to deploy and point the observatories. Multi-layer insulation, solar arrays and dust shields are not shown in this configuration drawing. The associated mass budgets are tabulated in Table 8. Components mass includes margin add-on according to their respective maturity level. The total mass includes therefore a margin factor 15%.

The observatory operates in three modes. These modes are:

1) Day science mode: The seismometer and radio experiment are active and gathering data. The IR telescope is de-activated whereas the latter one is in a stowed configuration. The station is transmitting the scientific and housekeeping data in dedicated communication windows to keep radio silence during LRX data acquisition phases. The station's batteries are recharged via the solar generators. Nominal duration is 13 days.
2) Night science mode: all instruments are active and gathering data. The station transmits data only in dedicated communication windows to ensure radio silence. All electrical power is provided by the battery system. Nominal duration is 13 days.
3) Sleep mode: this mode is entered in the transient phases between lunar day and night to let the station cool down or warm up. It gives especially the IR telescope the required time to attain the required detector temperature. The seismometer has an out time to avoid a phase with thermo-mechanical cracking noise. Duration is one day around each transition.

The illumination conditions driving these modes and used to size the thermal and power subsystems refer to the Schrödinger 1 site while start of operation is assumed mid of April 2025.

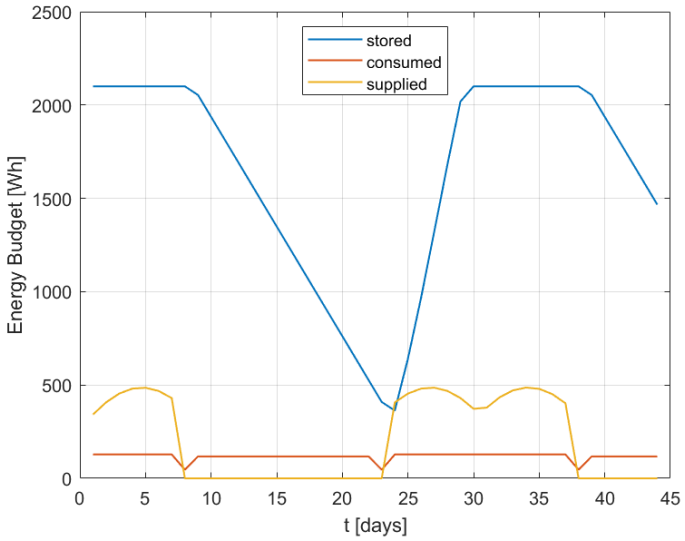

Figure 51: Daily power budget evolution over day/night cycle.

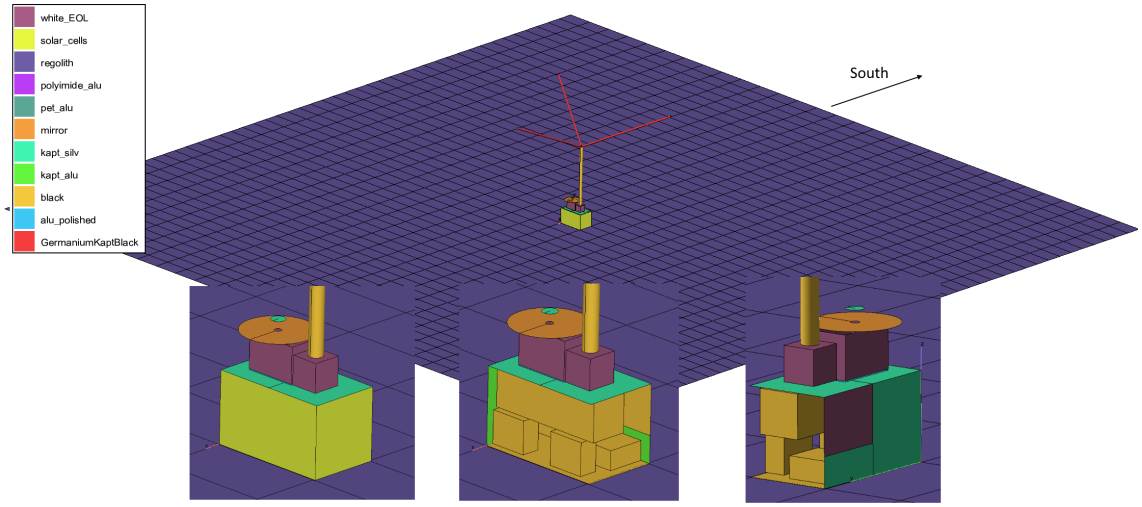

Figure 52: Geometrical and optical properties of thermal model.

8.3.1 Avionics

8.3.1.1 Onboard computing, data handling and communication

The onboard computing and data handling architecture OBC/DHS of the MASCOT surface package is re-used in this concept study with some modifications to accommodate the Lunar environmental conditions. These modifications affect the mass storage concept. The architecture consists of a cold redundant onboard computer and 2 x 4GByte RAID 1 memory. The OBC provides further services to the payload such as 24 Bit analog-to-digital-sampling, running instrument back-end software if required or optional data compression. Science data is explicitly time tagged. Data compression of 80% is considered in this study to reduce the volume of data actually transmitted. The uncompressed volumes of data are tabulated in Table 2 and include meta data and time tag data in addition to the science data.

A communications architecture using a lunar surface relay station as node to uplink to an orbiting gateway station is considered in the baseline design. It is assumed that the landing vehicle remains active to collect and bundle the data streams from several observatories which are part of a star or mesh topology. The observatories' service communication is restricted to the 2–3 GHz band following the recommendations of the International Telecommunication Union (ITU), stated in ITU 2013 and ITU 2017, to maintain a radio quiet zone for the radio astronomy experiment.

The communication hardware takes a full-duplex S-band transceiver of type satlab SRS-3 into account to satisfy this frequency restriction as well as the station's mass and volume constraints. This transceiver features an adjustable transmitter output power up to 30 dBm and a maximum bit rate of 512kbps (Satlab 2018). The communication distances are assumed to be in a range of 0.1 km–1 km and are individually determined by the observatories' position in the Y-shaped array and its relative deployment position with regard to the lander node. Duty-cycling of the data link is a necessity to achieve average low power consumption. One transceiver is on stand-by throughout the complete mission time but transmits during 5% of the night time and 15% of day time. A second transceiver remains as cold-redundant unit similar as the onboard computer.

8.3.1.2 Attitude reference sensor

Both the seismometer and the IR telescope require a precise alignment along the local gravity vector. The station's core unit takes into account an inertial reference sensor for this purpose. A tri-axial acceleration measurement unit has originally been developed for MASCOT but ultimately has not been flown on this mission. This unit was developed with two different form factors which are a stand-alone tetrahedral body or a flat board-mounted configuration using the same standardized interfaces as the other landers common E-box electronic boards. Both configurations combines 4 single MEMS sensors providing the required low noise ratio (7 µg/√Hz typical for 2 g full scale version) for resolving the impact accelerations experienced by MASCOT. The PCB version is taken as static gravity vector reference in this baseline design and is considered in the budgets accordingly. The stand-alone version of it has been built and implemented in the bread board version of the station's core unit and used in the field tests. Chapter 8.4.1.1 provides more information on the bread board unit and its configuration.

8.3.1.3 Power subsystem

The design of the power subsystem considers the power demand figures given in the following table. It shows the respective peak power values for the onboard computing and data handling unit and the communication subsystem as well as those of the scientific instruments. An effective average power demand depending on their specific duty cycle is given for each of the station's operating modes. The demand budget is shown in Figure 51 in terms of daily Watt-hours for 44 consecutive days starting mid-April 2025. The power consumption values of Table 3 are considered therein with an additional margin of 10%. Concerning power generation, the station design foresees bodymounted, non-deployable solar arrays on the station's East, West and North facing panels. Triple junction GaAs solar cells with an efficiency of 23% and a total active area of 0.138 m2 are considered. Given the station's geometry and North-facing orientation at its deployment site then a daily supplied amount of energy of nearly (peak) 500 Wh is obtained with a lunar day/night cycle as shown Figure 51. For the batteries an off-the-shelf and mature Li-ion technology (Buckle and Roberts, 2017) with a capacity of 189 Wh/kg and an allowed depth-of-discharge of 90% is examined. A storage capacity of ~2100 Wh is required with 11.1 kg battery mass when accounting for the tabulated supply and demand. The resulting battery charging state is likewise shown in Figure 51 along the station's operating cycle. This graph highlights the fact that the number of charge/discharge cycles over the stations lifecycle will remain fairly low as the mission stretches over 35 days.

Table 10: Power consumption figures of system and payload elements.

	Power [Wpeak]	Power in mode [Wavg]		
		Day	Night	Sleep
OBC/DHS	2.7	2.7	2.7	1.25
Communication	5.0	1.3	0.75	0.5
Seismometer	0.15	0.15	0.15	0.0
Lunar Radio Exp.	5 to 10	0.7	0.7	0.0
IR Telescope	5.0	0.0	0.15	0.0
		4.85	**4.45**	**1.75**

8.3.2 Structure and mechanisms

The monitoring stations structural design uses a lightweight, high strength carbon-fiber reinforced plastic (CFRP) framework with dedicated grapple element for the robotic arm on its front side. For the current study actual launch loads are considered as dimensioning loads. The interface to the landing vehicle's payload compartment is defined by four separation mechanisms at each corner to enable a stiff connection. The subsystem and instrument boxes within the CFRP-structure are accommodated to have connections close to the framework intersections in order to achieve a loading of the struts in mainly axial direction. The underlying load assumptions comprise random vibration (based on MASCOT CEB) of 15gRMS and a design limit load of 77.5 g. The maximum strain criterion is 0.3%. The design was verified for the core unit with a finite element model and a natural frequency of 138 Hz is calculated. Its first natural frequency is calculated at 138 Hz.

The deployment boom to elevate the antenna head (with its own instrument provided deployable tri-pole) is regarded as a system-provided mechanism. This mechanism makes use of a technology developed originally by DLR with the intent to deploy solar sails and other large Gossamer structure (Block et al., 2010). Such stiff but low mass boom is formed by two bonded and thin-walled carbon fiber half shells. When flatted, these booms can be coiled-up into a very small stowage volume. It resumes its tubular cross-section after being driven out and uncoiled by an electro-mechanical mechanism (Richter et al., 2019). A boom length of 1.0mis considered for the purpose of LRX antenna deployment in this study.

Contrarily, the elevation and azimuth mechanism of the IR telescope is regarded as part of the telescope unit itself. This is due to the involved high tolerances and stiffness requirements for such instruments which typically require an integrated design of its optical system and mechanical support framework. Such instrument design is however not elaborated in this study but reasonable estimates on associated budgets have been made to enable the overall observatories system assessment.

8.3.3 Thermal analysis

A geometrical mathematical model (GMM) and a thermal mathematical model (TMM) are developed and simulated at Technical University of Munich. The modelling approach allows for quick changes in thermal design leading to a robust, passive solution after little iteration. This chapter presents analysis of the most promising thermal configuration only. A crucial element in the frame of this study is a detailed model of the Moon's surface. The implemented model bases on the two layer model of Vasavada et al., (1999). However, thermo-physical properties are considered constant instead of temperature dependent in order to speed up simulation time. Furthermore, the mesh of the surface matches the footprint of the monitoring station. Otherwise, faulty results can occur because temperatures underneath the station are simulated incorrectly. Analysis include dynamic simulation of a full lunar day representing worst cold condition (latitude 78S, solar heat load 1320Wm^{-2}) and worst hot condition (latitude 68S, solar heat load 1420 W m^{-2}) for a mission to the Schrödinger Basin. A plane of size of 10 m x 10 m represents the surface of the Moon at the dedicated deployment site where the monitoring station is located in the center of the scene (Figure 52). The bottom face of the core unit is a glass-fiber panel, which is in direct contact to the regolith. Conduction occurs with a conductance of 50 W m^{-2} K^{-1}.

The details of the GMM can be seen in the sub-images of Figure 52. The colors indicate the thermo-optical properties of materials considered in the thermal design. Multi-layer insulation (MLI) sheets protect the warm compartment from the environment. In addition, solar cells have MLI attached on the backsides. Heat transfer through MLI occurs by radiation ($\varepsilon_{effective}$ = 0.009 W m^{-2} K^{-4}) and conduction ($k_{effective}$ = 0.016 W m^{-2} K^{-1}). A dedicated radiator emits excessive heat in order to meet temperature requirements. The cold compartment contains the IR telescope and the radio experiment with the deployment mechanism. For a closer analysis of thermal conditions of the IR telescope, its TMM considers the mounting structure, the primary and secondary mirrors M1 and M2, and the receiver element with the IR sensor. The connector interface between core unit and cold compartment leads to a heat conduction of 0.05WK^{-1} between the warm compartment and the telescope mounting structure.

The resulting temperature curves (Figure 53) show that a passive thermal design is feasible at the specified landing site. The temperatures inside the core unit tend to approach the warm end of the batteries' required operating range. Changes in the thermal design with heat switches are a viable mitigation option if necessary in a more detailed design. The mirrors and the sensor of the infrared telescope reach temperatures in the 110 K area and provide significant margin towards the required operating temperature (refer chapter 8.2, IR telescope section).

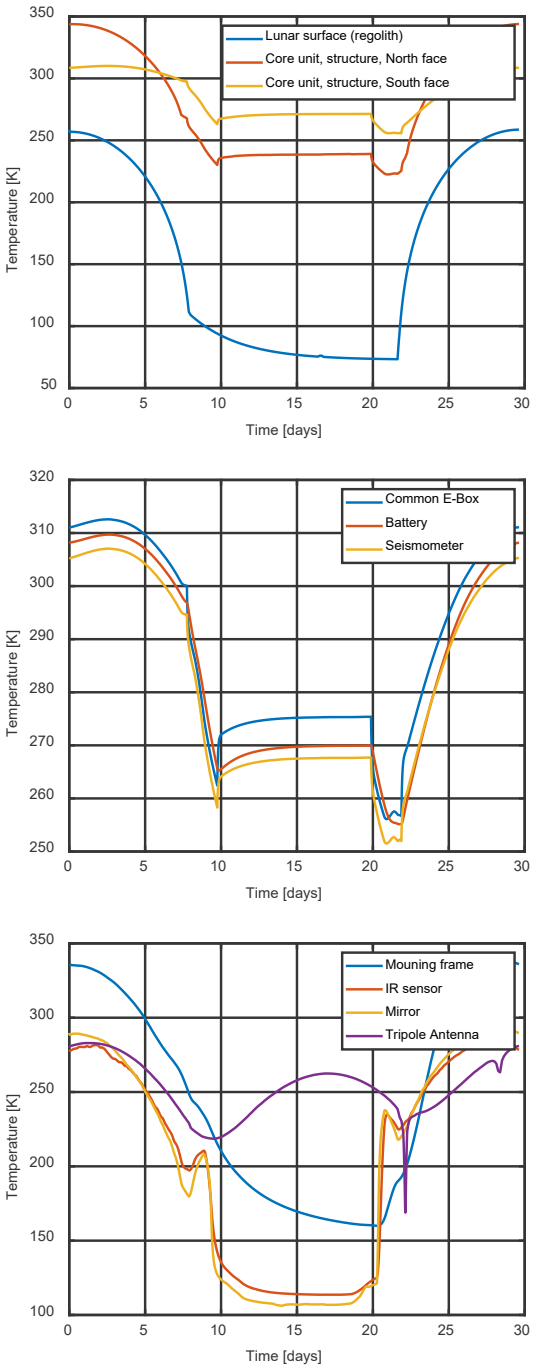

Figure 53: Temperature profiles along day/night cycle.

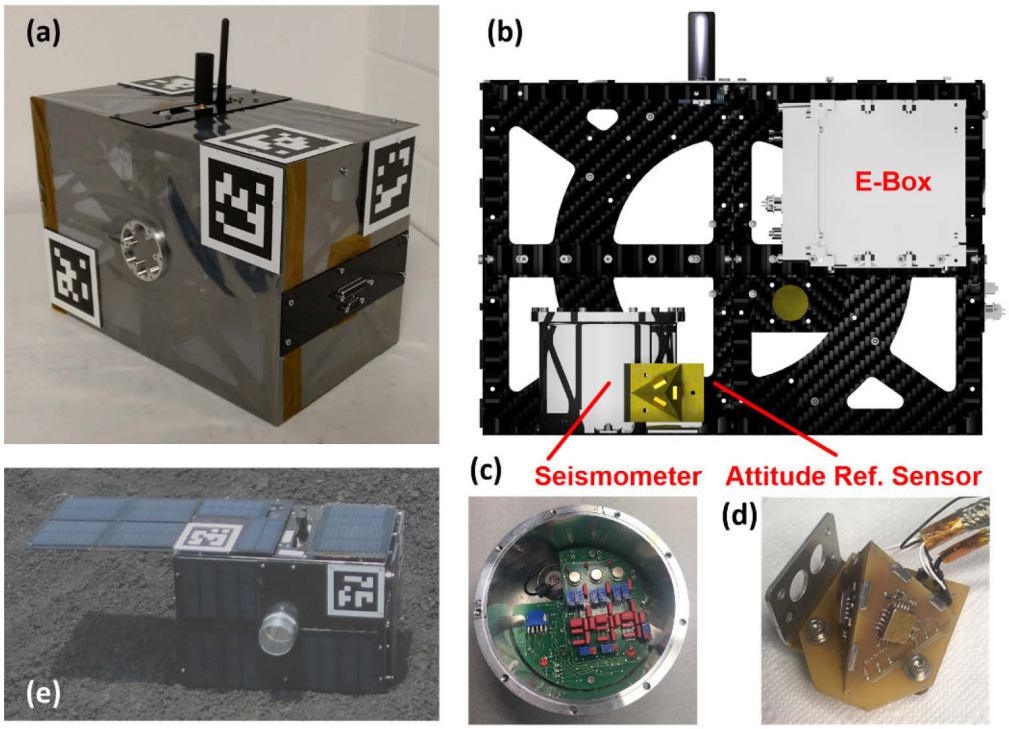

Figure 54: Monitoring station realized as bread board for field test purposes. (a) 'as-built' version with single foil cover and fiducials. (b) cross-section view with main subassemblies. (c) Details of seismometer with upper left cut-out in the front-end board revealing the vertical axis geophone and (d) attitude sensor. (e) Variant of the station with solar arrays.

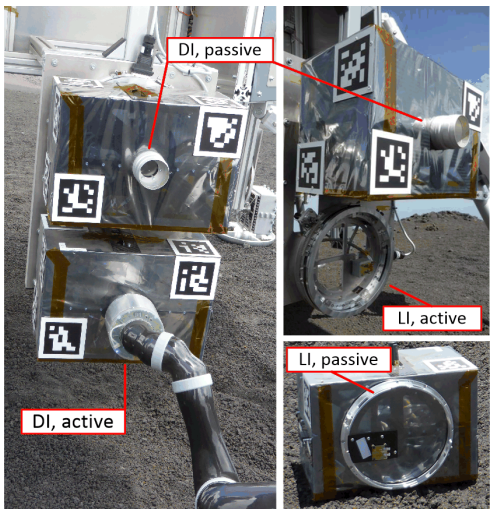

Figure 55: Locking and Docking interfaces between station and landing system and robotic arm.

Figure 56: Lander mock-up on Mt. Etna test site with lowered payload deployment mechanism and four stations mounted, seen on the lander's right and (partly hidden) left side. April tag markers are placed to support rover navigation in the lander near field.

Figure 57: Lightweight Roving Unit with manipulator arm mounted to its rear part. A cradle on the body's back can host a monitoring station.

8.4 Mission concept implementation and field testing

In response to the second objective of this project, the validation of the surface exploration mission concept, the overall architecture has to be implemented and put into an analogue test environment. This analogue mission shall primarily achieve and demonstrate mastering the station's robotic handling and deployment and the set-up of the end-to end data scientific acquisition and telemetry chain. Those are the basic building blocks of the operational concept and can be demonstrated with the station's core unit and the seismic experiment as stand-alone unit. It is acknowledged that the stacking of the additional payload compartment widens its applicability and enables the implementation of e.g. the conceptualized astronomy cases. Those added functionalities have however exempted from this particular field test in order to limit the complexity, regard project budget constraints and keep the focus on mastering the basic functionalities.

For this purpose, the core unit of the monitoring station conceptualized in the previous section has been realized and built as bread board to take part in the functional end-to-end. Hence, this campaign involves engineering models and bread boards representing the interfacing rover and lander elements as well. The tested functional chain covers the station hand-over and deployment up to the evaluation of the received seismic measurement data to provide a proof-of-concept also from scientific point of view.

The main purpose of using the analogue environment was to provide environmental context and stimulus of similar order as the lunar surface site would pose to the mission elements when performing their functions. Thereby bridge the gap between laboratory testing and a real mission implementation.

8.4.1 Mission elements functional models

The following chapter describes how the different mission elements were realized as different types of models as required for the functional demonstration. Focus is again given to the monitoring station itself whereas the interfacing elements are addressed in a brief way to understand the interaction. All mission elements are relying on off-the-shelf components or even heritage space hardware elements when mature enough to be integrated in this mission level demonstration. Verification and validation activities in preparation of the field test were therefore not rigorously performed on each unit or subsystem level but focused on assuring interoperability between the mission elements.

8.4.1.1 Surface stations

The top level requirements and constraints applicable to the bread board implementation of the station's core unit are:

1. Acquisition of high quality data in terms of temporal and domain resolution, comparable to established standards suitable to scientific publications.
2. Representativeness of mechanical and data (TMTC) interfaces in order to allow testing of the (cyber-) physical interactions between those elements in an autonomous and/or tele commanded way.
3. The mass budget was limited to 3 kg to still enable handling of the unit by the rover and its manipulator arm. Hence, the full-functional and full-scale implementation in terms of distances and dimensions must restrict itself to the core functions and/or sub-scaled components to be implemented for the station's demonstration.

The resulting 'as-built' bread board ready for the field test campaign is shown Figure 54a. The unit's structure has a size of 340 mm x 240 mm x 200 mm manufactured as a CFRP framework. The cross section view (Figure 54) shows the positions of the Common E-Box (CEB), the seismometer container, and the tetrahedral-shaped attitude reference sensor. The CEB contains all system electronics following the baseline design outlined in chapter 8.3. All avionics are however kept non-redundant in order to reduce the bread board's mass.

The on-board computer uses a microprocessor of type ARM Cortex M4 and provides an analogue-to-digital-converter (ADC) with a sampling rate of up to 20 kHz mainly in support of the scientific needs for high-rate seismic signal acquisition. Additional boards provide the communications based on wireless local area net standard (Völk et al., 2018) and time standard and time synchronization based on global navigation satellite system signals to support the (Earth-based) test data evaluation. The telemetry and tele command protocol used CCSDS compliant implementation (CCSDS, 2017). The power subsystem, stacked inside the E-box as well, consists of a 10 Wh battery and a power distribution and control unit. Both are commercial-of-the shelf products from Clyde Space (2017). The capacity of the battery has been traded against system mass. A 10Wh battery was chosen as consequence from the overall mass saving effort. This small battery capacity provided a lifetime of about 2 h with the system's average power consumption being around 5W. This lifetime was still sufficient to enable a self-contained end-to-end functional chain from deployment to scientific data generation. Nevertheless, the used power distribution and control unit (PDCU) supports solar arrays while implementing battery charging control algorithms. A version of such monitoring station has been built with a combination of deployable and body mounted solar arrays and is shown in Figure 54e. The power system design and its implications for a sustained lunar night operation are separately reported by Tsakyridis et al. (2018).

The seismometer is a Lennartz LE3Dlite Mark III short period seismometer (Lennartz Electronic, 2016). Its three geophones and front-end electronics were re-integrated into a customized housing, shown in Figure 54c.

The attitude reference sensor (Figure 54d), with the accelerometers mounted onto its faces, provides a static-only attitude reading with respect to the local gravity vector. Its signal is likewise sampled by the onboard computer's ADC. The attitude vector is not acquired continuously but polled on request by the rover and used during the placement of the station onto the soil.

The outside appearance of the station's bread board is characterized by April tags of the visual fiducial system to support the rover's recognition and handling of the station. As the lunar environment thermal protection cannot be meaningfully demonstrated in Earth environment, it has been replaced by a single layer foil for dust and sun light protection giving it a silver shining appearance.

The station has two mechanical interfaces to enable docking to the lander's payload deployment mechanism on one of the main faces and to the rover's manipulator arm end effector on the opposite panel. Both docking interface elements are passive while the active parts belong to the lander and rover respectively. The active and passive parts of the interfaces are shown in Figure 55. A docking interface DI is used for docking of the station with the robotic arm. Its active part is a rotationally symmetric docking core that uses the concept of retraction of spring elements and is described by Lehner et al., 2018) in more detail. Mechanical actuation and control of the retraction process are fully done on the rover side. Locking between lander and station is achieved with a cylindrical bayonet mount, indicated with LI. The passive part is a metallic ring with receptor slots. Actuation of the locking-pins is done by the lander's payload deployment unit with state-control provided by its on-board computer. This more complex but re-useable docking mechanism is favoured in the field test campaign

over the baseline's simpler but single-shot hold-down release mechanisms as enabler for more often repetitions of the hand-over process between lander and rover.

8.4.1.2 Lander mock-up

The rationale behind having a lander model is to realistically mimic the interactions between the mission elements during hand-over of the stations to the rover and during operations of the mission scenario. The lander model is a functional mock-up of a medium-sized lander featuring a four leg design with a 4 m diameter footprint and an octagonal-shaped body. Its height is 2.1 m, up to its top deck. The body structure provides four payload bays which are covered with solar panels. Deployment of the solar arrays opens the payload compartments. Functional elements of this lander model are its core avionics with an onboard computer identical to the monitoring stations computer. The power distribution and control system enable recharging of the landers battery via its solar arrays, permitting a permanent installation on the test site. The communication system acts as relay node between the rover, the monitoring stations and the ground stations (both the base camp and the Catania station). Further details on the communication links capabilities and architecture are described by Völk et al., (2018). Additionally, the lander model hosts four monitoring stations, needed to equip a Y-shaped station array. Each two of these units are stowed in opposing payload compartments. A payload deployment mechanism lowers the monitoring stations in a way that each station falls within the rover's manipulator workspace. The lander model with deployed payload mechanism is shown in Figure 56.

8.4.1.3 Rover and manipulation arm

The rover with its manipulator arm is without doubt a pivotal element in this mission scenario. Its functions and performance parameters are however only briefly described in a level of detail necessary to understand the interplay with the monitoring station and its deployment. The rover's role in this scenario is to take over a station from the lander, travel to its designated deployment site and deploy the station. The rover model (Figure 57) is a four-wheel drive and four-wheels steered vehicle based on DLR's Lightweight Roving Unit LRU (Wedler et al., 2015) with an operational mass of about 40 kg including a payload capability of 5 kg. A camera suite consists of a black/white stereo camera for navigation purpose and a color camera for scientific use. The stereo images are processed to provide 6D pose estimation and full 3D terrain mapping and classification with regards to obstacles and hazardous features (Schuster et al., 2018; Muller et al., 2018). The drive actuators enable a speed of approximately 1.1 m/s. An inertial reference unit and wheel odometry complement the navigation suite (Schuster et al., 2017).

The manipulator arm hardware is an off-the shelf six-segment robotic arm (Kinova Robotics, 2017). Its manufacturer rated nominal load bearing capability is 2.5 kg for mid-range and 1.5 kg for a fully extended arm. Own assessments on the load bearing capability with regard to the arm's workspace and optimized trajectory planning yielded a maximum handling capacity of 3.2 kg. This value and an associated center of mass position were used as design targets for the monitoring station. The final joint arm and station configuration were tested and validated intensively with tests as well as simulations. A consequent assessment of the "rover ergonomics" for the station hand-over between lander and rover has been crucial in maximizing the station's mass budget (Lehner et al., 2018).

8.4.2 Moon-analogue test site and mission control center

The three mission elements lander, rover, surface station and a Control Center were deployed for the analogue field test on Mt. Etna/Sicily in June 2017. The formation of site following an eruption of Mt. Etna in the year 2001 is described by Calvari and Pinkerton (2004). Figure 58 provides an overview of the site and the test installations. The coordinates of the "landing site", marked as lander station (A) in this Figure, are 37.724163 N and 15.007191 E. Feature (B) is an array of geophones buried into the soil for a continuous data acquisition of seismic data during the whole duration of the field test campaign. A basecamp (C) was deployed to support the tests with workshops and a local control center. A field weather station (D) provided reference data on local weather conditions. The rover and the monitoring stations were deployed only during daytime while night the access to the site was prohibited by local authorities. The site was selected to fulfill certain scientific and engineering criteria which are:

- General
    - The Exploration zone shall have an extent of several hundred meters to enable scientific (geophysical) and engineering tests with ranges applicable to the mission scenario outlined in chapter 8.2
    - Accessibility by cable car and off-road vehicle to enable a daily access by scientists and technicians
- Scientific
    - Basaltic terrain with alternating layers of lava flows and ashes to represent sub-surface structures that resemble shallow structures of the Moon (Cooper and Kovach, 1974; Heffels et al., 2017), with layer thicknesses accessible by using a 5 kg hammer as seismic source.
    - Active volcanic region to provide a natural seismic background with shallow quakes.
    - Lithospheric subduction zone with earthquake depths up to several hundred km (e.g. Maesano et al., 2017), to mimic deep moonquake activity.
- Engineering
    - Rocky and smooth areas without vegetation and a top surface layer of tephra to 'simulate' a dust layer
    - Optical properties with high contrast and dynamic range (at cloudless days) with pronounced bright and shadowed areas

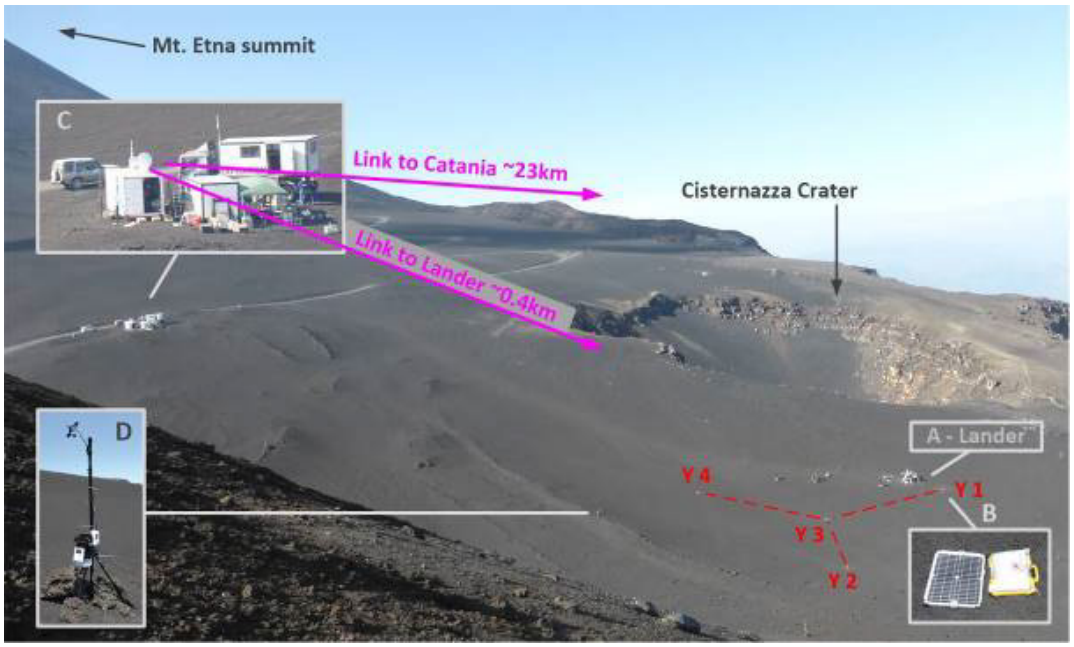

Figure 58: Mt. Etna test site – View from Laghetto cinder cone in Easterly direction onto the "Exploration Zone". Analogue mission installations are the Lander station (A), a Y-shaped network of benchmark seismometers, highlighted in dashed red lines, the Base Camp with workshops and on-site control (C) and the field weather station (D) to track environmental conditions. (For interpretation of the references to color in this figure legend, the reader is referred to the Web version of this article.)

8.4.3 Mission implementation and end-to-end functional demonstration

The following part of this chapter describes the mission integrated view and functional flow until generation of scientific data. The scientific network deployment scenario as sketched in the concept of operations (chapter 8.3) was therefore broken down into functional blocks. Those blocks are themselves aggregated functions of lower tier functions and are linked to specific mission elements. These functions were implemented as macro commands used to automatically trigger the underlying physical functions.

The top level function "Network Deployment" is decomposed into three main function "Hand over station" (F2), "Traverse to assigned waypoint" (F3) and "Place monitoring station" (F4) as shown in Figure 60 as functional flow block diagram. This chain is preceded by an initialization function (F1) and followed by the post deployment functions "Station operations" (F5) and "Rover post-deployment activity" (F6). The output of F5 execution in terms of scientific data is presented and discussed in chapter 8.4.4. Function F6 contains all functions related to opportunity science by the rover executed after its main objective of deploying the stations. Such activity is not assessed and reported in this paper.

It is important to mark that the role of the control center is to permanently monitor the mission elements autonomous operations. This is not explicitly depicted in this or the other functional flow block diagrams s this control center function is a parallel and permanent function.

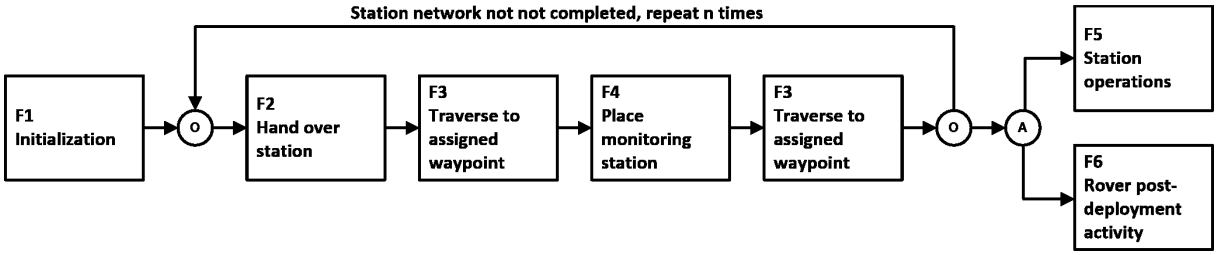

Figure 59: Network deployment main functional flow.

The functions F1 to F4 and their lower tier functions are described in more detail below. The descriptions are complemented by images taken during the field test. The level of reported detail focuses again primarily on the stations' core unit.

Function F1 – Post-landing operations and initialization: this functional block contains all functions to be executed prior to the start of the (scientific) surface operations. They provide the initial functions to be carried out prior to the network deployment and are:

F1.1 Initializations
F1.2 check-outs
F1.3 deployments of the solar arrays and
F1.4 Drooping of the monitoring station carrier frame of the lander's payload bays.

Function F2 – Hand-over monitoring station: The rover stands-by at its home position awaiting a command at the beginning of this sequence of functions. The station is in sleeping mode and sits in its restraint position in the lander's payload bay. The following sub-functions are shown as functional flow in Figure 61 and illustrated in Figure 62.

F2.1 Rover proximity operations: the rover detects its pose towards the lander and approaches in grasp position after receiving an authorization-to-proceed command from the lander. It backs off the lander after completion of the hand over sequence
F2.2 The arm of the rover uses the docking interface to connect to the station and signals readiness to the lander after completion
F2.3 The lander releases the station and signals readiness back to the rover
F2.4 The rover take over the station and place it on its carrier on the back

In the end state of this sequence the station sits in a cradle on the back of the rover. The communication link is established and maintained between both assets. The rover is back at its home position awaiting a proceed-to-waypoint command.

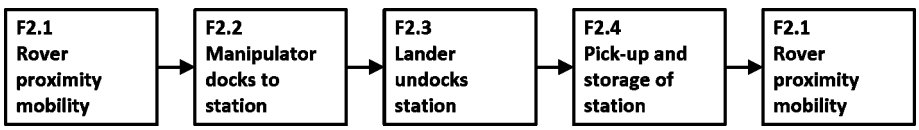

Figure 60: Decomposition of the function "Hand over station" (F2) into lower tier functions.

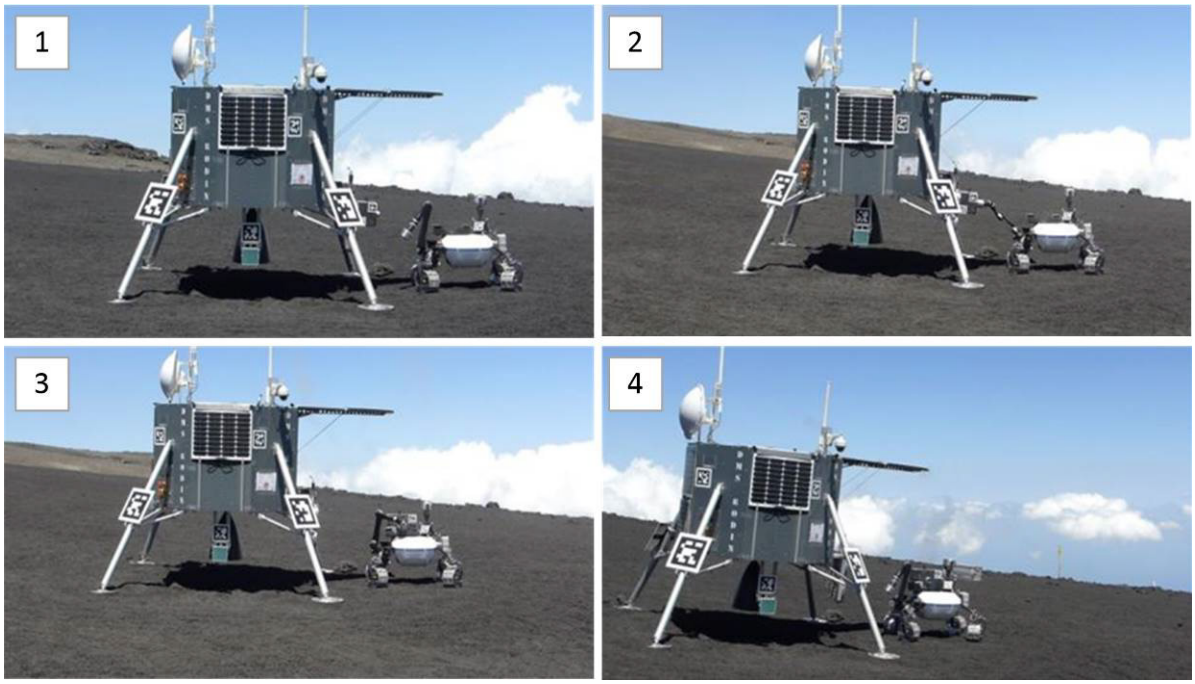

Figure 61: Image sequence depicting the execution of function "Hand over station" during the field test with (1) proximity operations, (2) grasping and docking by the manipulator arm, (3) release of the station by the lander and storage on the rover's cradle, and (4) readiness to back-off the lander. The station is a passive item handled between lander and rover.

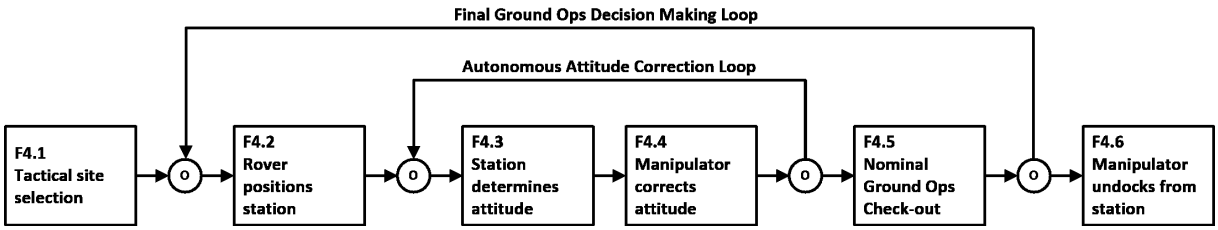

Figure 62: Decomposition of the function "Place station" (F4) into lower tier functions.

Function F3 – Traverse to next waypoint: This function is autonomously executed by the rover without interaction with the monitoring station. Autonomy is simultaneously and cannot be put into a sequential order anymore. Self-localization, ego-motion sensing and waypoint navigation in unknown and rough terrain and mobility functions such as chassis and wheel driving (slip) control are some of the autonomy features (Schuster, 2019). Similarly, robot arm path planning and following and docking interface locking and unlocking are functions of the manipulator arm. Nevertheless, the service which the rover/manipulator delivers in the overall mission scenario is requested by higher hierarchical functional chain. The rover reports back after fulfillment of its task. A detailed description of these functions is however omitted here as these functions are "rover only" functions. Interested readers are directed to Brunner et al., (2016) and Schuster et al., (2019), covering robotic viewpoints on this activity such as, navigation and localization on long traverses, manipulation in complex planetary environments and hierarchical autonomous task planning.

Function F4– Place station: The rover has arrived at the assigned region of interest for a deployment. This region is selected by human operators in the control center, based on remote sensing data and

in-situ surveys of the site. This functional flow covers only nominal intervention such as decision making regarding the station's final placement. All non-nominal interventions and contingency operations are excluded. The associated functions are shown as functional flow in Figure 62 and illustrated in Figure 63.

F4.1 Tactical evaluation of the assigned deployment site within a 5 m perimeter regarding its suitability to place the station.

F4.2 Manipulator arm re-docks to station and deploys it onto the soil. Torque-controlled, sweeping motions of the arm are used to achieve ground contact between station and soil and to achieve the required orientation and leveling.

F4.3 The station determines its attitude vector with regard to local gravity (out-of-vertical angle ε) after being placed onto the surface and being polled by the rover. This information stems from the station's own attitude reference sensor and is transmitted to the calling rover through a dedicated protocol. Limits of ε affecting the functional flow are:

(i) $\varepsilon > 5°$, immediate, autonomous attitude correction by manipulator arm through function F4.4,

(ii) $1° < \varepsilon \leq 5°$, expert judgement by ground operations staff through function F4.5, autonomous operations is halted and resumed with F4.2, F4.4 or F4.6,

(iii) $\varepsilon \leq 1°$, any autonomous attitude correction is by-passed and the functional flow proceeds after confirmation through function F4.5 to F4.6

F4.4 Torque-controlled, sweeping motions of the arm are used to improve ground contact between station and soil and to achieve the required orientation and leveling.

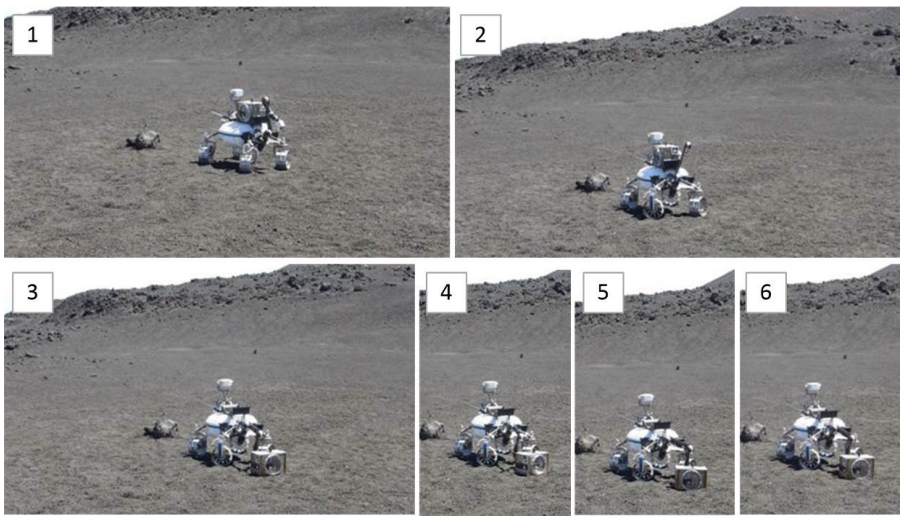

Figure 63: Image sequence depicting the execution of function "Place station" during the field test with (1) site selection and (2) re-docking to the station. (3) placing of the station and (4) to (6) execution of a 'sweeping/paving' move in order to correct the station's attitude and coupling with regard to the soil. The station takes an active role inside the attitude correction control loop.

F4.5 The station is commanded to take seismic sample measurement at the end state of this functional block. The rover still stands-by the station ready to withdraw and awaiting a newly assigned waypoint.

F4.6 The arm undocks and the rover backs-off the monitoring station.

8.4.4 Scientific proof-of-concept

An active seismic experiment has been conducted on the field test site as a scientific application case for the monitoring station and to prove its role as seismic observatory. Therefore, a seismic refraction profile was recorded along a line between stations Y2 and Y1. A 5-kg hammer and an aluminum disk target were used as active source as usually done in short distance seismic profiling. The source was positioned in line with the profile but at 15 m distance to Y2 in order to reduce times of saturation of the seismometer during strokes. A monitoring station was moved along the profile line, set down and levelled at regular intervals of 2 m, then 10 to 20 hammer strokes were performed and the resulting seismic signal was recorded by the tele-commanded station. Figure 64a shows this experimental set-up with a view from the active source along the profile line towards station Y1 and the lander. The two stations at both ends of the profile (Y2 and Y1) provided reference times for the computation of travel times as seen in Figure 64b.

The evaluation of the seismic refraction data is based on the analysis of travel time differences along the profile line. The distance between the source and the measuring equipment is known in this test. Then seismograms – shown in Figure 65 – are used to determine the time it takes for a signal to travel from source to current measuring point. The campaign recorded 14 valid seismic data sets at points along the 60 m long profile line. The used source (here a sledgehammer) generates mainly compressional waves. Since this type of wave travels the fastest, they are referred to as primary or P waves. Usually P-wave arrival identification is straightforward compared to other seismic wave types. The time it takes a P-wave to travel from the source (Y2) to the respective point is used as travel time for further evaluation.

Distances and corresponding P-wave travel times, as read from the seismograms in Figure 65, are plotted in a diagram in Figure 66. For interpretation, we assume that the underground consists of layers parallel to the surface, each with a constant P wave velocity. At a critical distance, Mach head waves from the layer interface overtake waves traveling in the upper layer, resulting in a piecewise linear segmentation of arrival times. This diagram shows that two clusters of arrivals – blue and pink markers, corresponding to a two layer model – can be identified and are suitable for further analysis. In accordance with the constant-velocity hypothesis, straight lines are fitted to these clusters whose gradients g1 and g2 and intercept time tint are determined. Signal arrivals marked 48, 52, and 54 are considered as outliers due to their remote position in relation to the initially estimated straight line and are thus excluded from the evaluation. The thickness h of the uppermost layer can be calculated by the following equation:

$$h = \frac{v_i \, t_{int}}{2 \cos i_c}$$

The velocity of the first layer is $v_1 = 1/g_1$ and the velocity of the second layer is $v_2 = 1/g_2$ respectively. The critical angle for total reflection at the layer interface is $i_c = \arcsin(v_1/v_2)$. The uppermost layer has a very low seismic velocity of approximately $v_1 = 92$ m/s and its thickness can be calculated to about h = 11 m. The layer below is a more consolidated material with a seismic velocity of $v_2 = 245$ m/s. The result is illustrated in the sketched extension to the image in Figure 64c. The distribution and thickness of the layering following the 2001 Etna eruptions and deposits therefrom are well documented in the work of Coltelli et al., (2007) which confirms the result derived from the seismic refraction experiment. A second set of measurements with reversed shot direction to resolve possible layer tilts could not be conducted due to weather conditions during the later part of the field campaign.

Regarding the actual lunar surface, Cooper et al. (1974) presented a five-layer model for the lunar near-side surface based on the findings of the Apollo missions 14, 16, and 17. In their model the uppermost

layer has a velocity of 100 m/s and a thickness of 4 m. The second layer has a velocity of 327 m/s. These lunar surface conditions correspond well with the determined layering depth and velocity found on Mt. Etna at the Laghetto site. Drawing upon that, it could be claimed that Mt. Etna is a suitable choice as analog region for the Moon with regard to shallow surface seismic observations.

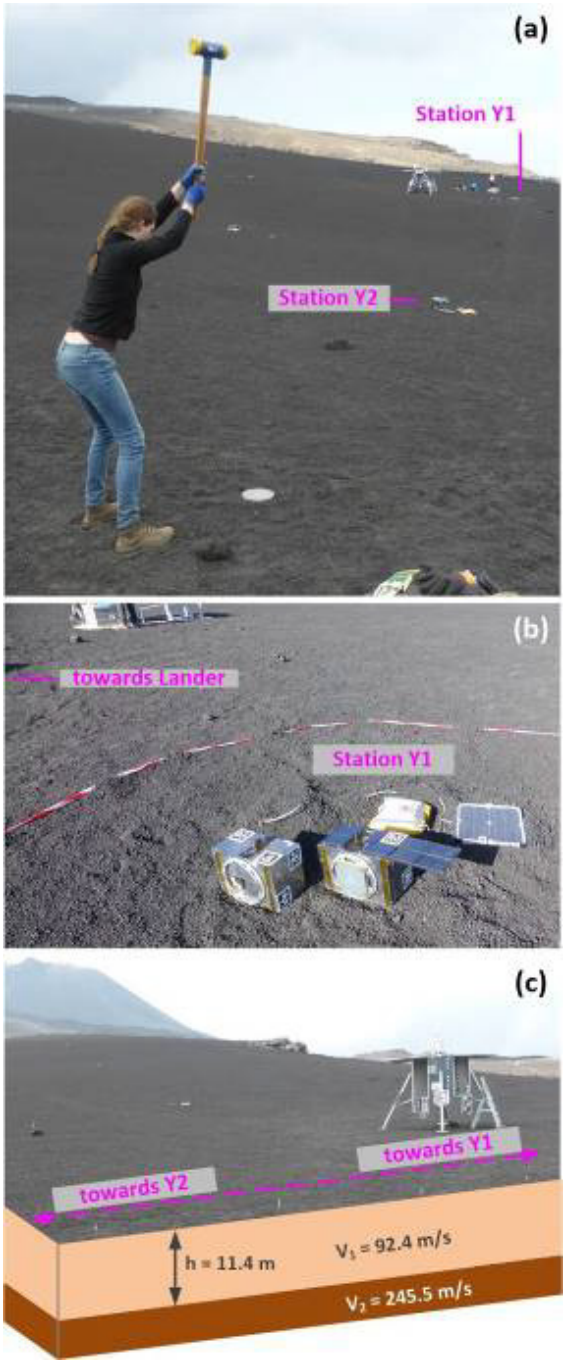

Figure 64: Experimental set-up of the active seismic profiling. (a) 'active seismic source' hitting an aluminum disk and a station at node Y2, (b) joint measurements by two surface station models (with and without solar arrays) and a buried reference geophone at node Y1, (c) exploration zone with shallow surface layering as determined by the seismic profiling.

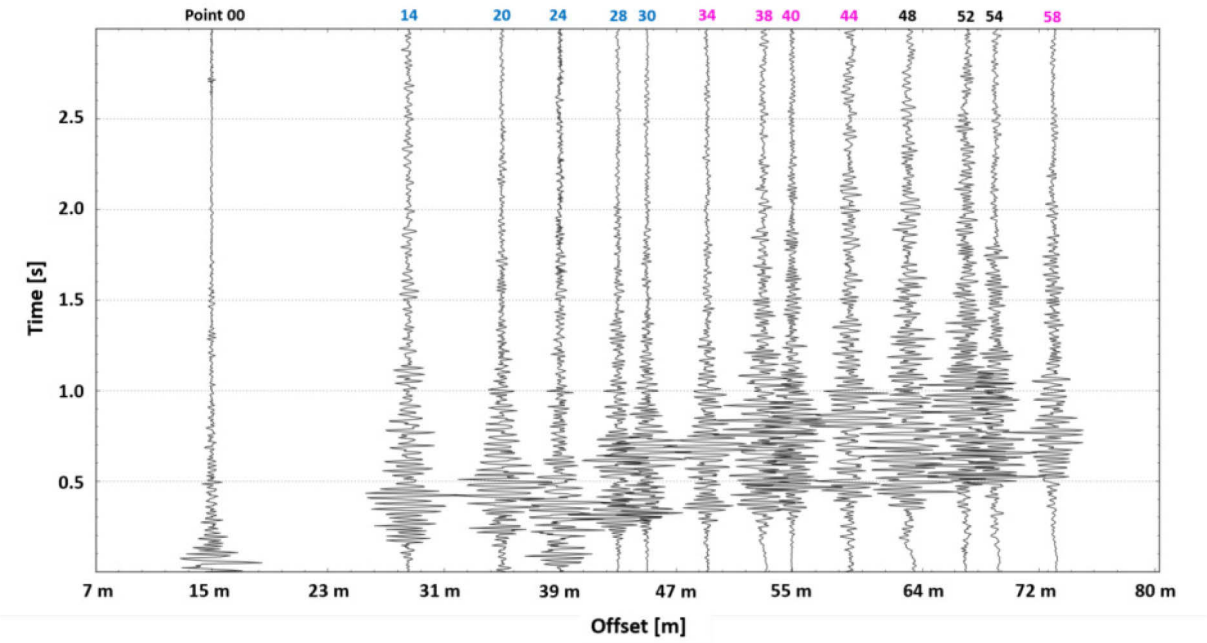

Figure 65: Section plot of the vertical component. This plot shows example data of one hammer stroke for each of the 14 points used for the evaluation.

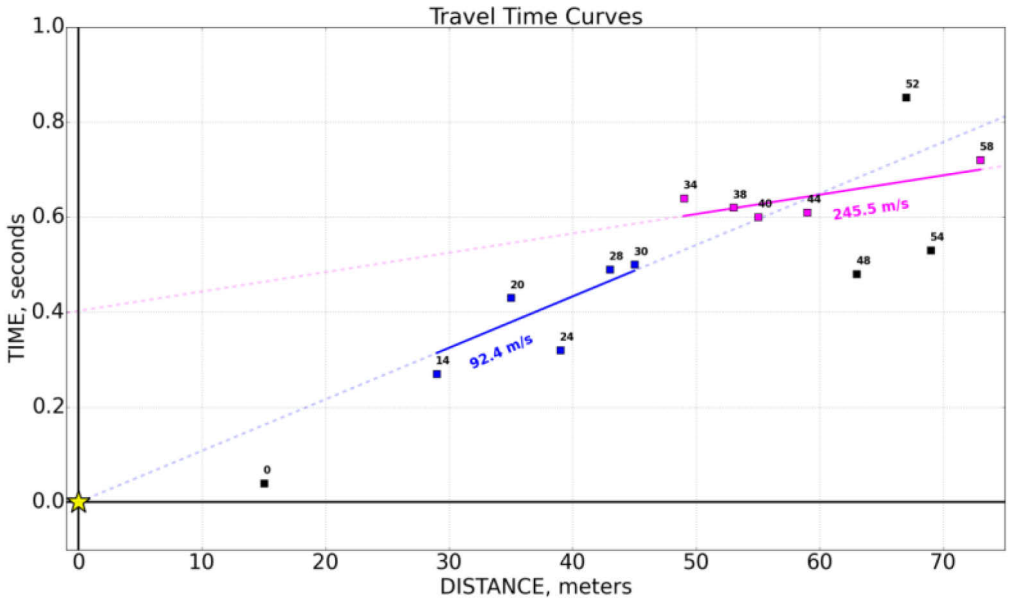

Figure 66: Depiction of the 14 used points with linear regression lines fitted to the points representing a two-layer model. The blue markers represent the uppermost layer. Travel times of second layer points are shown in pink color. Outliers are marked in black color. (For interpretation of the references to color in this figure legend, the reader is referred to the Web version of this article.)

8.4.5 Further findings and 'lessons-learned' from field test

The previous chapters focus exclusively on the system and mission and the scientific and technical aspects of deploying and using the presented station concept. Nevertheless, the field test campaign yielded a large number of findings and lessons-learned from its de-briefing. Major ones which complement the campaign results and which can be transferred in a generalized form to other campaigns are collected below.

Estimations of durations of test and task execution from previous lab and even outdoor testing were significantly underestimated. Contributing factors can be attributed to the unstructured terrain and environment factors of the site and the remote access by the simulated ground ops personnel. Those are desired findings and main reason to conduct an analogue campaign to identify exploration-like factors in the mission concept. Other factors were not Moon-analogue and range from adverse weather (sunny and calm scenes as seen e.g. on Figures 58 and 61 hide the fact that Mt. Etna is a high alpine region with rapidly changing visibility and wind conditions) and up to groups of tourists interrupting test executions (the test site is a World Natural Heritage and exclusive access by the test teams only was not granted by authorities). Mostly, overall delays were mixtures from both groups and some are reactionary to them (e.g. depleted batteries after unplanned loiter periods), making a break-down into relevant and irrelevant delays difficult or nearly impossible. Even if cumbersome, a better event and 'side-factors' tracking could be worth the effort. Large schedule contingency should be foreseen in the field test campaign planning.

A rigorous establishment of a catalogue of mission (here: field test) success criteria was useful and is recommendable. Campaign planners shall be however aware and acknowledge that different levels of conceptions of 'mission success' might or should remain and balanced. E.g. a certain limited level of task automatization or autonomy might be acceptable by mission engineers or project scientists while being unsatisfactorily from the roboticist's point of view having a technology demonstration in mind. The number of repetitions of a seismic experiment might be sufficient from an engineering point of view to show reproducibility of a process but maybe insufficient from the geophysicists point of view for a scientific evaluation.

It is recommendable to record and archive data (structured and unstructured) as 'by-products' from sources beyond the immediate needs of the campaign. E.g. records of the field weather station were used later to identify wind conditions in conjunction with seismic records to contribute to the InSight mission (Knapmeyer-Endrun et al., 2018).

Important technical findings were data link signal strength weakness between lander and rover when in close proximity to each other. The lander structure with deployed solar arrays obstructed the line-of-sight to its top-mounted antennas and shielded the rover. Signal strength and link availability in very mission critical close-proximity operations is needed to be more carefully assessed.

8.5 Conclusions

A lunar surface science station has been conceptually designed which could act as single, stand-alone element or as a node in a geophone and/ or radio antenna array of several such stations, or as a small precursor array for a larger interferometric observatory. The station's design considers mature technologies for its subsystems which are available today and integrates them into the presented highly integrated and compact instrument container. The underlying key design parameter and assumptions regarding the design details have been stated.

Focus is given to the question whether such small station can operate continuously during the lunar day and night. Thermal and power design is based on solar arrays and conventional, non-nuclear, battery systems. The analysis shows that meaningful scientific operations – in terms of instrument duty time and data volume – can be conducted during lunar night. Lunar night temperatures can be exploited to passively cool down the sensor head of an IR telescope to its operating temperatures. Power saving – and ultimately mass saving – come however at the price that the station itself cannot communicate directly to an orbiting gate way or relay satellite due to the relatively high expense in transmission power. It therefore would rely on communication to a gate way or relay node on the lunar surface. Another focus was given to a structure shape, its physical interfaces and TMTC protocols which enable the stations handling by robotic assets. Its simplistic, brick-shaped design and compactness has shown as beneficial feature for its modularization and to facilitate its handling, transportation and deployment by a rover equipped with a robotic arm. The conceptual design also considers a modularization of the station into a core unit with system electronics and limited science instrumentation and a stackable cold unit with added instrumentation requiring cold operating temperatures such as the telescope's IR-receiver and radio antenna in this case. Whether such physical partitioning into two distinct units is necessary or not for a particular mission design could not be answered by this study as it depends on the actual rover's handling capability and actually selected instruments.

Test and demonstration with an engineering model of the station's core unit has been successfully done in the frame of a Moon analogue mission on Mt. Etna/Sicily. From an engineering standpoint, the test has shown that the station supports and improves the automatization of the robotic deployment by being an active element in the deployment-loop. Dedicated sensors, tele-command and telemetry protocols are required for this task. This field test has shown as well that the functional flow for a network deployment could be broken down into few, repeating functional blocks which ease the effort and complexity of installation of such scientific station.

The functional model of the station has been equipped with a set of geophones and enabled a demonstration of the geophysical science case of the station. From a science standpoint, the evaluation of the recorded seismic data acquired during this field test demonstrates the general suitability of the station for scientific exploration of the subsurface. Additionally, it confirmed that the Mt. Etna Laghetto site was an adequate choice regarding shallow surface seismic observations. Finally, field tests in an analogue environment mean more than just 'open air' tests. The results and findings of this project confirm the idea that those kinds of campaigns are important elements to close the gap between Earth lab tests and the later planetary environment.

Author contributions

Lars Witte: Conceptualization, Methodology, Supervision, Writing.
Alexandra Heffels: Investigation, Formal analysis, Writing
Matthias Killian: Methodology, Formal analysis, Writing
Martin Knapmeyer: Conceptualization, Supervision, Writing
Caroline Lange: Methodology, Investigation, Writing
Norbert Toth: Software, Methodology
Georgios Tsakyridis: Methodology, Investigation, Writing
Armin Wedler: Conceptualization, Supervision, Writing

Declaration of competing interest

The authors declare that they have no known competing financial interests or personal relationships that could have appeared to influence the work reported in this paper.

Acknowledgments

This work was supported by the Helmholtz Association, project alliance ROBEX, under contract number HA-30.

8.6 References

Block, J., Straubel, M., Wiedemann, M., 2010. Ultralight deployable Booms for solar Sails and other large gossamer Structures in space. Elsevier Acta Astronaut. 68 (7–8), 984–992. https://doi.org/10.1016/j.actaastro.2010.09.005. ISSN 0094–5765.

Brunner, S.G., Steinmetz, F., Belder, R., Domel, A., 2016. RAFCON: A graphical tool for engineering complex, robotic tasks. IROS.

Buckle, R., Roberts, S., 2017. Review of commercial cells for space applications. ESPC 2016, E3S Web of Conferences 16, 17006. https://doi.org/10.1051/e3sconf/20171617006.

Calvari, S., Pinkerton, H., 2004. Birth, growth and morphologic evolution of the 'Laghetto' cinder cone during the 2001 Etna eruption. J. Volcanol. Geoth. Res. Volume 132 (2–3) https://doi.org/10.1016/S0377-0273(03)00347-0.

Carpenter, J., 2010. ESA Lunar Lander Phase B1 Payload Definition Document, LLB1-PDD-ESA(HSF)-0001, ESA/ESTEC.

Carpenter, J., 2019. Lunar Exploration in ESA's European Exploration Envelope Programme, Presented at the 7th European Lunar Symposium. Manchester/UK.

CCSDS, 2017. Consultative committee for space data systems (CCSDS). https://public.ccsds.org/default.aspx.

Clyde Space, 2017. User Manual: 3rd Generation EPS. https://www.aac-clyde.Space.

Coltelli, M., Proietti, C., Branca, S., Marsella, M., Andronico, D., Lodato, L., 2007. Analysis of the 2001 lava flow eruption of Mt. Etna from three-dimensional mapping. J. Geophys. Res.: Earth Surface 112 (F2).

Cooper, M.R., Kovach, R.L., Watkins, J.S., 1974. Lunar near-surface structure. Rev. Geophys. 12 (3), 291–308.

Crawford, I., Zarnecki, J., 2008. Astronomy from the Moon. Astron. Geophys. 49 (2), 2.17–2.19. https://doi.org/10.1111/j.1468-4004.2008.49217.x.

Foing, B., 1994. The Moon as a site for astronomy and space science. Adv. Space Res. Vol. 14 (6), 9–18.

Greiner, J., Trenti, M., Klose, S., 2017. Skyhopper: the First Infrared Space Telescope on a CubeSat, 6th Interplanetary CubeSat Workshop. Cambridge/UK, May 2017. https://icubesat.files.wordpress.com/2017/05/2017-b-1-2-20170530174534-skyhopper.pdf. accessed November 2017.

American Geophysical Union (AGU) Haase, I., Wählisch, M., Gläser, P., Oberst, J., Robinson, M., 2019. Coordinates and Maps of the Apollo 17 landing site. Earth Space Sci. 6 (1), 59–95. https://doi.org/10.1029/2018EA000408. ISSN 2333–5084.

Harwit, M., 1994. Infrared astronomy from the Moon. Adv. Space Res. Vol. 14 (6), 69–76.

Heffels, A., Knapmeyer, M., Oberst, J., Haase, I., 2017. Re-evaluation of Apollo 17 lunar seismic profiling experiment data. Planet. Space Sci. 135, 43–54.

Ho, T.-M., et al., 2017. MASCOT - the mobile asteroid surface Scout onboard the Hayabusa2 mission. Space Sci. Rev. 208, 339–374. https://doi.org/10.1007/s11214-016-0251-6.

ITU, 2013. International Telecommunication Union, Handbook on Radio Astronomy, third ed. Radiocommunication Bureau www.itu.int. (Accessed February 2020).

ITU, 2017. International Telecommunication Union, Protection of Frequencies for

Radioastronomical Measurements in the Shielded Zone of the Moon, Recommendation ITU-R RA, 479. Radiocommunication Bureau. www.itu.int. (Accessed February 2020).

Joliff, B.L., Gillis, J.J., Haskin, L.A., Korotev, R.L., Wieczorek, M.A., 2000. Major lunar crustal terranes: surface expressions and crust-mantle origins. J. Geophys. Res: Plan 105, 4197–4216. https://doi.org/10.1029/1999JE001103.

Kawamura, T., et al., 2019. Autonomous lunar geophysical experiment package (ALGEP),

white paper in response to the voyage 2050 long-term plan in the ESA science Program. www.cosmos.esa.int/web/voyage-2050/white-papers. (Accessed September 2019).

Klein Wolt, M., et al., 2012. Radio astronomy with the European Lunar Lander: opening up the last unexplored frequency regime. Planet. Space Sci. 74, 167–178. https://doi.org/10.1016/j.pss.2012.09.004.

Knapmeyer-Endrun, B., Murdoch, N., Kenda, B., et al., 2018. Influence of body waves, instrumentation resonances, and prior assumptions on Rayleigh wave ellipticity inversion for shallow structure at the InSight landing site. Space Sci. Rev. 214, 94. https://doi.org/10.1007/s11214-018-0529-y.

Kring, D., 2013. Exploring the Schr€odinger and South Pole-Aitken Basins on the Lunar Farside, Presentated at the 13th European Planetary Science Conference. London. www.lpi.usra.edu/science/kring/lunar_exploration/Kring_EPSC2013_LunarFarsideLandingSites.pdf. (Accessed 6 September 2019).

Laneuville, M., Wieczorek, M.A., Breuer, D., Tosi, N., 2013. Asymmetric thermal evolution of the Moon. J. Geophys. Res.: Plan 118 (7), 1435–1452. https://doi.org/10.1002/jgre.20103.

Lehner, P., et al., 2018. Mobile manipulation for planetary exploration. In: IEEE Aerospace Conference Proceedings. IEEE. 2018 IEEE Aerospace Conference, 3-10 March 2018. Big Sky, MT, USA. https://doi.org/10.1109/AERO.2018.8396726. ISBN 978-1-5386-2014-4.

Lennartz Electronic, 2016. LE-3Dlite MkIII Specification. www.lennartz-electronic.de/index.php/de-de/seismometers-de/le-3dlite. (Accessed December 2019).

Lognonné, P., et al., 2019. SEIS: insight's seismic experiment for internal structure of Mars. Space Sci. Rev. 215, 12. https://doi.org/10.1007/s11214-018-0574-6.

Maesano, F.E., Tiberti, M.M., Basili, R., 2017. The Calabrian Arc: three-dimensional modelling of the subduction interface. Sci. Rep. 7, 8887.

Muller, M.G., Steidle, F., Schuster, M.J., Lutz, P., Maier, M., Stoneman, S., Tomic, T., Stürzl, W., 2018. Robust visual-inertial state estimation with multiple odometries and efficient mapping on an MAV with ultra-wide FOV stereo vision. IROS.

NASA ALSEP, 1971. (Unknown Authors). Apollo Lunar Surface Experiments Package and Particles and Fields Subsatellite System Description and Data Flow, NASA Manned Spacecraft Center. Houston/Texas, May 1971.

Pike, T., et al., 2014. A self-levelling nano-g silicon seismometer. Valencia IEEE Sensors 1599–1602. https://doi.org/10.1109/ICSENS.2014.6985324.

Rayman, M., Saunders, R., 1996. Optical interferometry from the lunar surface. Adv. Space Res. Vol. 18 (11), 45–48.

Renk, F., et al., 2017. Human Lunar Exploration Precursor Program, Mission Analysis Guidelines, ESA-HSO-K-TN-0008, Issue 1, Revision 0, MAS Working Paper No. 619. ESA/ESOC.

Richter, M., Straubel, M., Fernandez, J.M., Stohlman, O.R., Wilkie, W.K., 2019. Compact deployment control Mechanism for the deployable backbone Structure of a 500-m2-Class solar sail. ISSS 2019, 29.07.2019 - 02.08.2019, Aachen, Deutschland. https://elib.dlr.de/128852/.

Kinova Robotics, 2017. Jaco V2 specification sheet. www.kinovarobotics.com. (Accessed November 2017).

Satlab, 2018. Full-duplex low-power S-band transceiver, Product specification satlab SRS-3. www.satlab.com. (Accessed February 2020).

Schneider, J., et al., 2019. OWL-MOON : Very High Resolution Spectro-Imaging andEarth-Moon Interferometry: Exoplanets to Cosmology. White Paper submitted toESA's call for Voyage 2050, [arXiv:1908.02080].

Schuster, M.J., 2019. Collaborative Localization and Mapping for Autonomous Planetary Exploration: Distributed Stereo Vision Based 6D SLAM in GNSS-Denied Environments. Ph.D. dissertation. University of Bremen, 2019. http://nbnresolving.de/urn:nbn:de:gbv:46-00107650-19.

Schuster, M.J., et al., 2017. Towards Autonomous Planetary Exploration: the Lightweight Rover Unit (LRU), its Success in the SpaceBotCamp Challenge, and beyond. Journal of Intelligent & Robotic Systems. Springer. https://doi.org/10.1007/s10846-017-0680-9. ISSN 0921–0296.

Schuster, M.J., Schmid, K., Brand, C., Beetz, M., 2018. Distributed stereo vision-based 6d localization and mapping for multi-robot teams. J. Field Robot. https://onlinelibrary.wiley.com/doi/abs/10.1002/rob.21812.

Schuster, M.J., Muller, M.G., Brunner, S.G., Lehner, H., Lehner, P., 2019. Towards heterogeneous robotic teams for collaborative scientific sampling in lunar and planetary environments. In: Workshop on Informed Scientific Sampling in Large-Scale Outdoor Environments at IROS, 2019.

Silk, J., 2018. Put telescopes on the far side of the Moon. Nature 553, 6. https://doi.org/10.1038/d41586-017-08941-8, 2018.

Teledyne Imaging Sensors, 2012. H2RG Visible & Infrared Focal Plane Array, Product Specification Brochure. Revision 6, version 2.2. www.teledyne-si.com. (Accessed November 2017).

Tsakyridis, G., et al., 2018. Power system analysis and optimization of a modular experiment Carrier during an analog lunar demo mission on a volcanic environment. Elsevier Acta Astronautica, Seiten 200-210. https://doi.org/10.1016/j.actaastro.2018.11.034. ISSN 0094-5765.

Vasavada, A.R., Paige, D.A., Wood, S.E., 1999. Near-surface temperatures on mercury and the Moon and the stability of polar ice deposits. Icarus 141/2, 179–193. https://doi.org/10.1006/icar.1999.6175.

Völk, S., et al., 2018. The Network Infrastructure for the ROBEX Demomission Space. SpaceOps Conference, 28. May - 01. Jun. 2018, Marseille, France. [elib.dlr.de/124166/].

Wang, J., et al., 2015. 18-Month operation of Lunar-based Ultraviolet Telescope: a highly stable photometric performance. Astrophys. Space Sci. 360, 10. https://doi.org/10.1007/s10509-015-2521-2.

Wedler, A., Rebele, B., Reill, J., Suppa, M., Hirschmüller, H., Brand, C., Schuster, M., Vodermayer, B., Gmeiner, H., Maier, A., Willberg, B., Bussmann, K., Wappler, F., Hellerer, M., 2015. LRU - Lightweight Rover Unit. ASTRA, 2015.

Wieczorek, M.A., Neumann, G.A., Nimmo, F., Kiefer, W.S., Taylor, G.J., Melosh, H.J., Phillips, R.J., Solomon, S.C., Andrews-Hanna, J.C., Asmar, S.W., Konopliv, A.S., Lemoine, F.G.,

Smith, D.E., Watkins, M.M., Williams, J.G., Zuber, M.T., 2013. The crust of the Moon as seen by GRAIL. Science vol. 339 (6120), 671–675. https://doi.org/10.1126/science.1231530.

Wollenhaupt, W.R., Sjogren, W.L., 1972. Comments on the figure of the Moon based on preliminary results from laser altimetry. Earth Moon Planets 4 (3), 337–347.